Investigation of the Light-Induced Intermediate States in Type I Photosynthetic Reaction Centers

Inaugural-Dissertation

zur

Erlangung des Doktorgrades der

Mathematisch-Naturwissenschaftlichen Fakultät

der Heirich-Heine-Universität Düsseldorf

vorgelegt von

Leysan Khuzeeva

aus Kazan, Ruβland

Düsseldorf, April, 2009

Aus dem Max-Planck-Institut für Bioanorganische Chemie,

Mülheim an der Ruhr, Germany

Gedruckt mit der Genehmigung der Mathematisch-Naturwissenschaftlichen Fakultät der Heirich-Heine-Universität Düsseldorf

Referent: Prof. Dr. Wolfgang Lubitz

Korreferent: Prof. Dr. Lutz Schmitt

Tag der mündlichen Prüfung: 19 April, 2009

For my family

All truths are easy to understand once they are discovered; the point is to discover them. (Galileo Galilei)

Acknowledgements

First of all I would like to thank my supervisor Professor Dr. Wolfgang Lubitz for providing me the possibility to work on an interesting PhD thesis. Vielen Dank!

Prof. Dr. Lutz Schmitt is acknowledged for being the second reviewer of my thesis.

I would like to thank my co-supervisor Dr. Mikhail L. Antonkine for his advices and help during my thesis work. I also knowledge Dr. Jens Niklas, Dr. Anton Savitsky, Dr. Alexey Silakov, Dr. Shipra Prakash, Dr. Özlen Erdem, Dr. Maria-Eirini Pandelia, Dr. Nicholas Cox and Prasanna Rangadurai for good discussions and valuable comments and remarks on my thesis work. I sincerely thank to Dr. Mikhail L. Antonkine and Dr. Jens Niklas for kindly providing the samples of PS I for the A_0 project.

I would like to thank all the Max Planck institute members who made the time spent for me, especially Gudrun Klihm, Frank Reikowski, Christoph Laurich, Michael Reus, Horst Selbach for their support with the experimental work.

I also would like Professor John H. Golbeck and their laboratory from the Department of Biochemistry and Molecular Biology, The Pennsylvania State University, for providing the samples of the heliobacterial reaction centers.

I would like to thank my friends and especially Dr. Ruslan Ovsyannikov for their help and support. Thank You!

At last I would like to thank my parents and my husband Timur Khayrov for their continuous help and giving motivation in difficult times of my thesis work and my life.

Abstract

Photosynthesis is the natural process by which light energy is converted into physiologically available chemical energy and is, thus, one of the most important processes in nature. Light-induced charge separation between donor and acceptor molecules (cofactors) initiates electron transfer in reaction center (RC). Subsequent electron transfer (ET) steps proceed through a sequence of cofactors. Electron paramagnetic resonance (EPR) spectroscopy allows the detection of intermediate states involved in ET (*e.g.* radicals, radical pairs and triplet states). The focus of this work is EPR investigation of intermediate electron acceptors in Type I RC to obtain information about their structure and function.

Chapter 5 is devoted to the primary electron acceptor A_0 in the Photosystem I (PS I). The acceptor A_0 is a chlorophyll *a* (Chl *a*) molecule, as was shown by X-ray crystal structure of PS I and optical data. The direct EPR investigation of transient A_0 in the $P_{700}^{\bullet+}A_0^{\bullet-}$ radical pair (RP) is difficult because of its short lifetime (~ 10 ns). Therefore, the intermediate A_0 was studied in the stationary photoaccumulated state. Additionally, the electrochemically generated Chl *a* anion radical in liquid and frozen solution was used as model for the $A_0^{\bullet-}$ system. Advanced EPR methods, such as ENDOR, TRIPLE, HYSCORE, were used to obtain the hyperfine and quadrupole couplings of the photoaccumulated radical $A_0^{\bullet-}$ and the electrochemically generated Chl *a* anion radical. The comparison of the native cofactor and the *in vitro* model system further clarified the current picture of the electronic structure of the primary electron acceptor $A_0^{\bullet-}$ and the influence of the protein surrounding on the electron spin density distribution.

The Chapter 6 describes multifrequency EPR study of the primary photosynthetic processes in the heliobacterial RC (HbRC). An investigation of HbRC is complicated due to fast primary ET rates and the high sensitivity of the major pigment of HbRC, BChl *g*, to oxidation. The main aim was to clarify the proposed role of a quinone as the secondary electron acceptor A_1 of HbRC, as is seen for PS I. Several biochemical treatments on HbRC were performed, *e.g.* quinone replacement and photoaccumulation of ET cofactors. Transient EPR (TREPR) spectroscopy was used to detect the short-lived paramagnetic states, i.e. RPs, triplets. The influence of both oxidation and light excitation were investigated. The explanation of the experimental results as well as parameters obtained from data analysis do not require the formation of the intermediate RP $P_{798}^{\bullet+}A_1^{\bullet-}$. However, the participation of the quinone in the ET of HbRC can not be explicitly excluded.

TABLE OF CONTENTS

Table of Contents

Abbreviations

A, A_i	- hyperfine tensor, principal values
A_0	- "primary" electron acceptor in Photosystem I
A_1	- "secondary" electron acceptor in Photosystem I
a_{iso}	- isotropic hyperfine value
AQ	- anthraquinone
ATP	- adenosine triphosphate
B_0, B_1	- static external magnetic field, microwave field
BChl *g*	- bacteriochlorophyll *g*
bRC	- bacterial reaction center
Car	- carotenoid
CD	- circular dichroism
Chl *a, b, c, d*	- chlorophyll *a, b, c, d*
CV	- cyclic voltammogram
CW	- continuous wave
D, E	- zero field splitting parameters
DEAE	- diethylaminoethyl
DFT	- density function theory
DME	- dimethoxyethane
DQ	- duroquinone
E/A	- emission/ absorption
ENDOR	- electron nuclear double resonance
EPR	- electron paramagnetic resonance
ESE	- electron spin echo

Abbreviations

ESEEM	- electron spin echo envelope modulation
ET	- electron transfer
FID	- free induction decay
FSE	- field-swept echo
F_X, F_A, F_B	- terminal electron acceptor in Photosystem I
g, g_i	- *g*-tensor, principal values
HbRC	- heliobacterial reaction center
hfc	- hyperfine coupling
HOMO	- highest occupied molecular orbital
HPLC	- high performance liquid chromatography
HYSCORE	- hyperfine sublevel correlation spectroscopy
ISC	- intersystem crossing
LHC	- light-harvesting complex
LUMO	- lowest occupied molecular orbital
MOPS	- 3-[N-Morpholino]propanesulfonic acid, buffer
MQ-7	- menaquinone-7
NADP+, NADPH	- nicotinamide adenine dinucleotice: oxidized, reduced
NMR	- nuclear magnetic resonance
OEC	- oxygen evolving complex
OPO	- optical parametric oscillator
P_{680}	- electron donor in PS II
P_{700}	- electron donor in PS I
P_{798}	- electron donor in HbRC
P_{865}/P_{960}	- electron donor in bRC
PC	- plastocyanine

Abbreviations

PDB	- protein data bank
Pheo	- pheophytin
PhQ	- phylloquinone
PQ-9	- plastoquinone-9
PS I, PS II	- photosystem I, photosystem II
PsaA, PsaB, PsaC	- main protein subunits in PS I
PshA, PshB	- protein subunits in HbRC
Q_A, Q_B	- quinone acceptors in Type II RC
RP	- radical pair
S_i	- singlet sublevels
SCE	- saturated calomel electrode
T_i	- triplet sublevels
$TBABF_4$	- tetrabutylammonium-tetrafluoroborate
TREPR	- time-resolved EPR
TRIPLE	- electron nuclear nuclear triple resonance
VK_1 / VK_3	- vitamin K_1/K_3
X, Q, W	- EPR frequency bands
ZFS	- zero-field splitting

Chapter 1. Photosynthesis

1.1 Importance of photosynthesis

The primary source of energy for nearly all life on the Earth is the Sun. The energy of sunlight is introduced into the biosphere by a process known as photosynthesis, which occurs in plants, algae and bacteria. The photosynthetic process arises in a set of complex protein molecules that are located in and around a highly organized membrane. Through a series of energy converting reactions, the photosynthetic apparatus transforms light energy into a stable form of energy that can be stored for millions of years.

In plants, algae and certain types of bacteria, the photosynthetic process results in the release of molecular oxygen and the removal of carbon dioxide from the atmosphere that is used to synthesize organic materials, like carbohydrates (*oxygenic* photosynthesis). Other types of bacteria use light energy to create organic compounds but do not produce oxygen (*anoxygenic* photosynthesis).

Photosynthesis is the main pathway for assimilation of the inorganic carbon in the biological cycle. It accounts for 98% of the world's atmospheric oxygen production and avoids the increase in the concentration of CO_2, thus, preventing overheating the Earth due to the «greenhouse effect» [Idso, 1982; Sage, 1994] [Govindjee 1999] [IPCC reports]. Although, photosynthesis occurs in cells or organelles that are typically only a few microns (10^{-6} m), the process has a profound impact on the Earth's atmosphere and climate. Each year more than 10% of the total atmospheric carbon dioxide is reduced to carbohydrate by photosynthetic organisms. The humans and other animals breathe the oxygen released during photosynthesis. The sources of

atmospheric oxygen through photosynthesis are cyanobacteria and plankton in the ocean, and trees on land.

Humans are also dependent on ancient products of photosynthesis, known as fossil fuels that are supplying us with most of our energy [Govindjee, 1999]. These fossil fuels, including natural gas, coal, and oil, are composed of a complex mix of hydrocarbons, left by organisms that relied on photosynthesis millions years ago.

1.2 Brief history of discovery of photosynthesis

In the 1770s *Joseph Priestley* performed experiments showing that plants differed from animals in their effects on the air in the closed space [Priesley, 1776] [Govindjee, 1999] [Gregory, 1989]. He placed a mouse in the chamber with a burning candle and after several days showed that the candle extinguishes or the mouse dies. But if a green plant was added and illuminated in the chamber, the mouse could survive and the candle could burn in it. Although Priestley did not know about molecular oxygen, his work showed that plants release oxygen into the atmosphere.

Building on the work of Priestley, *Jan Ingenhousz* demonstrated that sunlight was necessary for photosynthesis and that only the green parts of plants could release oxygen [Ingenhousz. (1779)] [Gregory, 1989]. During this period *Jean Senebier* discovered that CO_2 is required for photosynthetic growth and *Nicolas-Theodore de Saussure* showed that water is required. It was not until 1841 that *Julius Robert von Mayer* proposed that photosynthetic organisms convert light energy into chemical free energy [Mayer , 1841] [Govindjee, 1999]. These five scientists profoundly contributed to the understanding of photosynthesis (Fig.1.1).

Important contributions to the field of photosynthesis have been made by *Lomonosov, Lavoisier* (oxygen theory), *Pelletier* and *Cavento* (isolation of chlorophyll), *Wilstatter* (chlorophyll and carotenoid purification and structure), *Calvin* (carbon-dioxide assimilation in photosynthesis) and many others excellent scientists.

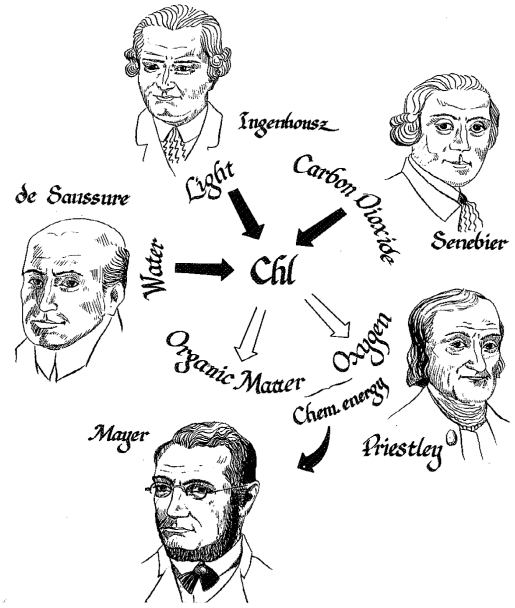

Figure 1.1 Discovers of photosynthesis [Rabinowitch, 1969].

A next stage in the investigation of photosynthesis was discovering of the structures of photosynthetic organisms. *Johann Deisenhofer*, *Hartmut Michel, Robert Huber* and co-workers in the 1980s determined the structure of the reaction center (RC) of the purple bacterium *Rhodospeudomonas viridis*. [Deisenhofer et al., 1984, 1985]. They were awarded the Nobel Prize for Chemistry in 1988 for their work, which has provided insight into the relationship between structure and function of membrane-bound proteins. This was just the first step in the long way of discoveries in the field of photosynthesis. Advances in crystallography, X-ray scattering, resonance spectroscopy and electron microscopy in combination with biochemical and physicochemical investigations allowed to obtain information about the structure of the tiny

photosynthetic machines. For example, electron paramagnetic resonance (EPR) spectroscopy is a very informative method to determine the electronic structure of paramagnetic species, which appear during the photosynthetic processes. The radicals formed in electron transfer in photosynthetic RCs can be often stabilized and studied with continuous wave EPR spectroscopy [Feher, 1978]. The investigation of short-lived intermediate states of photosynthetic processes was developed by transient and pulse EPR techniques [Stehlik, 1997] [Hoff, 1982] [Prisner, 2001] [Lubitz, 2002] [Lubitz, 2003].

A key element in photosynthetic energy conversion is the electron transfer (ET) within and between protein complexes. The ET reactions are rapid (as fast as a few picoseconds) and depend on many factors: temperature, redox potentials of partners, structure and specifications of partners etc. Much of our current understanding of the physical principles that guide the ET is based on the pioneering work of *Rudolph A. Marcus* [Marcus, 1985], who received the Nobel Prize in Chemistry in 1992 for his contributions to the theory of ET reactions in chemical systems.

1.3 What happens during photosynthesis?

By the middle of the 19th century the key features of plant photosynthesis were known, namely, that plants could use light energy to make carbohydrates from carbon dioxide and water. The empirical equation representing the net reaction of photosynthesis for oxygen evolving organisms is

$$6CO_2 + 12H_2O \xrightarrow{light\ energy, green\ plant} C_6H_{12}O_6 + 6O_2 + 6H_2O$$

The photosynthetic process consists of two main parts, the so-called “Light” and “Dark” reactions [Hall, 1988]. The products from these reactions are two energy-rich compounds: adenosine triphosphate (ATP) and reduced nicotinamide adenine dinucleotide phosphate (NADPH) [Gregory, 1989]. In the dark reactions, the products of the light part, ATP and NADPH, are used for biosynthesis of carbohydrates (sugars) from carbon dioxide. This happens in the so-called Calvin cycle or carbon fixation cycle [Bassham, 1950] [Diwan, 2005] [Martin, 2000]. In the light part two different membrane-bound photochemical assemblies called Photosystems I and II are working. Each photosystem operates in a series of photochemical reactions in membranes.

The first step of the light reactions is the absorption of light energy by conversion of a photon to an excited electronic state of a chromophore pigment molecule located in the antenna system [Owens, 1996]. Each antenna pigment is capable of absorbing photons at certain characteristic wavelengths [Kobayshi, 2006] (Fig.1.2*a*). The absorption spectra of the chromophore pigments in the photosynthetic organisms correspond to the action spectrum of photosynthesis [Rabinowitch, 1969] [Danks, 1983]. For example, chlorophylls absorb blue and red light and carotenoids absorb blue-green light, but green and yellow light are not effectively absorbed by photosynthetic pigments in plants; therefore, light of these colors is either reflected by leaves or passes through the leaves. This is the reason of the green colour of leaves.

In the dark the chlorophyll molecule is in a stable unexcited singlet state (S_0), and its electrons are on the basic energy level. When the chromophore molecule absorbs a photon, the electron is moved from the ground state S_0 to an energized or excited state S_n*. Depending on the wavelength of light excitation, the molecule can move up to different levels of the excited singlet state (Fig.1.2*b*). The lifetime of the chlorophyll molecules in the excited singlet state is very

short: S_2* - 10^{-12} - 10^{-13} s, S_1* - 10^{-9} - 10^{-7} s, after which the molecule returns to its original stable state S_0 through several pathways [Govindjee, 1999]. These processes can be described by the Jablonski scheme (Fig.1.2*b*).

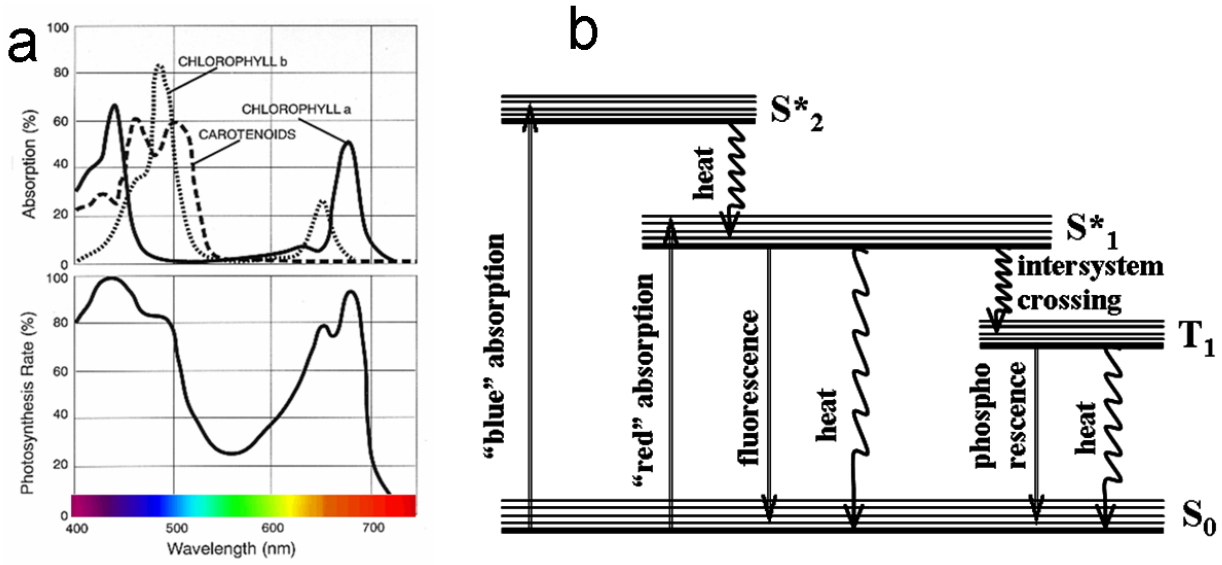

Figure 1.2 (*a*) The absorption spectrum of chloroplast pigments chlorophyll *a* and *b*, carotenoids along with the action spectrum of photosynthesis of a chloroplast [Govindjee, 1999] and (*b*) Jablonski energy diagram.

The electronic excited state is transferred to other antenna molecules as an exciton. Some excitons are converted back into photons and emitted as fluorescence or phosphorescence after singlet-triplet transitions by the intersystem crossing mechanism, some are converted to heat (Fig. 1.2*b*), and some are trapped by photosynthetic RC. Excitons trapped by RC provide the energy for the primary photochemical reaction of photosynthesis - the transfer of an electron from a donor molecule to an acceptor molecule. Both the donor and acceptor molecules are attached to the RC protein complex. Once primary charge separation occurs, the subsequent ET reactions are energetically downhill (diagram on Fig.1.5).

1.4 Organization of photosynthetic organisms

All living cells can be divided into two groups: prokaryotic and eukaryotic. Animals, plants, fungi, and algae all possess eukaryotic cell types. Bacteria and archea have prokaryotic cell types. Eukaryotic cells are generally much larger, have a nucleus and are more complex than prokaryotic cells. Because of their larger size, they require a variety of specialized internal membrane-bound organelles to carry out their metabolism, transport chemicals throughout the cell and provide energy [Nelson, 2008].

Photosynthetic prokaryotic organisms have membranous vesicles where photosynthetic pigments (chlorophyll molecules) are located. These structures are called thylakoids. In eukaryotes photosynthesis takes place in organelles called chloroplasts [Douglas, 1994] (Fig. 1.3). Chloroplasts are disk-shaped structures ranging from 5 to 10 micrometers in length, which can be observed easily as green grains by light microscopy [Heath, 1969]. They were first observed by *van Leeuwenhoek* in the 16th century, review of Leeuwenhoek work in [James, 1994]. Chloroplasts are surrounded by an inner (stroma) and an outer membrane (lumen). The stroma contains enzymes for photosynthetic reactions. This inner membrane consists of interconnected stacks called thylakoids, often arranged in stacks called grana or granum. The thylakoid membrane contains several protein complexes (Fig. 1.3), which participate in the light-dependent reactions of photosynthesis [Bryant, 1994] [Staehelin, 1996].

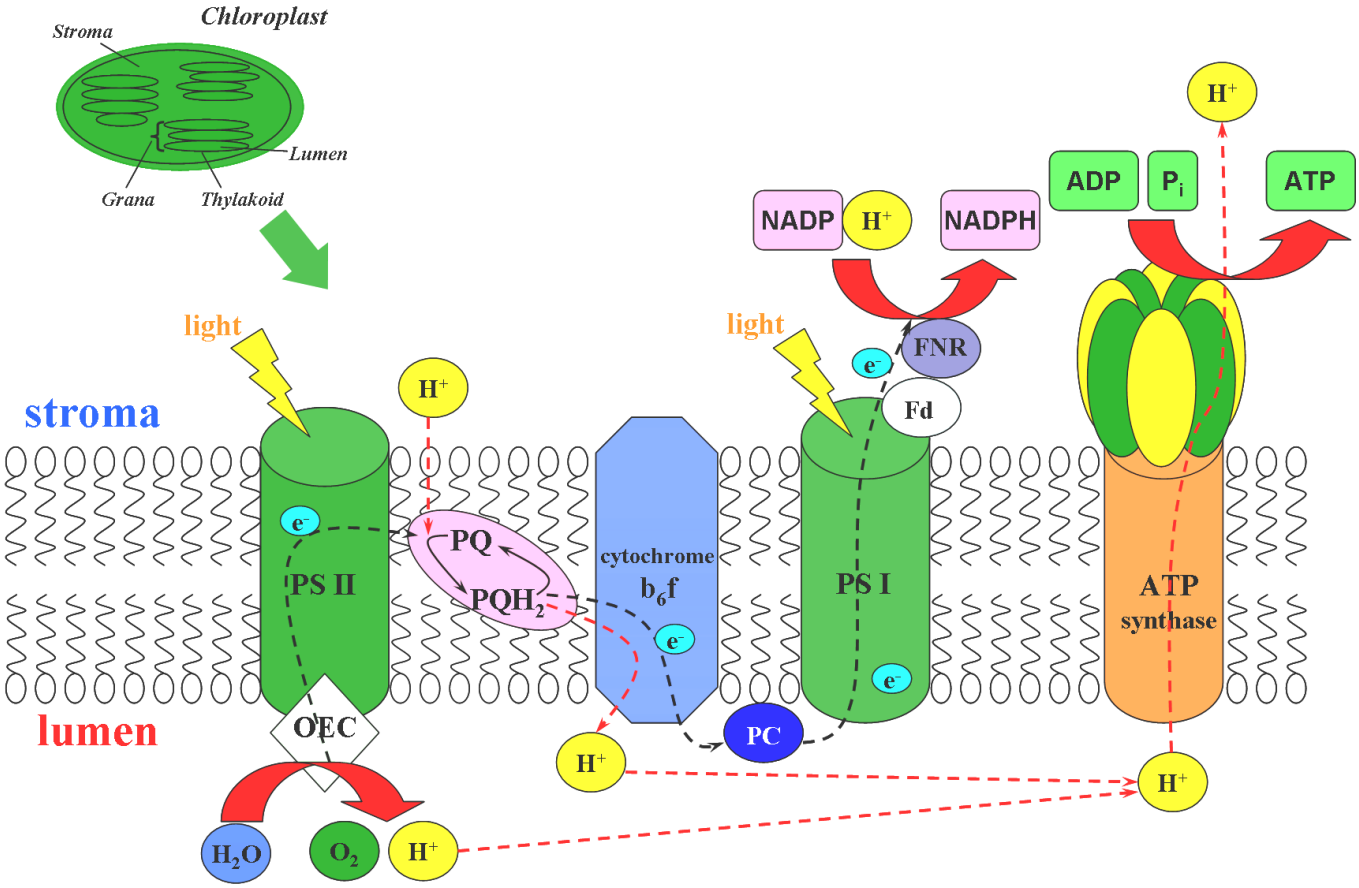

Figure 1.3 Structure of chloroplasts and the schematic model of the cyanobacterial thylakoid membrane with photosynthetic complexes. Abbreaviation: PS I (II) – photosystem I (II), PQ – plastoquinone, PC – plactocyanine, Fd – ferredoxin, FNR – ferredoxin-NADP reductase, ADP - adenosine diphosphate, P_i - phosphate, ATP - adenosine triphosphate, NADP and NADPH - nicotinamide adenine dinucleotide phosphate and its reduced form.

The pigments of the thylakoid membranes can absorb light of the whole solar spectrum due to the so called antenna complexes. Antenna pigments create singlet excitons which finally are trapped by the special pair of (bacterio)chlorophylls – the electron donor in the RC. For efficient energy transfer between the antenna and the primary electron donor of the RC, the donor absorbs at a longer wavelength, then transfers energy from antenna to the RC effectively.

RCs are bound in the photosynthetic membrane and are classified according to the identity of the terminal electron acceptors [Hillier, 2001] [Heathcote, 2002] [Vassiliev, 2001] (Fig. 1.4).

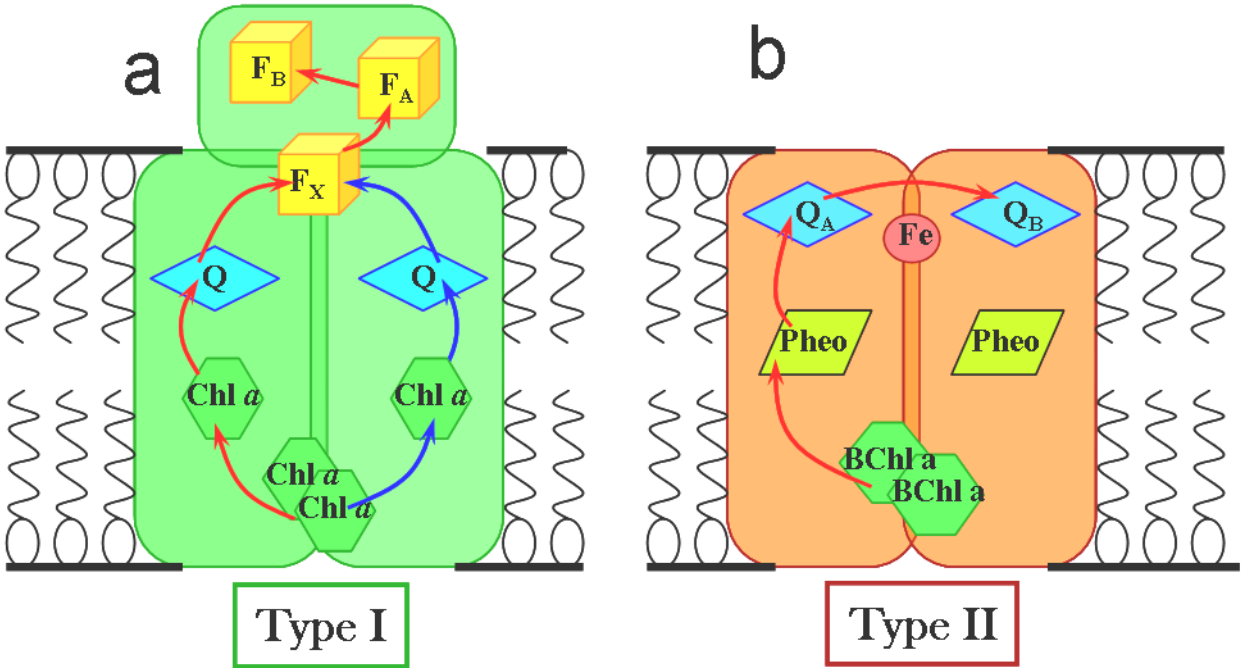

Figure 1.4 Types of photosynthetic reaction centers by the terminal acceptor. (*a*) Type I – Fe-S terminal acceptor, (*b*) Type II – quinone terminal acceptor.

Type I RC, also known as Fe–S type (Fig. 1.4*a*) possesses [4Fe-4S] clusters as terminal acceptors. Type I RC includes the photosystem of anoxygenic heliobacteria and green sulfur bacteria as well as Photosystem I of oxygenic photosynthetic organisms. The Type II RC or quinone type RC has quinones as terminal acceptor (Fig. 1.4*b*). This group is constituted by the RC of purple bacteria and Photosystem II of oxygenic photosynthetic organisms. While anoxygenic organisms contain a single photosynthetic RC complex – Type I or Type II, the oxygenic photosynthetic organisms, for example cyanobacteria, employ both types of RCs in

their membrane. As result they can oxidize water and reduce nicotinamide adenine dinucleotide phosphate ($NADP^+$).

1.5 Type II reaction centers

The first X-ray crystallographic structure of a photosynthetic RC has been resolved by Deisenhofer et al. in 1984 [Deisenhofer, 1984] [Deisenhofer, 1985], for which in 1988 the Nobel Prize was awarded. This structure was of the purple bacterial reaction center (bRC) from *Rhodopseudomonas viridis* with 3 Å resolution. The resolved structure allowed to conclude that the cofactors, which are responsible for light-driven ET, are arranged in two membrane spanning branches around an axis perpendicular to the plane of the membrane (pseudo-C_2 symmetry). These cofactors are bound to the L and M polypeptides, each of them contain five transmembrane α helices which are assembled around the axis of C_2 symmetry [Deisenhofer, 1985]. The photosystem II (PS II) is closely related to the bRC and has an ET chain and two subunits D1 and D2 that are similar to that of the purple bRC. The structure of PS II from the cyanobacteria *Synechococcus elongatus*, was determined with a resolution of 3.8Å [Zouni, 2001] and later with more precise resolutions [Kamiya, 2003] [J. Biesiadka, 2004] [B. Loll, 2005] [Guskov et al., 2009]. Photosystem II binds at least 99 cofactors - 35 chlorophyll *a* molecules, 12 β-carotenes, two pheophytins, three plastoquinones, two hemes, bicarbonate, 25 lipids, the $Mn_4Ca_1O_xCl_{1-2}(HCO_3)_y$ cluster (including a chloride ion), and one Fe^{2+} and one putative Ca^{2+} ion per monomer [Guskov et al., 2009].

The unique feature of PS II is the oxygen-evolving complex (OEC), which contains four manganese (Mn) ions (Mn_4 cluster), one calcium ion (Ca^{2+}) and one chlorine ion (Cl^-) as essential cofactors [Lindberg, 1993]. The OEC uses water as electron donor. The OEC can exist in

5 oxidation states created by light (the Kok cycle of S-states) [Yachandra, 2005]. When the OEC oxidizes water, producing dioxygen gas and protons, it delivers four electrons from water to a tyrosine (Y_Z) sidechain. The redox active tyrosine Y_Z (associated with the D1 subunit) acts as electron donor to PS II.

The ET chains in purple bRC and in PS II are highly similar. The ET chain consists of a dimer of two (bacterio)chlorophylls – the primary donor (P_{865}/P_{960} for purple bRC *R.sphaeroides* and *R.viridis*, respectively, and P_{680} for PS II), two (bacterio)pheophytins, two quinones Q_A and Q_B and non-heme iron (Fe) located between the two quinones [Deisenhofer, 1985]. The ET through the membrane in Type II RC is an asymmetric process using only one branch of cofactors attached to the L-subunit in purple bRC or the D1 subunit in PS II [Diner, 1996].

The electrons obtained in PS II from the water oxidation proceed through the cytochrome b_6f and are transferred via a plastocyanine – a small Cu-containing protein - to Photosystem I (Fig. 1.5). Plastocyanine (PC) has an essential role in photosynthesis, functioning as a last electron carrier in the chain between photosystems II and I [Sykes, 1985]. The electron flow between the two photosystems also generates a transmembrane proton gradient which is used to generate adenosine triphosphate (ATP) in the ATP synthase.

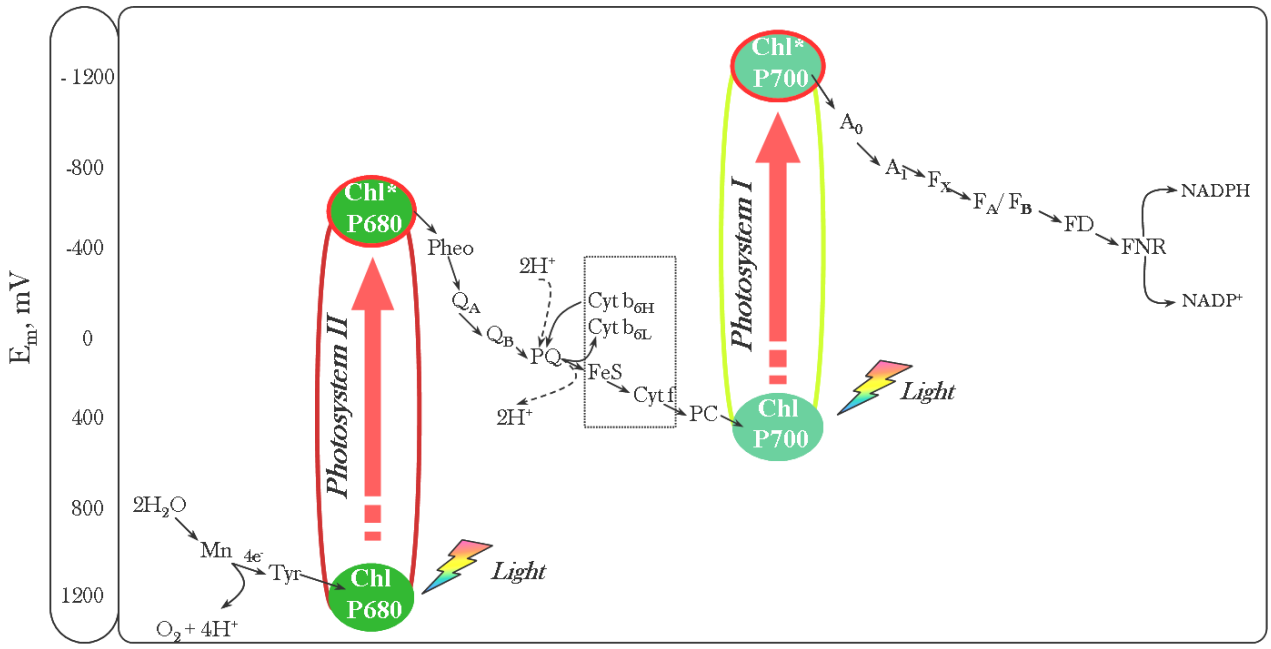

Figure 1.5 Z-scheme of photosynthesis in cyanobacterial organisms.

1.6 Type I reaction centers: Photosystem I

In oxygenic photosynthetic organisms – cyanobacteria, plants and algae – the PS II RC is working in cooperation with a Type I RC called photosystem I (PS I) (Z-scheme, Fig. 1.5). PS I is a membrane bound pigment protein complex that mediates the light-driven electron transfer from reduced plastocyanine or cytochrome c_6 to ferredoxin or flavodoxin (for review, see [Golbeck, 1994]).

Cyanobacterial PS I complexes can exist as monomers or trimers. The X-ray structure of PS I from *Synechococcus elongatus* at 2.5 Å resolution [Jordan, 2001] shows 12 protein subunits, which contain 126 cofactors: 96 chlorophyll *a* molecules (Chl *a*), 22 carotenoid molecules (Car), two phylloquinones (PhQ), three iron-sulfur clusters, four lipids, ~200 water molecules, and a metal ion (presumably Ca^{2+}).

The two largest subunits PsaA/PsaB bind 90 chlorophylls and 22 carotenoid molecules that function in the light absorption. Light is absorbed by the chlorophyll molecules

of the light-harvesting complex (LHC) and/or the core antenna [Fromme, 2003]. Then excitation energy is transferred to the P_{700} chlorophyll dimer [Brettel, 1997]. The assembly of the antenna chlorophylls in PS I is unique. The chlorophylls form a clustered network as an alternative to the symmetric ring of the light harvesting systems of purple bacteria [McDermott., 1995]. The antenna system is geometrically optimized for rapid energy transfer. Each antenna chlorophyll molecule has at least one neighboring chlorophyll molecule within a center-to-center distance of 15 Å that assure the highly effective energy transfer [Fromme, 2001]. A specific feature of the PS I antenna complex is the presence of "red" chlorophylls, which absorb light at longer wavelengths than P_{700} [Ratsep, 2000]. The excitation energy is then transferred from the antenna chlorophylls to the ET chain. There are two chlorophylls (named "connecting chlorophylls") that structurally seem to link the antenna system to the ET chain [Fromme, 2003].

Most of the redox cofactors involved in the ET process are connected to the largest subunits PsaA and PsaB: The ET cofactors are located in two branches A and B [Jordan, 2001] (Fig. 1.6*a*). The high resolution (2.5 Å) of the crystal structure of the PS I complex allowed to resolved that P_{700} is a heterodimer of chlorophyll *a* and *a'* (eC-A1/ec-B1) molecules which links to the PsaA and PsaB subunits by histidine nitrogen to the central Mg atom in each chlorophyll [Jordan, 2001] [Webber, 2001]. The dimeric structure and orientation of the donor P_{700} was supported by different EPR spectroscopically methods [Sieckmann, 1993] [Kass, 1995] [Kass, 2001] and X-ray structure analysis [Jordan, 2000]. The dimerization of chlorophylls and the asymmetric H-bonding environment (A-branch) of P_{700} result in a low potential of the donor (+ 0.4 V) [Plato, 2003]. It has been shown that spin density of the radical $P_{700}^{\bullet+}$ is located mostly on the B branch chlorophyll molecule [Krabben, 2000], [Webber, 2001].

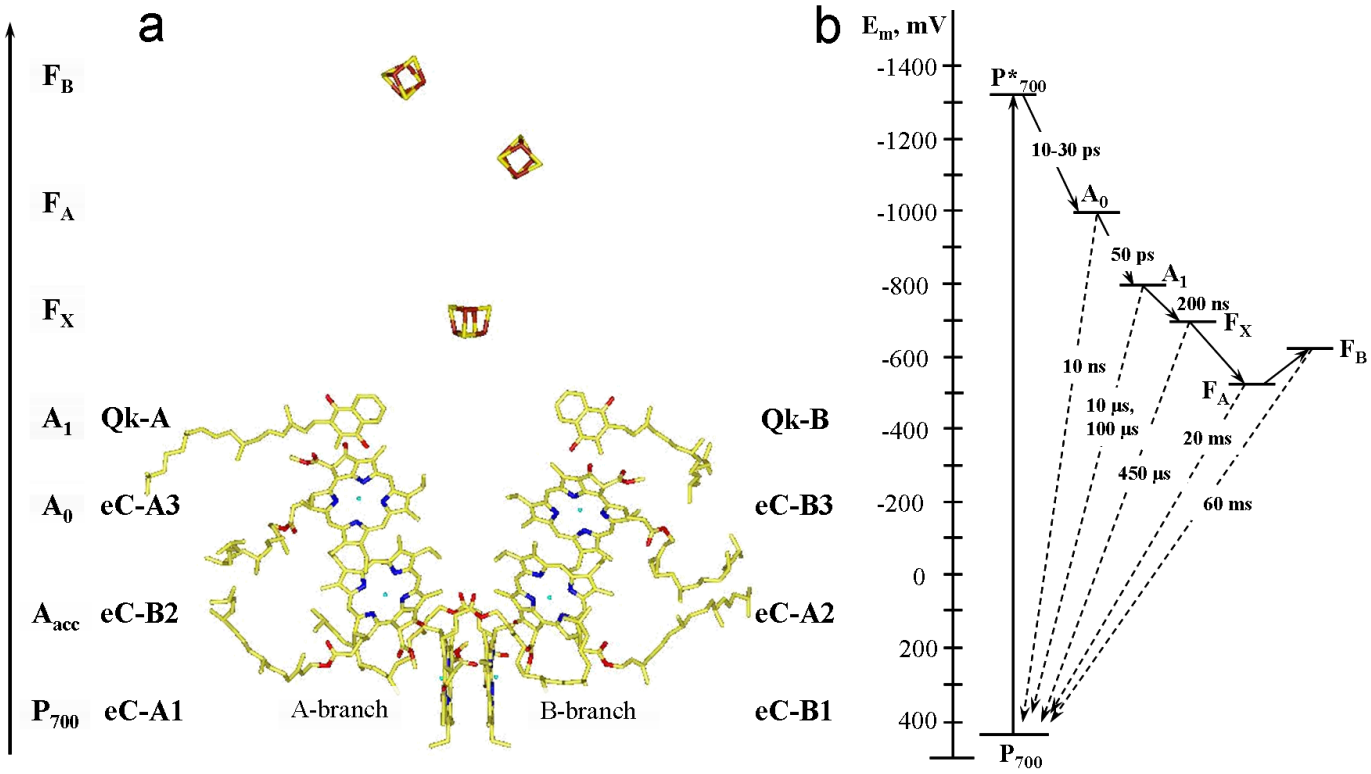

Figure 1.6 (*a*) Structure of the electron transfer chain in PS I (PDB entry 1JB0), (*b*) redox potentials of cofactors and time constants of electron transfer are given [Jordan, 2001] [van der Est, 2006].

There are two accessory Chl molecules (eC-B2/eC-A2) between the donor P_{700} and the primary acceptor A_0 that may be analogous of the monomeric bacteriochlorophylls in purple bRC [Jordan, 2001]. It has been recently hypothesized in the literature that the earliest step of ET (charge separation) can start from the accessory chlorophylls [Müller, 2003].

After charge separation process the electron is very rapidly (within 1- 2 ps) transferred to next redox cofactor A_0 [Trinkunas, 1996] [Savikhin, 2001], Fig.5.1*b* and the primary radical pair $P_{700}^{\bullet+}A_0^{\bullet-}$ is created. The primary acceptor A_0 is a monomer of Chl *a* (eC-A3/eC-B3), which has methionine sulfur as ligand (more details on the structure of A_0 can be found in Chapter 5). The redox potential of Chl *a* in A_0 binding site is ~ -1 V. The charge separated state $P_{798}^{\bullet+}A_0^{\bullet-}$ has a

lifetime of 10-30 ps before reduction by a secondary acceptor A_1, a quinone forming a phyllosemiquinone anion radical $A_1^{\bullet-}$ [Brettel, 1997] (Fig.2.4*b*).

Two phylloquinone molecules (Qk-A/Qk-B) have been found in each of the branches of the ET chain. The A_1 acceptor was tentatively identified as a quinone based on EPR [Snyder, 1991] [Heathcote, 1993] and absorption difference [Brettel, 1986] spectra. The recent EPR studies of radical A_1^- allowed explaining the unique properties of the phylloquinone molecule in the A_1 protein binding site [Niklas, 2009]. The binding site of A_1 for phylloquinone consists of a single H-bond with protein backbone and π-stacking with a tryptophane [Jordan, 2000] [Niklas, 2009]. The corresponding redox potential of the quinone in the A_1 binding site is ~ - 810 mV [Iwaki, 1994]. The directionality of the ET is still a matter of discussion in the literature [Redding, 2006] [Brettel, 2001] [Santabarbara, 2005] [Niklas, 2009].

In the next step of the ET, the electron proceeds from cofactor A_1 to cofactor F_X. The rate for the ET step $P_{700}^{\bullet+}A_1^{\bullet-} \rightarrow P_{700}^{\bullet+}F_X^{\bullet-}$ (about 200 ns) was detected by transient EPR at high temperature [van der Est, 1994]. F_X is a [4Fe-4S] iron-sulfur cluster and its binding site is composed of four cysteines provided by PsaA and PsaB. F_X participates as redox-active component in forward electron transfer between the PsaA/PsaB and the PsaC subunit. Like all components in the redox chain, its redox potential is very low, about − 700 mV [Chamorovsky, 1982].

The terminal electron acceptors F_A and F_B (two [4Fe-4S] iron sulfur clusters) are both linked to the subunit PsaC, one of the three extrinsic subunits located on the stromal side of PS I [Antonkine, 2006]. The function of F_A and F_B clusters is to forward the electron transfer from F_X to soluble ferredoxin or flavodoxin, which means moving out the electrons from the hydrophobic RC to the hydrophilic stromal side. PS I does not reduce $NADP^+$ directly but via a ferredoxin

dependent dehydrogenase. Ferredoxin may also participate in cyclic electron transport by routing electrons back to the cytochrome b_6 complex [Setif, 2006].

1.7 Antenna pigments in photosynthetic reaction centers

All photosynthetic organisms contain pigments able to absorbing of the light and initiate the photochemical reactions. The chlorophylls (Chls) are most important among them. Chls are probably the most widely-distributed biological pigments on Earth. The name of *chlorophyll* was first used by Pelletier and Caventou in 1818 to describe the green pigment of plants [Pelletier, 1818]. In 1906 a Russian botanist Tswett has first separated Chl *a* and Chl *b* from the alcoholic extract by means of powdered sugar column chromatography [Tswett, 1906], and later bacteriochlorophylls (BChls) were also found in nature [Fischer, 1938] [Jensen ,1964].

The structure of Chl *a* was elucidated by Hans Fisher [Fisher, 1940]. Chls are part of the class of chemical components called porphyrins. Chls are dihydroporphyrins (ring IV is partially saturated) having a unique cyclopentanone ring, ring V, as shown in Fig.1.7. Chlorophyll *a* is a planar molecule composed of a 'head' and a 'tail'. The head consists of a porphyrin ring (cyclic tetrapyrrole), from which extends a tail made up of a 20-carbon grouping called the phytol. Phytol is a long straight chain alcohol containing a double bond. Its formula is $C_{20}H_{39}$. Four nitrogens in the porphyrins usually surround a metal atom. In chlorophyll the central metal atom is magnesium (Mg).

Chl *a* is present in RCs (PS I and PS II, heliobacterial RC) and in all light-harvesting complexes (LHC). The core antenna of PS I is composed of 90 Chl *a* molecules and 22 carotenoid molecules. Structurally, the Chls in the antenna complex of PS I are organized in

three domains [Jordan, 2001]: a central domain which surrounds the RC; two peripheral domains which is located on the stromal and luminal sides. In the core antenna of some cyanobacterial PS I complexes Chls were found which have very broad "red"-shifted absorption spectra. These are so called "red" chlorophylls. The properties of the "red" Chls are explained by a strong excitonic interaction between neighboring Chls and high electron-photon coupling [Gobets, 1994] [Palsson, 1996] [Ratsep, 2000] [Zazubovich, 2002].

The absorption spectrum of the Chl *a* is characterized by a strong Soret band at 430 nm and a relatively strong Q_y band at 670 nm. The weak band at 580 nm is the Q_x transition. The intense absortivity in the visible region is an important factor in light-harvesting by a Chl *a*. This is the reason why Chl *a* is the major pigment in all chlorophyllous antenna complexes of oxygenic organisms. However, the intense bands of Chl a are quite narrow, and there is only moderate absortivity in the green spectral range. In antenna, it is therefore almost always supplemented by additional light-harvesting pigments.

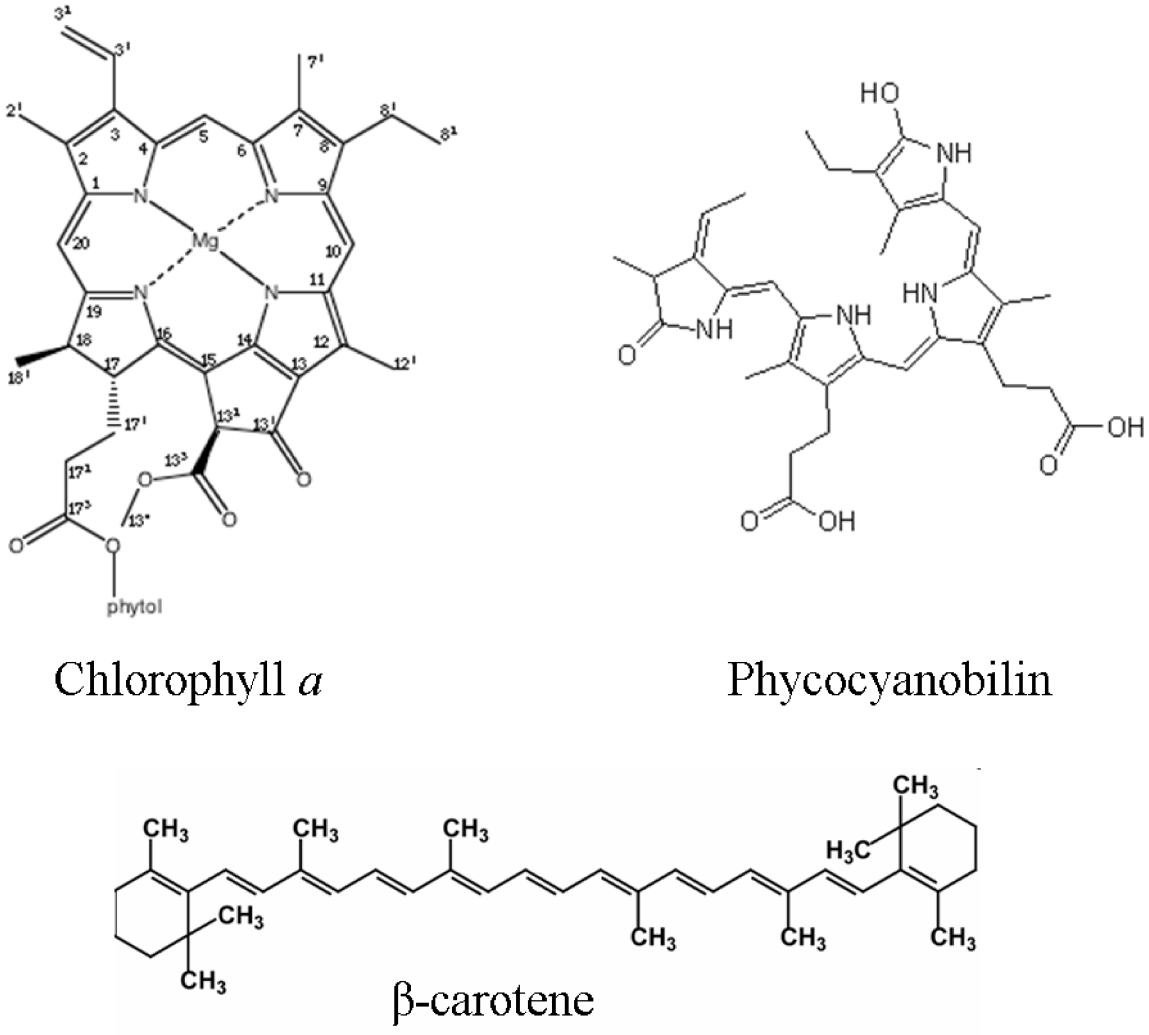

Figure 1.7 Basic antenna pigments in photosynthetic antenna complexes.

As part of the antenna system in PS I, carotenoids absorb blue light in the 450-570 nm range, where the chlorophyll pigments do not and transfer the energy to the chlorophylls. For example, the X-ray crystal structure of the cyanobacterial PS I shows that all the carotenoids are β-carotenes, which are oriented close to the membrane plane [Jordan, 2001] (Fig.1.7). In cyanobacteria and other carotenoid-producing organisms carotenoids are synthesized from isoprenoid precursors in membranes [Govindjee, 1999]. Carotenoids in cyanobacteria have two main functions: light-harvesting and protection from photooxidation damage [Cogdell, 1987].

The danger of photooxidation damage arises from the excited triplet state of chlorophyll. Carotenoid molecules with π-electron conjugation of nine or more carbon-carbon double bonds can absorb triplet state energy from excited chlorophyll:

$$^1Car + {}^3Chl^* \rightarrow {}^3Car^* + {}^1Chl$$

and prevent the formation of destructive singlet-state oxygen radicals[Cogdell, 1987]:

$$^3O_2 + {}^3Chl^* \rightarrow {}^1O_2^* + {}^1Chl.$$

This reaction is called the "photodynamic reaction" (or "photo-oxidative killing"). Carotenoids can protect the reaction center against damage by near ultra-violet (UV) irradiation [Buckley, 1976]. Because of the ability to quench oxygen radical, carotenoids are good anti-oxidants and they can protect cells from oxidative breakage.

The cyanobacterial antenna system contains also photosynthetic pigments which absorb solar energy in the visible range (red, orange, yellow and green) where absorption of chlorophylls is low. These pigments are called biliproteins [Ke, 2001]. The bilins are linear tetrapyrroles, which derive from cyclic tetrapyrroles (e.g. chlorophyll) by oxidation and removal of a carbon bridge. Blue pigments are phycocyanobilins (Fig. 1.7) and the red pigments are phycoerythrins [Ke, 2001].

Bibliography to Chapter 1

Amunts A., Drory O. and Nelson N. (2007) The Structure of a Plant Photosystem I Supercomplex at 3.4 Å Resolution. Nature, 447, 58-63.

Antonkine M.L. (2006) Molecular Interactions of the Stromal Subunit PsaC with the PsaA/PsaB Heterodimer. In: Golbeck J.H. (eds) Photosystem I: The Light-Driven Plastocyanin: Ferredoxin Oxidoreductase. Advances in Photosynthesis and Respiration, vol 24, 79-98. Publishers: Springer, Dordrecht.

Bassham J.A., Benson A.A., and Calvin M. (1950) Path of Carbon in Photosynthesis. J.Biol.Chemistry, 185, 781-787.

Biesiadka J., Loll B., Kern J., Irrgang K.D., Zouni A. (2004) Crystal Structure of Cyanobacterial Photosystem II at 3.2 Å Resolution: a Closer Look at the Mn-cluster. Phys. Chem. Chem. Phys., 6, 4733-4736.

Brettel, K. (1997) Electron Transfer and Arrangement of the Redox Cofactors in Photosystem I. Biochimica et Biophysica Acta, 1318, 322-373.

Brettel, K., Leibl W. (2001) Electron Transfer in Photosystem I. Biochimica et Biophysica Acta, 1507, 1-15.

Bryant, D.A. (1994) Molecular Biology of Cyanobacteria. Publishers: Kluwer, Netherlands.

Buckley C.E., Houghton J.A. (1976) Study of Effects of Near UV-radiation on Pigmentation of Blue-green Alga *Gloeocapsa Alpicola*. Arch.Microbiology, 107, 93-97.

Chamorovsky S.K. and Cammack R. (1982) Direct Determination of the Midpoint Potential of the Acceptor-X in the Chloroplast Photosystem I by Electrochemical Reduction and

Electron Spin Resonance Spectroscopy. Photobiochemistry and Photobiophysics, 4, 195-200.

Cogdell R.J., Frank H.A. (1987) How Carotenoids Function in Photosynthetic Bacteria. Biochimica et Biophysica Acta, 895, 63-79.

Collings A.F., Critchley C. (2005) Artificial Photosynthesis: From Basic Biology to Industrial Application. Publisher: Wiley Verlag Gmbh.

Danks S.M, Evans E.H., and Whittaker P.A. (1983) Photosynthetic Systems: Structure, Function, and Assembly. Publishers: Chichester New York: Wiley.

Deisenhofer J., Epp O., Miki K, Huber R. and Michel H. (1984). X-Ray Structure Analysis of a Membrane-Protein Complex. J.Mol.Biology, 180, 385-398.

Deisenhofer J., Epp O., Miki K, Huber R. and Michel H. (1985) Structure of Protein Subunits in the Photosynthetic Reaction Center of *Rhodopseudomonas viridis* at 3 Å Resolution. Nature, 318, 618-624.

Diner B.A. and Babcock G.T. (1996) Structure, Dynamics, and Energy Conversion Efficiency in Photosystem II. In: Ort D.R. and Yocum C.F. (eds) Oxygenic Photosynthesis: The Light Reactions. Advances in Photosynthesis and Respiration, vol 4, 213-247, Publishers: Springer, Dordrecht.

Diner B.A., Schlodder E., Nixon P.J., Coleman W.J., Rappaport F., Lavergne J., Vermaas W.F.J., Chisholm D.A. (2001) Site-directed Mutations at D1-His198 and D2-His 97 of Photosystem II in *Synechocystis* PCC 6803: Sites of Primary Charge Separation and Cation and Triplet Stabilization. Biochemistry, 40, 9265-9281.

Diwan J.J. (2005). Photosynthetic Dark Reaction at Biology: Exploring Life by Neil A Campbell et al. Publishers: Boston, Mass.

Douglas S.E. (1994) Chloroplast Origins and Evolution. In: Bryant D.A. (ed) The Molecular Biology of Cyanobacteria. Advances in Photosynthesis and Respiration, vol 1, 91-118, Publishers: Springer, Dordrecht.

Ermler U., Michel H., and Schiffer M. (1994) Structure and Function of the Photosynthetic Reaction Center from *Rhodobacter* sphaeroides. J.Bioenergetics and Biomembranes, 26, 5-15.

Feher G. and Okamura M.Y. (1978) Chemical Composition and Properties of Reaction Centers. In: Clayton R.K. and Sistrom W.R. (eds.) Photosynthetic Bacteria, p. 349-386, Publisher: Plenum, New York.

Frank, H.A. and Cogdell R.J. (1996) Carotenoids in Photosynthesis. Photochemistry and Photobiology, 63(3), 257-264.

Fromme P., Schlodder E. and Jansson S. (2003) Structure and Function of the Antenna System in Photosystem I. In: Green B.R. and Parson W.W. (eds) Light-Harvesting Antennas in Photosynthesis. Advances in Photosynthesis and Respiration, vol. 13, 253-279, Publishers: Springer, Dordrecht.

Golbeck J.H. (1987) Structure, Function and Organization of the Photosystem I Reaction Center Complex. Biochimica et Biophysica Acta, 895 167-204.

Golbeck J.H. (1994) Photosynthetic Reaction Centers: So Little Time, So Much to Do. Biophysics Textbook Online.

Golbeck J.H. (2003) The Binding of Cofactors to PhotosystemI Analyzed by Spectroscopic and Mutagenic Methods. Annu. Rev. Biophys. Biomol. Structure 32 237–256.

Govindjee (1999) Carotenoids in Photosynthesis: a Historical Perspective. In: Frank H.A., Young A.J., Britton G. and Cogdell R.J. (eds) The Photochemistry of Carotenoids. Advances in Photosynthesis and Respiration, vol. 8, 1-19 Publishers: Springer, Dordrecht.

Govindjee, Whitmarsh J. (1999) Concepts in Photobiology: Photosynthesis and Photomorphogenesis, Edited by Singhal G.S., Publishers: New Delhi and Kluwer Academic, Dordrecht.

Gregory R. P. F. (1989) Biochemistry of Photosynthesis. Publishers: John Wiley & Sons, London.

Gregory R.P.F. (1989) Photosynthesis. Publishers: Chapman & Hall, New York, USA.

Guskov A., Kern J., Gabdulkhakov A., Broser M., Zouni A., Saenger W. (2009) Cyanobacterial Photosystem II at 2.9 Å Resolution and the Role of Quinones, Lipids, Channels and Chloride. Nature Struct. and Molec. Biology, 16, 334-342.

Hall D.O., Rao K.K., (1999) Photosynthesis. Publishers: Cambridge University Press.

Hauska G., Schütz M. and Büttner M. (1996) The Cytochrome b_6f Complex - Composition, Structure and Function. In: Ort D.R. and Yocum C.F. (eds) Oxygenic Photosynthesis: The Light Reactions. Advances in Photosynthesis and Respiration, vol. 4, 377-398. Springer, Dordrecht.

Heathcote P., Fyfe P.K., Jones M.R. (2002) Reaction Centres: the Structure and Evolution of Biological Solar Power. TRENDS in Biochemical Sciences. 27, 79-87.

Heathcote P., Jones M.R., Fyfe P.K. (2003) Type I Photosynthetic Reaction Centres: Structure and Function. Phil. Trans. R. Soc. Lond. B, 358, 231–243

Heath O.V.S. (1969) The Physiological Aspects of Photosynthesis. Publishers: Stanford University Press.

Hillier W. and Babcock G.T. (2001) Photosynthetic Reaction Centers. Plant Physiology, 125, 33–37.

Hoff A. J. (1982) ESR and ENDOR of Primary Reactants in Photosynthesis. Biophys. Struct. Mechanisms, 8, 107-150.

Idso, S.B. (1982) Carbon Dioxide: Friend or Foe? Publishers: IBR Press, Tempe, USA.

Ingenhousz J. (1779) Experiments upon Vegetables, Discovering their Great Power of purifying the Common Air in the Sun-shine, and of Injuring it in the Shade and at Night. To which is Joined, A New Method of Examining the Accurate Degree of Salubrity of the Atmosphere London.

IPCC assessment reports, see http://www.ipcc.ch/

Iwaki M., Itoh S. (1994) Reaction of Reconstituted Acceptor Quinone and Dynamic Equilibration of Electron Transfer in the Photosystem I Reaction Center. Plant Cell Physiology, 35, 983–993.

James, J. (1994) van Leeuwenhoek's Discoveries of 1677-1678 - A Look Too Far, Micron, 25, 1-4.

Jordan P., Fromme P., Witt H.T., Klukas O., Saenger W., Krauss N. (2001) Three-dimensional Structure of Cyanobacterial Photosystem I at 2.5 Å Resolution. Nature, 411, 909-917.

Kaas H., Fromme P., Witt H.T. and Lubitz W. (2001) Orientation and Electronic Structure of the Primary Donor Radical Cation P_{700}^{+} in Photosystem I: Single Crystal EPR and ENDOR Study. J. Phys. Chemistry, 105, 1225-1239.

Kamiya N. and Shen J.R. (2003) Crystal Structure of Oxygen-evolving Photosystem II from *Thermosynechococcus vulcanus* at 3.7 Å Resolution. PNAS, 100, 98-103.

Ke B (2001) Phycobiliproteins and phycobilisomes. In: Govindjee (eds) Photosynthesis: Photobiochemistry and Photobiophysics. Advances in Photosynthesis and Respiration, vol 10, 251-269 Publishers: Springer, Dordrecht.

Klukas O., Schubert W.O., Jordan P. et al (1999) Localization of Two Phylloquinones, Q(K) and Q(K)1, in an Improved Electron Density Map of Photosystem I at 4 Å Resolution. J. Biol. Chemistry, 274, 7361-7367.

Krabben L., Schlodder E., Jordan R., Carbonera D., Giacometti G., Lee H., Webber A.N., Lubitz W. (2000) Influence of the Axial Ligands on the Spectral Properties of P700 of Photosystem I: A Study of Site-directed Mutants. Biochemistry, 39, 13012-13025.

Lindberg K., Vanngard T., Andereasson L.E. (1993) Studies of the Slowly Exchanging Chloride in Photosystem II of Higher Plants. Photosynth. Res., 38, 401-408.

Loll B., Kern J., Saenger W., Zouni A., Biesiadka J. (2005) Towards Complete Cofactor Arrangement in the 3.0 Å Resolution Structure of Photosystem II. Nature, 438, 1040-1044.

Lubitz W. (2002) Pulse EPR and ENDOR Studies of Light-induced Radicals and Triplet States in Photosystem II of Oxygenic Photosynthesis. Phys. Chem. Chem. Phys., 4, 5539–5545.

Lubitz W. (2003) Photochemical Processes in Photosynthesis Studied by Advanced Electron Paramagnetic Resonance Techniques. Pure Appl. Chemistry, 75, 1021–1030.

Lubitz W. (2006) EPR Studies of the Primary Electron Donor P700 in Photosystem I. In: Golbeck J.H. (ed) Photosystem I: The Light-Driven Plastocyanin: Ferredoxin Oxidoreductase. Advances in Photosynthesis and Respiration, vol. 24, 245-269, Publishers: Springer, Dordrecht.

Marcus R.A. and Sutin N. (1985) Electron transfer in Chemistry and Biology. Biochimica et Biophysica Acta, 881, 265-322.

Martin W, Scheibe R. and Schnarrenberger C. (2000) The Calvin Cycle and its Regulation. In: Leegood R.C., Sharkey T.D. and von Caemmerer S. (eds) Photosynthesis: Physiology and Metabolism. Advances in Photosynthesis and Respiration, vol.9. Publishers: Springer, Dordrecht, pp. 9-51.

Mayer, Robert (1841). Remarks on the Forces of Nature; as quoted in: Lehninger, A. (1971). Bioenergetics - the Molecular Basis of Biological Energy Transformations, 2nd ed. Publishers: The Benjamin/Cummings Publishing Company, London.

McDermott G. , Prince S.M., Freer A.A., Hamthornthwaitelawless A.M., Papiz M.Z., Cogdell R.J., Isaacs N.W. (1995) Crystal Structure of an Integral Membrane Light-harvesting Complex from Photosynthetic Bacteria. Nature, 374, 517-521.

Müller, M. G., Niklas, J., Lubitz, W., Holzwarth, A. R. (2003) Ultrafast Transient Absorption Studies on Photosystem I Reaction Centers from *Chlamydomonas reinhardtii*. 1. A New Interpretation of the Energy Trapping and Early Electron Transfer Steps in Photosystem I. Biophysical Journal, 85, 3899-3922

Nelson D.L., Cox M.M. (2008) Principles of Biochemistry. 5th ed. Publisher: Freeman, New York.

Niklas J., Epel B., Antonkine M.L., Sinnecker S., Pandelia M. and Lubitz W. (2009) Electronic Structure of the Quinone Radical Anion $A_1^{\bullet -}$ of Photosystem I Investigated by Advanced Pulse EPR and ENDOR Techniques. J. Phys. Chemistry B, accepted.

Owens T.G. (1996) Processing of Excitation Energy by Antenna Pigments. In: Baker N.R. (ed) Photosynthesis and the Environment. Advances in Photosynthesis and Respiration, vol 5. Publishers: Springer, Dordrecht, pp. 1-23.

Plato M., Krauss N., Fromme P., Lubitz W. (2003) Molecular Orbital Study of the Primary Electron Donor P700 of Photosystem I Based on a Recent X-ray Single Crystal Structure Analysis. Chem. Physics, 294, 483-499.

Priestley J. (1775) Experiments and Observations on Different Kinds of Air. 2nd ed. Printed for J. Johnson, London.

Prisner T., Rohrer M, and MacMillan F. (2001) Pulsed EPR Spectroscopy: Biological Applications. Annu. Rev. Phys. Chemistry, 52, 279–313.

Prokhorenko V.I., Holzwarth A.R. (2000) Primary Processes and Structure of the Photosystem II Reaction Center: A Photon Echo Study. J. Phys. Chemistry B, 104, 11563-11578.

Rabinowitch E., Govindjee (1969). Photosynthesis. Publishers: Wiley, New York, London, Sydney and Toronto.

Ratsep M., Johnson T.W., Chitnis P.R., Small G.J. (2000) The Red-absorbing Chlorophyll a Antenna States of Photosystem I. J. Phys. Chemistry B, 104, 836-847.

Redding K. and van der Est A. (2006) The Directionality of Electron Transport in Photosystem I. In: Golbeck J.H. (eds) Photosystem I: The Light-Driven Plastocyanin: Ferredoxin Oxidoreductase. Advances in Photosynthesis and Respiration, vol. 24, 413-437, Publishers: Springer, Dordrecht.

Sage R.F. (1994) Acclimation of Photosynthesis to Increasing the Atmospheric CO_2. Photosynth. Research, 39, 351-368.

Santabarbara S., Heathcote P. and Evans M. C. W. (2005) Modeling of the Electron Transfer Reactions in Photosystem I by Electron Tunneling Theory. Biochimica et Biophysica Acta, 1708, 283-310.

Scheer H (2003) The Pigments. In: Green B.R. and Parson W.W. (eds) Light-Harvesting Antennas in Photosynthesis. Advances in Photosynthesis and Respiration, vol. 13. Publishers: Springer, Dordrecht, pp 29-81.

Scheer H. (2006) An Overview of Chlorophylls and Bacteriochlorophylls: Biochemistry, Biophysics, Functions and Applications. In: Grimm B., Porra R.J., Ruediger W. and Scheer H. (eds) Chlorophylls and Bacteriochlorophylls: Biochemistry, Biophysics, Functions and Applications. Advances in Photosynthesis and Respiration, vol 25, 1-26, Publishers: Springer, Dordrecht.

Schubert W., Klukas O., Saenger W., Witt H.T., Fromme P. and Krauss N. (1998) A Common Ancestor for Oxygenic and Anoxygenic Photosynthetic Systems: A Comparison Based on the Structural Model of Photosystem I. J. Mol. Biology, 280, 297-314.

Setif P (2006) Electron Transfer from the Bound Iron-sulfur Clusters to Ferredoxin/flavodoxin: Kinetic and Structural Properties of Ferredoxin/flavodoxin Reduction by Photosystem I. In: Golbeck JH (ed) Photosystem I: The Light-Driven Plastocyanin: Ferredoxin Oxidoreductase. Advances in Photosynthesis and Respiration, vol 24, 439-454, Publishers: Springer, Dordrecht.

Srinivasan N, Golbeck J.H. Protein–cofactor Interactions in Bioenergetic Complexes: The Role of the A_{1A} and A_{1B} Phylloquinones in Photosystem I. Biochim. Biophys. Acta, 2009.

Staehelin L.A. and van der Staay G.W.M. (1996) Structure, Composition, Functional Organization and Dynamic Properties of Thylakoid Membranes. In: Ort D.R. and Yocum

C.F. (eds) Oxygenic Photosynthesis: The Light Reactions. Advances in Photosynthesis and Respiration, vol 4, 11-30, Publishers: Springer, Dordrecht.

Stehlik D. and Möbius K. (1997) New EPR Methods for Investigating Photoprocesses with Paramagnetic Intermediates. Annu. Rev. Phys. Chemistry, 48, 745.

Sykes A.G. (1985) Structure and Electron Transfer Reactivity of the Blue Copper Protein Plastocyanin. Chem. Soc. Reviews, 14, 283-315.

van der Est A (2006) Electron Transfer Involving Phylloquinone in Photosystem I. In: Golbeck J.H. (ed) Photosystem I: The Light-Driven Plastocyanin: Ferredoxin Oxidoreductase. Advances in Photosynthesis and Respiration, vol 24, 387-411, Publishers: Springer, Dordrecht.

Vassiliev I.R., Antonkine M.L., Golbeck J.H. (2001) Iron-sulfur Clusters in Type I Reaction Centers. Biochimica et Biophysica Acta, 1507, 139-160.

Webber A.N., Lubitz W. (2001) P700: the Primary Electron Donor of Photosystem I. Biochimica et Biophysica Acta, 1507, 61-79.

Yachandra V.K. (2005) The Catalytic Manganese Cluster: Organization of the Metal Ions. In: Wydrzynski T.J. and Satoh K. (eds) Photosystem II: The Light-Driven Water: Plastoquinone Oxidoreductase. Advances in Photosynthesis and Respiration, vol 22, 235-260, Publishers: Springer, Dordrecht.

Zouni A., Witt H.T., Kern J., Fromme P., Krauss N., Saenger W., Orth P. (2001) Crystal Structure of Photosystem II from *Synechococcus elongatus* at 3.8 Å Resolution. Nature, 409, 739-743.

Chapter 2. Principles of electron paramagnetic resonance

Electron paramagnetic resonance (EPR) spectroscopy is an effective method for studying systems containing one or more unpaired electrons. States with free electrons are often short-lived, but still play crucial roles in many processes such as photosynthesis, oxidation, catalysis, and polymerization reactions. In proteins paramagnetic molecules can be stable cofactors (*e.g.* heme molecules, iron-sulfur clusters, or metal ions); short-lived radicals in reactions (chromophores); or artificial spin labels attached to the protein.

EPR spectroscopy can provide detailed information on the electronic structure. Magnetic parameters such as: the *g* value, hyperfine couplings, and nuclear quadrupole interactions are directly relate to the arrangement of the surrounding nuclei. Hyperfine couplings (hfc) are related to the spin populations and can be used to measure distances between the nuclei and the unpaired electron; nuclear quadrupole interactions provide information on the bonding of nuclei and zero-field splittings often provide information about the type of paramagnetic species.

In powders and frozen solutions, many of the hyperfine and nuclear-quadrupole splittings are not resolved in the field-swept EPR spectrum. Therefore, the pulsed electron nuclear double resonance (ENDOR) can be applied for more precise determination of the hfs parameters. ENDOR and electron-spin-echo envelope-modulation (ESEEM) methods give much higher spectral resolution by directly measuring nuclear frequencies.

2.1 Basic principles of electron paramagnetic resonance (EPR)

Electron paramagnetic resonance describes the phenomena of resonant absorption of microwave radiation by paramagnetic ions or molecules, with at least one unpaired electron spin, in the presence of a static magnetic field. The EPR effect was discovered at Kazan State University by Zavoisky in 1944 [Zavoisky, 1944].

Let us assume that a particle with spin S = ½ interacts with the external magnetic field B_0. Due to the Zeeman effect, the energy levels split depending on the strength of the external magnetic field B_0. If electromagnetic radiation is applied at the frequency that corresponds to the separation between two energy levels, energy is absorbed from the electromagnetic field (Fig. 2.1).

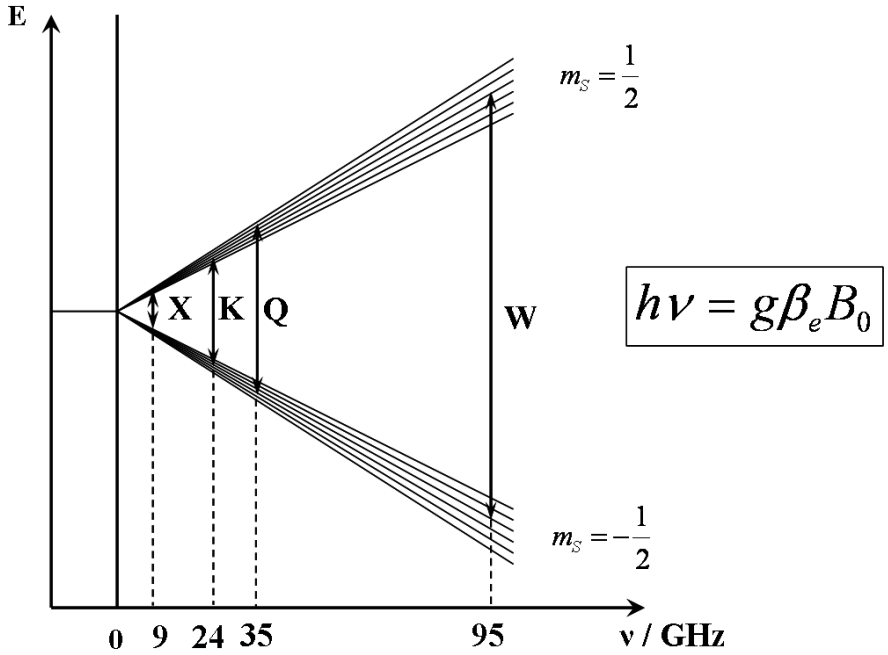

Figure 2.1 Schematic representation of the energy levels for electron spin S = ½ and resonance conditions.

When a variable magnetic field (microwave field) with an energy $h\nu$ is applied to this system, and B_0 is scanned, a resonance transition takes place when ΔE between the two states

becomes equal to $h\nu$: $h\nu = g\beta_e B_0$. This equation is the EPR condition, which determines the resonance position; it contains two variables, the microwave frequency ν and the magnetic field B_0.

EPR spectra are generally obtained by scanning the magnetic field to find the resonance position with a fixed microwave frequency. The most often frequency used is 9 GHz, called X-band. Higher field (frequency) EPR measurements are needed to detect subtle spectroscopic details [Mobius, 2005, Mobius, 2009]. The lineshape of EPR spectrum depends on the interplay of magnetic field dependent (Zeeman interaction) and magnetic field independent (hyperfine, dipole-dipole) terms. By operating at several frequencies, contributions from different interactions can be analyzed. Other commonly used frequency bands are K-(24 GHz), Q-(35 GHz) and W-(95 GHz) (Fig. 2.1). A major advantage of high field EPR is enhanced g factor resolution and sensitivity.

In EPR spectroscopy, we observe the resonance transition between two spin populations N_A and N_B. The population of spins in the lower energy level N_B and upper energy level N_A is determined by the Boltzmann distribution $N_A/N_B = exp(-g\beta_e B_0/kT)$. The difference between the two populations is generally very small ($N_A/N_B \approx 0.998$). If both populations are equal, no EPR signal is observed. In the absence of relaxation the applied microwaves will equalize these two populations. However, interactions of spins with the molecular environment (called *lattice*) and interactions between spins themselves tend to keep the Boltzmann population at a given temperature [Slichter, 1996]. This process is called spin relaxation. Relaxation limits the measuring time and thus the resolution of EPR experiments, it is also a source of information about the electronic structure and the molecular dynamics. The resonance absorption may be

considered as a continuous competition between the tendency of the microwave field to balance the Boltzmann population difference and the spin relaxation.

Relaxation is characterized by two time constants, T_1 (spin lattice or longitudinal relaxation time) and T_2 (spin–spin or transverse relaxation time), both of which are specific properties of the individual paramagnetic components. In longitudinal electron spin relaxation the magnetic quantum number m_S and the energy of the spin system change. Energy conservation requires that the same energy is absorbed or provided by the environment. Unlike to longitudinal relaxation, transverse relaxation requires an exchange of energy within the spin system. However, interaction with the environment influence to the coherence of the spin system [Schweiger, 2001]. Inversion and saturation recovery ca be used as methods to measure T_1. T_2 is often not well defined in solids and for a practical (quantitative) description of transverse relaxation used phase memory time T_m. It is usually associated with the decay of the primary echo. T_m corresponds to the inverse homogeneous linewidth and is sometimes called T_2.

EPR spectra are also characterized by their linewidth. There are two reasons for broadening of the EPR lines: homogeneous and inhomogeneous. The sources of the homogeneous broadening are fluctuating fields originating from spin motions, when all spins are acting together. The inhomogeneous broadening consists of the superposition of spin packets with different Larmor frequencies. Sources of inhomogeneous broadening are: inhomogeneous of the external magnetic field B_0, anisotropy of tensor interaction in disordered systems and unresolved hyperfine structure (heterogeneous broadening).

2.2 Continuous wave (CW) and time-resolved (TR) EPR technique

Continuous wave (CW) EPR is the easiest EPR technique. The stationary nature of the CW experiment means that spin dynamics are incoherent. Generally, non-saturating conditions are used so that the system is close to thermal equilibrium. The standard way to achieve CW EPR experiments is to keep the transition frequency constant and sweep the applied magnetic field B_0. Magnetic field modulation is used to improve the sensitivity of the EPR signal (signal-to-noise ratio) [Schweiger, 2001]. CW EPR spectra are usually given as the first derivatives of the true absorption spectra. In some special applications, zero field magnetic resonance experiments, the frequency of the applied electromagnetic field is swept to obtain a spectrum [Weil, 2001].

CW EPR spectroscopy relies on magnetic field modulation with frequency ν_{mod} (usually, 100 kHz), hence the fastest possible time response is of the order $2\pi/\nu_{mod}$. The theoretical limit for time resolution in EPR techniques is $1/\nu_{mw}$, which is shorter by orders of magnitude [Weil, 2001]. In order to improve the time resolution, it is needed to avoid modulation techniques completely and instead use methods of direct detection of the transient EPR (TR EPR) signal at a fixed magnetic field employing a suitably fast data acquisition system [Stehlik,1997]. Thus, time-resolved EPR does not use field modulation and has response times as low as tens of nanoseconds, but the sensitivity is low [Schweiger, 2001].

A method of electron paramagnetic resonance spectroscopy with time resolution – time-resolved electron paramagnetic resonance (TR EPR) is a powerful technique that allows the study chemical and biological processes. The main advantage over CW EPR is the ability to detect ESR signals of short-lived states in the photochemical reactions: spin-polarized radical pairs, triplet states, etc [Stehlik, 2006, 1997; Bittl, 2005].

2.3 Pulsed EPR techniques

Pulsed EPR experiments use microwave pulses to prepare the spin system into a non-equilibrium state. Free magnetic induction of the sample is measured, without the application of a microwave field [Schweiger, 2001]. Free induction decay (FID) detection is widely used in NMR, but for most pulsed EPR techniques electron spin echo (ESE) detection is used.

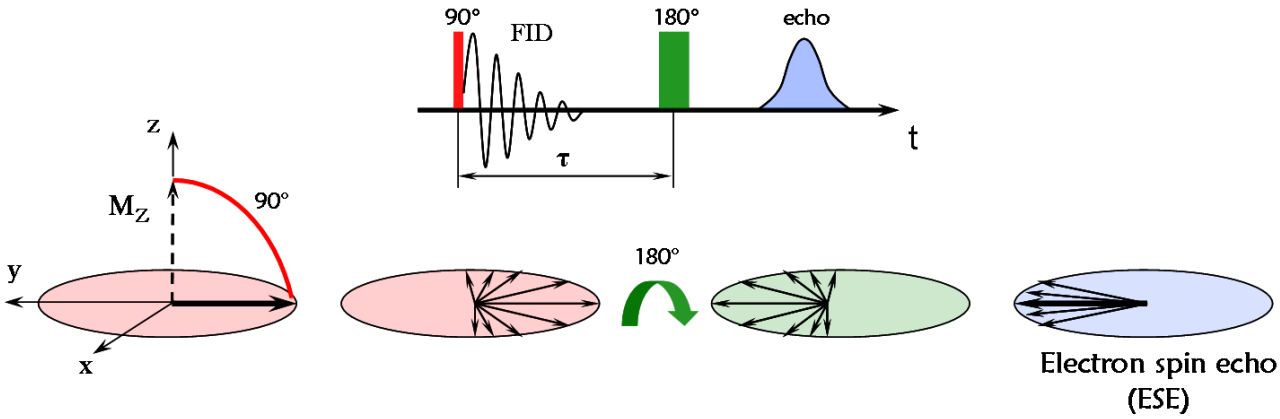

Figure 2.2 Formation of the electron spin echo.

Electron spin echo phenomena: The difference in the populations of the parallel and antiparallel spins leads to a macroscopic magnetization M_Z, to become established in the direction parallel to B_0. The result of applying a short microwave pulse is to rotate the magnetization M_Z through the flip angle $\theta = \gamma_e B_1 t_p$. Here γ_e is the gyromagnetic ratio of the electron spin ($\gamma_e = 1.78 \cdot 10^{11}$ rad·s^{-1}·T^{-1}), B_1 is the field intensity of the microwave pulse, and t_p is the pulse duration. In the simplest type of pulsed EPR experiment a single pulse with a flip angle $\theta = 90^\circ$ (called a 90° or $\pi/2$ pulse) transforms the original longitudinal magnetization M_Z into a transverse *y'* magnetization [Schweiger, 2001] (Fig. 2.2).

The oscillating signal, which decays owing to transverse relaxation or inhomogeneous line broadening, is called the free induction decay (FID). The rapid decay of the FID, caused by inhomogeneous broadening, can be reversed in the spin-echo experiment. This phenomenon, which was first described by Hahn in 1950 for the nuclear spin case, depends on the non-linear behavior of a set of oscillators with different frequencies [Hahn, 1950]. The decreasing of the FID, which is detected after π/2 pulse appears due to the spins with different Larmor frequencies (slower and faster spins) in the EPR spectrum causing the magnetization to fan out in the *x*-*y* plane. After applying a π pulse (180°), the magnetization flips about the *x* axis. The spins still rotate in the same direction and with the same speeds. This has the effect of running the FID backwards in time [Schweiger, 2001]. The faster spins (higher frequencies) after the π/2 pulse will move further than slower spins (lower frequencies). But after the π pulse faster spins overtake the slower spins along the *y* axis and the spin echo signal occurs (Fig. 2.2). The echo formation mechanism can be also described by "race-track" and "pancake" echo models, see details in [Hahn, 1950], [Abragam, 1961].

2.3.1 Electron Spin Echo Envelope Modulation (ESEEM) techniques

The ESE signal amplitude can be described as function of the pulse interval time τ. In 1965, Rowan, Hahn and Mims [Mims, 1965] observed that the decay of the electron spin echo was modulated due to an interaction of the unpaired electron spin with magnetic nuclei. The modulation is caused by periodic dephasing by the nuclei [Schweiger, 2001]. This method gives information on the types of the magnetic nuclei surrounding the centres, their number and the parameters of their magnetic interactions (hyperfine and quadrupole interactions) [Dikanov, 1989].

In two-pulse ESEEM experiments, a ESE sequence ($\pi/2 - \tau - \pi$) is used and the π pulse is incremented out to longer periods of τ. The amplitude of the ESE is measured for each τ, giving rise to a time domain ESEEM spectrum. Since the magnetization is stored transversely during the τ mixing period, these experiments are sensitive to T_2.

In three-pulse ESEEM experiments the following pulse sequence ($\pi/2 - \tau - \pi/2 - T - \pi/2$) is used, τ is held constant and T is incremented, giving rise to a modulation in the three pulse stimulated echo. As with two-pulse ESEEM, the ESE intensity is measured as a function of $\tau + T$, yielding a time domain spectrum that can be converted to a frequency domain spectrum via a Fourier transformation. Since the magnetization is along the z-axis during the mixing period T, three-pulse ESEEM is sensitive to T_1 relaxation. Since T_1 is typically much longer than T_2, three-pulse ESEEM spectra can yield much narrower linewidths than those obtained in two-pulses ESEEM.

The stimulated-echo ESEEM experiment can be used as a two-dimensional technique (2D), i.e., recording the spin echo amplitude as a function of both times τ (time between first and second pulses) and T (time between second and third pulses) to show the correlation of the nuclear spin coherences of the two electron spin manifolds to each other. The limiting factor of 2D three-pulse ESEEM measurements is the time range of τ due to the usually very short T_2 relaxation time of the electron spin system [Schweiger, 2001]. It is highly sensitive to frequencies below 5 MHz and the broadband excitation of nuclear transitions allows correlation experiments. ESEEM techniques are used for measurements of small hyperfine and nuclear quadrupole interactions [Tang, 1994] [Dikanov, 1992] [Thurnauer, 1980] [Deligiannakis, 2001].

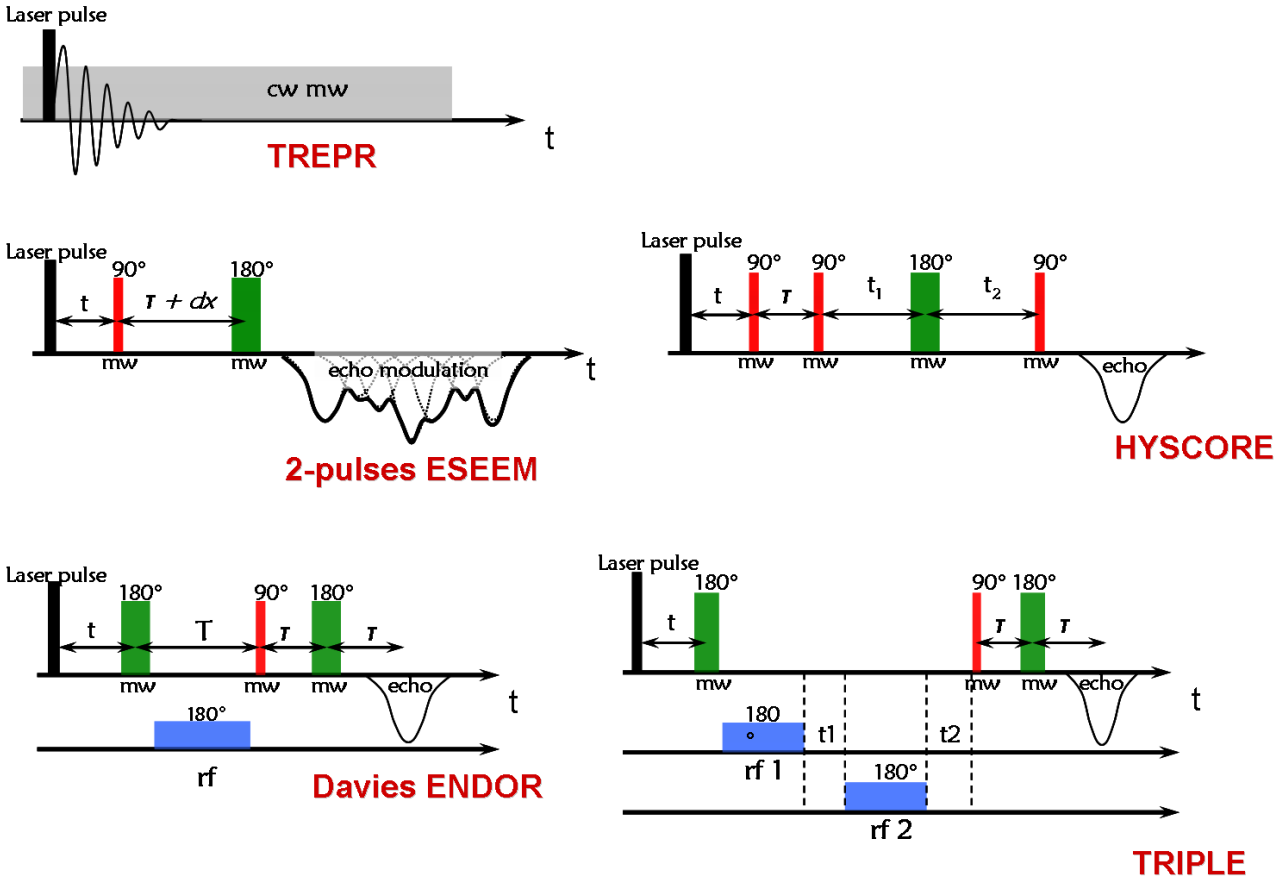

Figure 2.3 Pulse sequences for different pulsed EPR techniques which are used in this work.

2.3.2 HYperfine Sublevel CORrelation Spectroscopy (*HYSCORE)*

The two-dimensional four-pulse stimulated-echo experiment introduced by P. Hofer et al. as hyperfine sublevel correlation spectroscopy (HYSCORE) provides a useful alternative to the 2D three-pulse ESEEM technique [Hoefer, 1986] [Shane, 1992]. The HYSCORE experiment is analogous to three-pulse ESEEM, but contains additional a π pulse which exchanges the populations of the electron spin manifolds (Fig. 2.3). This π pulse, also called the mixing pulse, creates correlations of nuclear spin transitions.

The Fourier transformation of HYSCORE data yields a 2D spectrum with the coordinates of nuclear frequencies from opposite electron spin manifolds [Shane, 1992]. The symmetric nuclear coherence transfer pathways ν_α - ν_β and ν_β - ν_α during the evolution period t_1 - π - t_2 lead to cross peaks (ν_α, ν_β) (ν_β, ν_α) in the 2D spectra, where ν_α and ν_β are the nuclear transition frequencies in the two different m_S states (Fig.2.4). The cross peaks are not the same for all quadrants of the 2D spectrum. For the weak coupling case ($|A| < 2|\nu_I|$), where ν_α and ν_β have the same sign, cross peaks appear in the first (++) quadrant, while in the case of strong hf coupling ($|A| > 2|\nu_I|$), peaks appear in the second (+ –) quadrant (Fig.2.4).

Since the microwave pulse also excites forbidden EPR transitions, unwanted cross peaks appear in the spectrum. The influence of electron transfer on the nuclear coherence and *vice versa* can be suppressed by phase cycling [Schweiger, 2001]. In the case of transfer of two-spin order to nuclear coherence and vice versa axial peaks $(0, \nu_\alpha)$, $(0, \nu_\beta)$ *and* $(\nu_\alpha, 0)$, $(\nu_\beta, 0)$ occur (open circles in Fig. 2.4).

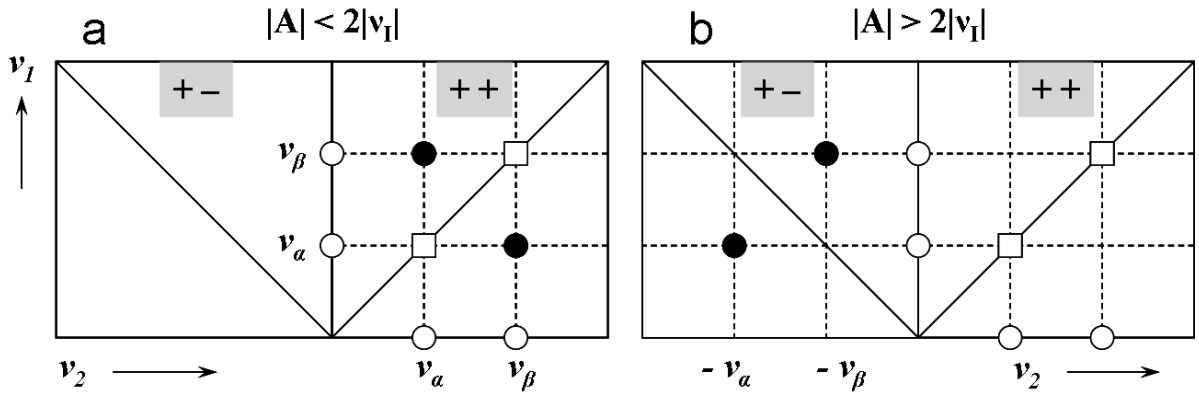

Figure 2.4 Expected peaks in a HYSCORE spectrum in the case of (a) weak coupling and (b) strong coupling. Full circles represent wanted cross peaks, open circles – axial cross peaks, open squares – diagonal peaks.

The additional cross peaks *(ν_α, ν_α) and (ν_β, ν_β)* occur due to an ineffective π pulse flip angle for all spin packets (open squares in Fig. 2.4). The peak positions also depend on the type of coupling in the spin system. For example, for weak coupling region, where ν_α and ν_β have the same sign, peaks are expected in the first (and third) quadrant, for strong coupling region, in the second and fourth quadrant (Fig. 2.4).

The HYSCORE experiment gives improved resolution since during time intervals t_1 and t_2 the electron spin system depends only on longitudinal relaxation [Schweiger, 2001]. In this work, HYSCORE was used for the measurement of weak spin interactions of ^{14}N nuclei

2.3.3 Electron Nuclear Double Resonance (ENDOR) techniques

Electron Nuclear Double Resonance (ENDOR) is a double resonance technique that combines the high resolution and nuclear selectivity of a nuclear magnetic resonance (NMR) experiment with the sensitivity of an EPR experiment. George Feher first described the ENDOR technique in 1956 [Feher, 1956].

In the ESR experiment, transitions are induced between different sublevels. These transitions (Fig.3.1) depend on the selection rules: $\Delta m_S = \pm 1$, $\Delta m_I = 0$. The two transition energies are given by: $\Delta E_{EPR} = h\nu = g_e(\varphi)\mu_B B_0 \pm \frac{A(\varphi)}{2}$, where the φ denotes the angular dependence of the symmetry of the system and its orientation within an arbitrary laboratory reference frame [Schweiger, 2001]. Transitions between levels 1 and 2 and levels 3 and 4 obey the selection rules $\Delta m_S = 0$ and $\Delta m_I = \pm 1$ and are formally forbidden in ESR, but they are the basis of both NMR and ENDOR experiments. The energies of the ENDOR transitions are given by:

$$\Delta E_{ENDOR} = h\nu = \left| \frac{A}{2} \pm g_N(\varphi)\mu_N B_0 \right|.$$

In classical CW ENDOR, a selected EPR transition is excited by the microwave (*mw)* field and the radiofrequency (*rf)* field induces nuclear transitions, which are detected by observing the desaturation of the EPR transition as a function of the radio frequency (Fig.2.5) [Schweiger, 2001]. Unfortunately, CW ENDOR is often restricted to narrow temperature ranges due to relaxation effects. By using short *mw* and *rf* pulses for excitation such unwanted relaxation features can be excluded. This technique is only available in frozen state, because spin echo has fast decay in solution.

In *Davies ENDOR* (Fig.2.3), the first selective *mw* pulse excites one of the EPR transitions [Davies, 1974]. Then, a selective *rf* pulse is applied. If the *rf* pulse is resonance with one of the nuclear transitions, the polarization of this transition is inverted, which also changes the polarization of the electron spin echo of the excited EPR transition. This can then be detected via

the primary echo, *π/2 - τ – π – τ - echo*. The ENDOR spectrum is the result of monitoring the primary echo intensity as the *rf* is incremented stepwise over the desired frequency range.

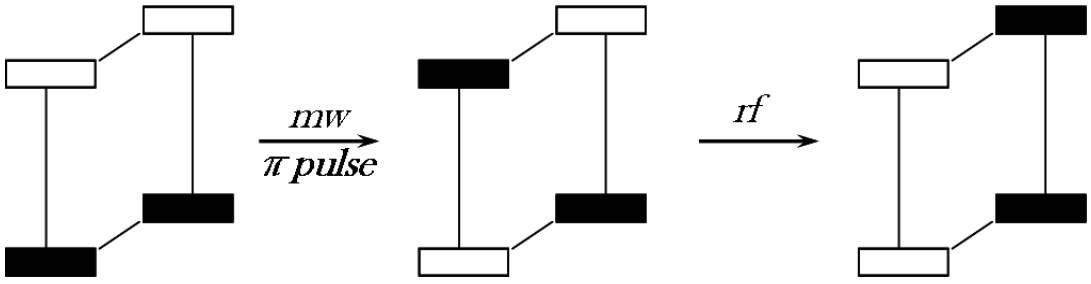

Figure 2.5 Energy levels diagram and possible transitions during ENDOR experiment.

Mims ENDOR (sequence not shown) uses three nonselective π/2 pulses [Mims, 1965]. The preparation part, π/2 – τ - π/2, creates a τ-dependent grated polarization pattern. Then, the *rf* pulse scans nuclear transition. The electron polarization is detected via a stimulated echo created at time *t* after the last π/2 *mw* pulse and recorded as function of the radio frequency. For large hyperfine couplings, it is usually preferable to employ the Davies ENDOR sequence with a well chosen length for the inversion π *mw* pulse. In contrast, Mims ENDOR can be particularly sensitive for measuring small hyperfine couplings [Schweiger, 2001].

2.3.4 Electron Nuclear Nuclear Triple Resonance

The ENDOR technique has been extended to include a second NMR exciting field (pulse), to yield the so-called Electron Nuclear Nuclear Resonance (TRIPLE) experiment [Dinse, 1974] [Kurreck, 1984], [Mobius, 1982]. The TRIPLE method was proposed by Freed in 1969 [Freed, 1969]. In contrast to the ENDOR technique, in which one of the two possible nuclear transitions belonging to a set of equivalent nuclei is excited to desaturate the electron transition, in TRIPLE

experiment two nuclear transitions are excited simultaneously. There are two types of TRIPLE experiment: special TRIPLE and general TRIPLE.

Special TRIPLE: The special TRIPLE technique is used for hyperfine coupling $|A|/2 < \nu_N$ mostly in CW experiments [Kurreck, 1984]. If two *rf* fields are tuned to simultaneously saturate both NMR transitions of the same nucleus, the efficiency of the alternative relaxation path is enhanced. If *rf* fields are strong enough, the nuclear transitions are saturated completely and EPR desaturation becomes independent of nuclear relaxation T_{1N}. Thus line intensities are not determined by the relaxation of various nuclei. The special TRPLE spectrum can reflect the number of nuclei involved in the transition [Schweiger, 2001]. The advantage of special TRIPLE is enhanced sensitivity/resolution.

General TRIPLE: In general TRIPLE resonance NMR transitions of different sets of different kinds of nuclei are saturated simultaneously [Kurreck, 1984]. The general TRIPLE experiment is realized by using the following sequence: one EPR and one NMR transition is saturated; the first *rf1* field (pulse) saturates the NMR transition and the second *rf2* field (pulse) is scanned over the whole range of ENDOR (NMR) resonances. The characteristic intensity changes compared with the ENDOR spectrum then gives the relative signs of the hyperfine couplings [Schweiger, 2001].

In the pulse version of TRIPLE resonance, the mixing period consists of two *rf* π pulses separated in time by t1 (Fig.2.3). The first *rf* pulse (pump pulse) with a fixed frequency ν_{rf1} is resonant with a particular nuclear transition, while the second *rf* pulse (scan pulse) with frequency ν_{rf} is swept through the ENDOR spectrum. The polarization inversion of a nuclear transition, caused by ν_{rf1} in one of the two m_S manifolds, changes the polarization of all nuclear transitions which have a level common with the EPR transition excited by the *mw* preparation pulse.

Changes in line intensity obtained in the two experiments (ENDOR and TRIPLE) are best shown by subtracting the TRIPLE resonance spectrum from the ENDOR spectrum. The resulting difference TRIPLE spectrum (see *e.g.* Fig.5.7) only consists of transitions which have an energy level in common with EPR transition and the nuclear transition excited by ν_{rf1}. Thus, all transitions observed in a difference TRIPLE spectrum belong to the same m_S manifold of the same paramagnetic species. This can be used to determine the relative sign of hfc constants (details in Chapter 5).

Bibliography to Chapter 2

Abragam A. (1961) The Principles of Nuclear Magnetism. Publisher: Oxford University Press, Oxford.

Bittl R. and Weber S. (2005) Transient Radical Pairs Studied by Time-resolved EPR. Biochimica et Biophysica Acta, 1707, 117– 126.

Davies E.R. (1974) A New Pulse ENDOR Techniques. Phys.Letters, 47A, 1-2.

Deligiannakis Y., Rutherford A.W. (2001) Electron Spin Echo Envelope Modulation Spectroscopy in Photosystem I. Biochimica et Biophysica Acta, 1507, 226-246

Dikanov S.A, Astashkin A.V. (1989) ESEEM of Disordered Systems: Theory and Applications. In Hoff A.J. (ed) Advanced EPR. Applications in Biology and Biochemistry. Publisher: Elsevier, Amsterdam, 59-115.

Dikanov S.A., Tsvetkov Yu. (1992) Electron Spin Echo Envelope Modulation ESEEM Spectroscopy. Publisher: CRC-Press.

Dinse K.P., Biehl R., Möbius K. (1974) Electron Nuclear Triple Resonance of Free Radicals in Solution. J. Chem. Physics, 61, 4335-4341.

Feher G. (1956) Observation of Nuclear Magnetic Resonances via the Electron Spin Resonance Line. Physical Review, 103, 834-835.

Freed J.H. (1969) Theory of Saturation and Double Resonance Effects in ESR Spectra. IV. Electron–Nuclear Triple Resonance. J. Chem. Physics, 50, 2271-2272.

Hahn E. L. (1950) Spin Echoes. Physical Review, 80, 580–594.

Höfer P., Grupp A., Nebenfur H. and. Mehring D.M. (1986) Hyperfine Sublevel Correlation Spectroscopy. Chem. Phys. Letters 132, 279-282.

Kurreck H., Kirste B., and Lubitz W. (1984) ENDOR Spectroscopy - A Promising Technique for Investigating the Structure of Organic Radicals. Angew. Chemie, 23, 173-252.

Landau L. D., Lifshitz E. M. (1981) Quantum Mechanics: Non-Relativistic Theory, vol. 3, Third Edition. Publisher: Butterworth-Heinemann

Mims W.B. (1965) Pulsed ENDOR experiments. Proceedings of the Royal Society of London, 283, 452-457.

Möbius K. (2003) Multifrequency EPR and ENDOR on Transient Radicals and Radical Pairs in Liquid Crystals and Proteins: Structure and Dynamics of Cofactors in Natural and Artificial Photosynthesis. Molecular Crystals and Liquid Crystals, 394, 1–17.

Möbius K., Plato M., Lubitz W. (1982) ENDOR and TRIPLE Resonance Spectroscopy. Physics Reports, 87, 171-208.

Möbius, K., Savitsky A. (2009) High-field EPR Spectroscopy on Proteins and Their Model Systems. Publishers: Royal Society of Chemistry, Cambridge.

Rowan L.G., Hahn E.L., Mims W.B. (1965) Electron Spin Echo Envelope Modulation. Physical Review, 137, 61-71.

Schweiger A. and Jeschke G. (2001) Principles of Pulse Electron Paramagnetic Resonance. Publishers: Oxford University Press, UK.

Shane J.J., Höfer P., ReijerseE.J., de Boer E. (1992) Hyperfine Sublevel Correlation Spectroscopy (HYSCORE) of Disordered Solids. J. Magn. Resonance, 99. 596-604.

Slichter C.P. (1996) Principles of Magnetic Resonance. Third edition. Publishers: Springer, Berlin-New York.

Stehlik D., (2006) Transient EPR Spectroscopy as Applied to Light-Induced Functional Intermediates Along the Electron Transfer Pathway in Photosystem I. In: Golbeck J.H.

(ed) Photosystem I: The Light-Driven Plastocyanin: Ferredoxin Oxidoreductase. Advances in Photosynthesis and Respiration, vol 24. Publisher: Springer, Dordrecht, 361–386.

Stehlik D., Möbius K., (1997) New EPR Methods for Investigating Photoprocesses with Paramagnetic Intermediates. Annual Reviews of Physical Chemistry, 48, 745–784.

Tang J., Thurnauer M.C., Norris J.R. (1994) Electron Spin Echo Envelope Modulation due to Exchange Dipolar Interactions in a Spin-correlated Radical Pair. Chem. Phys. Letters, 219, 283-290.

Thurnauer M.C. and Norris J.R. (1980) An Electron Spin Echo Phase Shift Observed in Photosynthetic Algae. Chem. Phys. Letters, 76,557-561.

Weil J. A.; Bolton J. R., Wertz J. E. (2001) Electron Paramagnetic Resonance: Elementary Theory and Practical Applications. Publishers: Wiley-Interscience, New York.

Zavoisky E.K. (1944). The Paramagnetic Absorption of a Solution in Parallel Fields. Journal of Physics-USSR, 8, 377-380.

Chapter 3. Spin Hamiltonian of the two-spin system

A series of spin-correlated radical pair (RP) and triplet states are created during the light-induced processes in photosynthetic reaction centers. These paramagnetic states can be detected by EPR methods. The theory of RP can help to understand the information that is obtained from EPR spectra.

3.1 The Spin Hamiltonian of the radical pair

An electron has a spin *S*, equal to ½. It has two possible values of the projection on the axis of quantization, which is called as z axis. The wave functions of spin, corresponding to the projection of the spin m_S = ½ and m_S = - ½, are denoted by the symbols α and β, respectively. For system that contains two S = ½ spins, it is converted to use the total spin operator $\hat{S} = \hat{S}_1 + \hat{S}_2$. Eigenvalues of the operator $\hat{S}^2$ are the singlet and triplet states, respectively:

$$|S\rangle = \frac{1}{\sqrt{2}}(\alpha_1\beta_2 - \beta_1\alpha_2) \qquad S = 0,$$

$$|T_{+1}\rangle = \alpha_1\alpha_2 \qquad S = 1, S_z = +1,$$

$$|T_0\rangle = \frac{1}{\sqrt{2}}(\alpha_1\beta_2 + \beta_1\alpha_2) \qquad S = 1, S_z = 0,$$

$$|T_{=1}\rangle = \beta_1\beta_2 \qquad S = 1, S_z = -1.$$

The wave function of two spins in the triplet states with total spin projection +1 and -1 is the product of the wave functions of partners in the pair. The wave function in the singlet state of

S and the triplet state of T_0 (zero spin projection) can not be represented as the product of functions of two spins. This reflects the existence of correlations in the state of two spins.

The primary spin state of radical pair (RP) is singlet. The initial state of RP is not an eigenvalue condition of the energy operator of RP, wave function varies with time.

In general, changes in the spin system during time are given by the Schrödinger equation:

$$i\hbar \frac{\partial \psi}{\partial t} = \hat{H}\psi$$

where $\hat{H}$ is spin-hamiltonian of the system, ψ is the wave function.

The Spin Hamiltonian of the two-spin system in general terms can be represented as [Schweiger, 2001]:

$$\hat{H}_0 = \sum_i \left[\hat{H}_{EZ}(i) + \hat{H}_{ZFS}(i)\right] + \sum_j \left[\hat{H}_{NZ}(j) + \hat{H}_{NQ}\right] + \sum_{i,j} \hat{H}_{HFI}(i,j) + \sum_{i \geq k} \hat{H}_{SS}(i,k)$$

where $\hat{H}_{EZ}$ the operator of spin interaction of electron spin *i* and an external magnetic field B_0 (electron Zeeman interaction), $\hat{H}_{ZFS}$ the zero-field splitting, $\hat{H}_{NZ}$ the operator of nuclear Zeeman interaction of nuclear spin j, $\hat{H}_{NQ}$ the operator of the nuclear quadrupolar interaction (for $I > ½$), $\hat{H}_{HFI}$ the operator of the hyperfine interaction of electron spin *i* with the nuclear spins *j*, $\hat{H}_{SS}$ - the operator of the spin-spin interaction between electron spins *i* and *k* (Fig.3.1). Typical energies for each term are: electron Zeeman (~ 10 GHz) > nuclear Zeeman (1 – 15 MHz) ≈ electron-nuclear hyperfine (0-10 MHz) [Que, 2000].

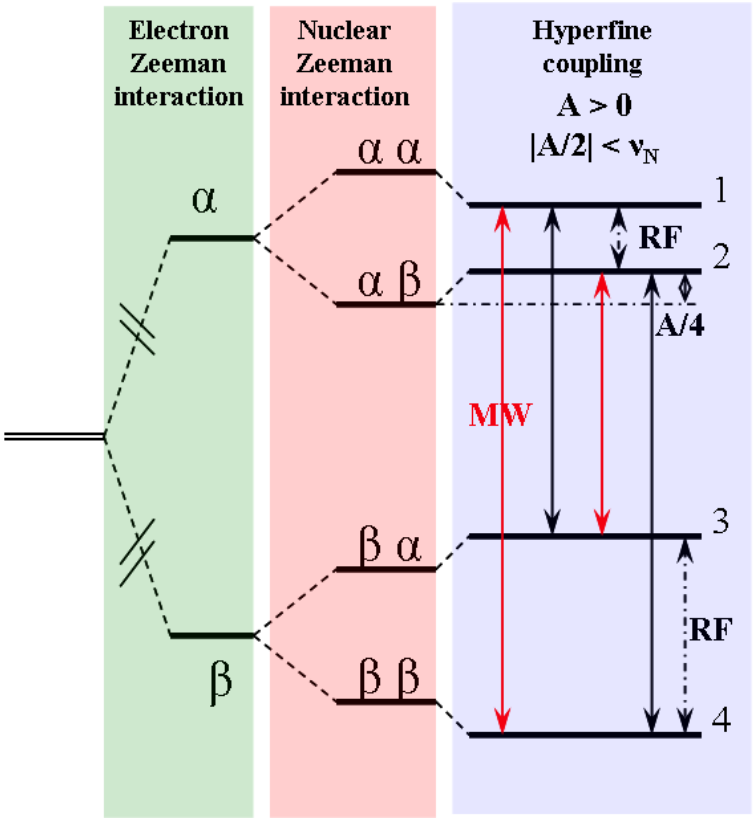

Figure 3.1 Energy level diagram for an electron spin S = ½ coupled to a nuclear spin I = ½ in an external magnetic field in the case of weak positive hf coupling ($|A/2| < |\nu_N|$). The vertical arrows indicate forbidden EPR transitions (red arrows), allowed EPR transitions (black arrows) and ENDOR of RF transitions (dashed arrows).

3.2 Electron Zeeman Interaction

The effect of the applied external magnetic field B_0 is to lift the splitting of the two electron/nuclear states, and is called the Zeeman effect [Zeeman, 1897]. The general term describing the interaction between an electron spin $\hat{S}$ and the external magnetic field B_0 is the electron Zeeman interaction [Schweiger, 2001]:

$$\hat{H}_{EZ} = \beta_e B_0^T \mathbf{g} \hat{S} / \hbar = \frac{\beta_e}{\hbar} \begin{pmatrix} B_X & B_Y & B_Z \end{pmatrix} \begin{pmatrix} g_{XX} & g_{XY} & g_{XZ} \\ g_{YX} & g_{YY} & g_{YZ} \\ g_{ZX} & g_{ZY} & g_{ZZ} \end{pmatrix} \begin{pmatrix} S_X \\ S_Y \\ S_Z \end{pmatrix} = \frac{\beta_e}{\hbar} \sum_{i,j=X,Y,Z} g_{ij} B_i S_j$$

where β_e is Bohr's magneton equals 9.27410^{-24} $J \cdot T^{-1}$, $\hbar$ - reduced Planck constant equals $1.055 \cdot 10^{-34}$ J·s and $\boldsymbol{g}$ is tensor, which characterizes the magnetic moment and gyromagnetic ratio. The $\boldsymbol{g}$ tensor components are affected by spin-orbit coupling and reflect features of the electronic structure of the system an the symmetry of molecule [Que, 2000].

If the molecule has both spin and orbital moments, then the $\boldsymbol{g}$ tensor will be anisotropic [Atherton, 1993]. The $\boldsymbol{g}$-tensor is a symmetric tensor with six independent values: g_{XX} (g_X), g_{YY} (g_Y) and g_{ZZ} (g_Z) are the three principal values and three Euler angles describing the orientation of the principal axes of the tensor in the molecular frame.

The determination of the principal components of the $\boldsymbol{g}$ tensor is possible only for systems in the solid state. For paramagnetic species in solution, because of rapid and random tumbling, all orientations are averaged and one observes the trace of the $\boldsymbol{g}$ tensor – the g-factor (or isotropic g-factor) equals $g = 1/3(g_X + g_Y + g_Z)$.

Depending on the relation between the $\boldsymbol{g}$ tensor components g_X, g_Y and g_Z, three types of EPR spectra appear: i) isotropic single symmetric EPR spectrum - $g_X = g_Y = g_Z$; ii) axial EPR spectrum - $g_X = g_Y <$ (or >) g_Z, where $g_X = g_Y$ is perpendicular $g_\perp$ and g_Z is parallel $g_\parallel$; iii) rhombic EPR spectrum - $g_X \neq g_Y \neq g_Z$ [Que, 2000].

The g-factor of a free electron represents the value of the magnetic moment associated with the angular momentum of the spinning electron relative to the magnetic moment associated with the unit of orbital angular momentum. The g-factor is a proportionality constant approximately equal to 2 for most samples, but which varies depending on the electronic configuration of the radical or ion.

3.3 Zero-Field Splitting

The zero-field splitting (ZFS) removes the degeneracy of the spin microstate for spin systems with $S > ½$ and non-cubic symmetry in the absence of an applied field [Schweiger, 2001]. This term is described by:

$$\hat{H}_{ZFS} = \hat{S}\mathbf{D}\hat{S}$$

where $\boldsymbol{D}$ is ZFS tensor. The $\boldsymbol{D}$ tensor is traceless (sum of diagonal elements is zero) and symmetric ($D_{i,j} = D_{j,i}$). In its eigenframe, the $\boldsymbol{D}$ tensor is diagonal, and the zero-field operator term is:

$$\hat{H}_{ZFS} = D_X S_X^2 + D_Y S_Y^2 + D_Z S_Z^2 = D\left(S_Z^2 - S(S+1)/3\right) + E\left(S_X^2 + S_Y^2\right)$$

$$D = \frac{3}{2} D_Z \,,\; E = \frac{D_X - D_Y}{2}$$

where D is the axial and E is the rhombic ZFS parameter. The parameters D and E describe the separation of the energy levels (three, in the case of S = 1) in the absence of the external magnetic field B_0. D gives a measure of the average distance between the two unpaired electrons. As D increases, the electrons in a triplet are on the average closer together. E gives a measure of the deviation of a molecule from axial symmetry. Thus, the relative magnitudes of D and E provide a means to study molecular structural properties. For a system with cubic symmetry $D = E = 0$; for axial symmetry, $D \neq 0,\ E = 0$; and for symmetries lower than axial, $D \neq 0,\ E \neq 0$ [Carrington, 1967]. E takes unique values over the range 0 to $D/3$.

3.4 Nuclear Zeeman interaction

The coupling of a nuclear spin I to the external magnetic field B_0 is described by the nuclear Zeeman interaction [Schweiger, 2001]:

$$\hat{H}_{NZ} = -\beta_N g_N B_0^T \hat{I} / \hbar = -\frac{\beta_N}{\hbar} g_N \sum_{i=X,Y,Z} B_i I_i ,$$

where β_N is the nuclear magneton (equals $5.050 \cdot 10^{-27}$ J·T^{-1}) and g_N is the nuclear *g*-factor. The g_N values are assumed to be isotropic.

For protons the nuclear Zeeman interaction is only 658 times smaller than the electron Zeeman interaction. For all other nuclei g_N is even smaller. Thus, the nuclear Zeeman effect usually has minor contribution to the EPR spectrum.

3.5 Hyperfine interaction

The unpaired electron is very sensitive to its local surroundings. The nuclei of atoms in a molecule or complex often have a magnetic moment, which produces a local magnetic field at the electron. The interaction between the electron and the nuclei is called the hyperfine interaction. The hyperfine interaction between electron and nuclear spins is described by the term [Schweiger, 2001]:

$$\hat{H}_{HFI} = \hat{S}^T \mathbf{A} \hat{I} = \begin{pmatrix} S_X & S_Y & S_Z \end{pmatrix} \begin{pmatrix} A_{XX} & A_{XY} & A_{XZ} \\ A_{YX} & A_{YY} & A_{YZ} \\ A_{ZX} & A_{ZY} & A_{ZZ} \end{pmatrix} \begin{pmatrix} I_X \\ I_Y \\ I_Z \end{pmatrix}$$

The matrix ***A*** is usually symmetric and can be transformed to its diagonal form. The hyperfine interaction has two general origins. The first is the so called “contact” or Fermi

interaction. It is the isotropic component of the hyperfine interaction a_{iso} and arises because the unpaired electron has a finite probability of being in the same space as the nucleus [Weil, 2000].

The isotropic hyperfine coupling constant is $a_{iso} = \frac{2\mu_B}{3\hbar} g_e \beta_e g_N \beta_N |\psi(0)|^2$, where $|\psi(0)|^2$ is the electron spin density at the nucleus. The isotropic part of the hyperfine interaction comes from overlap of the *s* orbital with the nucleus [Schweiger, 2001]. Physically, the sign of *A* indicates parallel or antiparallel orientation of electron and nuclear spins [Atherton, 1993]. Because the hyperfine interaction is a property of the spin system, *A* is not dependent on the direction or magnitude of the external magnetic field.

The anisotropic component of the hyperfine interaction (the dipolar coupling) $T = T_{ij} = \frac{\mu_B}{4\pi\hbar} g_e \beta_e g_N \beta_N \left\langle \psi_0 \left| \frac{3 r_i r_j - \delta_{ij} r^2}{r^5} \right| \psi_0 \right\rangle$ is due to dipole-dipole interaction between electron and nuclear spins, where *r* is the distance between the electron and the nuclear spins [Schweiger, 2001]. It is traceless and symmetric in the case of electron-nuclear dipole-dipole coupling. The anisotropic (dipolar) part is important in multi-spin systems and for unpaired electrons in non-symmetric orbitals (*p,d*).

Usually, several magnetic nuclei exist in the system, which may be grouped into magnetically equivalent sets due to the symmetry of the molecule. Equivalent nuclei, each with spin I_i, interact as one nucleus with total spin $I = \sum_i I_i$.

3.6 Electron spin-spin interaction

Strongly coupled unpaired electrons are usually characterized by a spin $S > ½$ (zero-field interaction). Two weakly coupled spins are characterized by the exchange coupling ***J*** and the dipole-dipole coupling ***D*** between the individual spins S_1 and S_2 [Schweiger, 2001].

The term describing the exchange interaction between two electrons is:

$$\hat{H}_{SS} = \hat{S}_1^T \mathbf{J} \hat{S}_2$$

The exchange interaction results when the orbitals of the two spins overlap significantly. A positive coupling ($J > 0$) results for the case when the triplet state stabilizes via the singlet state (ferromagnetic coupling, Coulomb interaction). A negative exchange coupling ($J < 0$) corresponds to the case when the triplet state of the two electrons is higher by energy than the singlet (antiferromagnetic coupling, overlapping of orbitals) [Schweiger, 2001]. The dipole-dipole coupling between two electron spins is analogous to the dipole-dipole coupling between electron and nuclear spins (anisotropic part of the hyperfine interaction and the zero-field interaction).

3.7 Nuclear Quadrupole interaction

A nucleus with $I \geq 1$ can have a non-spherical charge distribution. This gives rise to a quadrupole moment. The nuclear quadrupole moment (i.e., ^{2}H, ^{14}N, ^{16}O) interaction with the surrounding electric field gradient (*eq)*, can be expressed as [Schweiger, 2001]:

$$\hat{H}_{NQ} = \hat{I}\mathbf{P}\hat{I} = P_X I_X^2 + P_Y I_Y^2 + P_Z I_Z^2 = \frac{e^2 qQ}{4I(2I-1)h}\left[\left(3I_Z^2 - I(I+1)^2\right) + \eta\left(I_X^2 - I_Y^2\right)\right]$$

where tensor **P** is called the nuclear electric quadrupole coupling tensor, e is the electronic charge, Q is the electric quadrupole moment of the nucleus and $\eta = (P_X - P_Y)/P_Z$ is the asymmetry

parameter with $0 \leq \eta \leq 1$. A value of $\eta = 0$ corresponds to complete axial symmetry and $\eta = 1$ to pure rhombic symmetry [Schweiger, 2001]. In the presence of axial symmetry, the axial component of the **P** tensor, e.g. P_Z is defined by $P_Z = K = e^2qQ/[2Ih(2I-1)]$ [Schweiger, 2001]. It is quite common that only two quantities are given for analysis of quadrupole coupling: $4K = e^2qQ/h$ and η.

Bibliography to Chapter 3

Atherton N. M. (1993) Principles of Electron Spin Resonance. Publishers: Ellis Horwood, Chichester.

Carrington, A. McLachlan A. (1967). Introduction to Magnetic Resonance. Publishers: Harper and Row, London.

Que L.Jr. (2000) Physical Methods in Bioinorganic Chemistry: Spectroscopy and Magnetism. Publishers: University Science Books.

Schweiger A. and Jeschke G. (2001) Principles of Pulse Electron Paramagnetic Resonance. Publishers: Oxford University Press, UK.

Weil J.A.; Bolton J.R., Wertz J.E. (2001). Electron Paramagnetic Resonance: Elementary Theory and Practical Applications. Publishers: Wiley-Interscience, New York.

Zeeman P. (1897). The Effect of Magnetisation on the Nature of Light Emitted by a Substance. Nature, 55, 347.

Chapter 4. Materials and Methods

4.1 Materials: Chlorophyll a anion radical in solution

4.1.1 Chlorophyll a extraction and purification

Chlorophylls extraction from fresh spinach with dioxane: The chlorophyll extraction procedure described by Iriyama [Iriyama, 1974] was used. This method uses dioxane in the first step for selective precipitation of chlorophyll from crude extracts with acetone. All the solvents used were reagent grade and were purified further by standard methods to remove traces of unwanted contaminants. Fresh commercially available spinach leaves were used. All procedures in this study were carried out at about +4 °C under dim green light.

Spinach leaves (100 g fresh leaves) were washed in cold water and shredded in a blender in 500 ml of cold methanol. The green juice obtained was filtered through a cotton pad to remove the waste. The filtrate was then centrifuged at 1000*g for 5 min to remove any remaining insoluble material. The obtained deep green supernatant solution was mixed with freshly distilled dioxane one-seventh volume of the total solution. Then 80 ml milli-Q water was added drop-wise, with stirring, until high turbidity developed. The mixture was placed in an ice box for one hour to allow sedimentation. The lower thick mass of dark green sediment was collected by centrifugation at 10000*g for 5 min. The crude mass of chlorophyll thus obtained was dissolved in approx. 150 ml of methanol:dioxane mixture (7 : 1, v/v) and precipitated again by drop-wise addition of approx. 25 ml of milli-Q water, with stirring. The last procedure was repeated at least two times and the final product was filtrated through a paper filter. The Chl concentration was

measured using the method of Porra (see below). The Chl sample was dried and kept at -30 °C refrigerator until the next step of purification.

Chlorophyll extraction from dry spinach leaves: The chlorophyll extraction procedure described by Schertz [Jubert, 2007] was used with some modifications. Fresh commercially available spinach leaves were used. All the experiments in this study were carried out at about -4 °C under dim green light.

Spinach leaves were dried for 2 - 3 days at temperature of 30 - 40 °C. As soon as the leaves were dry enough to crumble easily in the hands, they were milled and kept in a refrigerator at -30 °C. The dry leaves were washed twice in a blender with 500 ml of light petroleum to remove carotenoids and waxes and then extracted twice using 400 ml of methanol/light petroleum (3:1, v/v). The combined extracts were transferred to a separatory funnel and washed with 250 ml of saturated sodium chloride water solution, pulling the methanol into the aqueous phase and leaving the light petroleum containing the dark chlorophyll pigment. The aqueous layer was extracted with 200 ml of light petroleum. The light petroleum layers were combined and washed with 100 mL of saturated sodium chloride. The extract was then filtered using a clean fritted funnel a final time and dried. This residue was dissolved with 50 ml of acetone and left overnight at

-20 °C. The acetone fraction was filtered using a clean fritted funnel and evaporated. The dried sample kept in a -30 °C fridge till the next step of purification.

Determination of chlorophyll concentration: UV/VIS spectra were recorded with a spectrometer UV2-300 (Unicam). The reference used was 80 % (v/v) acetone. The chlorophyll concentration in the sample was determined via the following steps: A small amount of Chl or PS I sample was mixed with 80 % (v/v) acetone, and the absorption spectrum was recorded. The chlorophyll concentration was calculated using the absorption coefficients determined by Porra [Porra, 1989].

$$A = \varepsilon \cdot c \cdot l \Rightarrow c = \frac{A}{\varepsilon \cdot l}$$

where A is the absorption intensity at certain wavelength, ε is the extinction coefficient, c is the concentration and l is the path length. Procedures for determination of the concentration of Chl *a* and extinction coefficient for Chl *a* in different solvents is given in [Porra, 1989].

High Performance Liquid Chromatography (HPLC): The solvent-free extracted products from fresh spinach were enriched in chlorophyll *a*, but still contained other pigments, such as chlorophyll *a'*, *b*, carotenoids as well as oils, fats and waxes, which needed to be removed. To improve the purification of chlorophyll, we used high-performance liquid chromatography (HPLC) [for review see Parriott, 1993].

All sample manipulations were done under green light. Samples were prepared as quickly as possible to limit Chl *a* degradation. All solvents were bubbled with argon before used. The preparative HPLC apparatus (Fig.4.1) consisted of a Model Abimed 306 high-pressure pump (Gilson),

a Model SPD-10AV-VP variable wavelength diode array detector (Shimadzu) fixedat 430 nm, and a Model 7125 sample injector equipped with a 2 ml loop. The stainless steel column

(250 mm X 21 mm i.d.) was packed with a 7-µL silica gel (Nucleosil 100-7, C18, Macherey-Nagel). About 2 mL of dichloromethane/methanol (1: 7, v/v) containing 20 to 50 mg of the mixture of Chl *a, a', b* and *b'*, prepared by the above procedure, was injected and eluted isocratically with the same solvent. The Chl *a* fraction was determined by its characteristic absorption spectrum and collected.

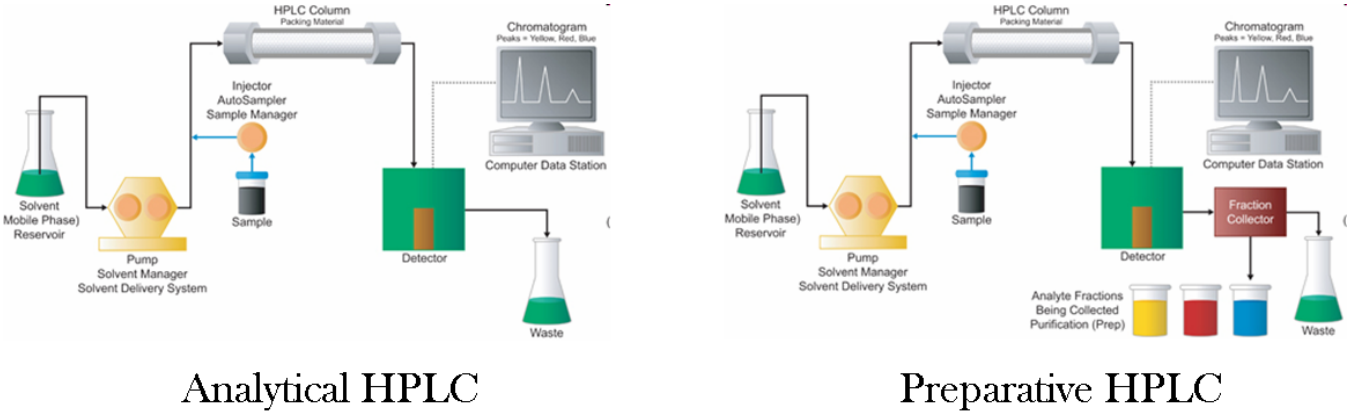

Figure 4.1 Scheme of basic components used for the analytical and preparative HPLC techniques.

Analytical HPLC (Fig.4.1) was used to examine the purity of Chl *a*. The analytical HPLC apparatus consisted of a Model Abimed 306 high-pressure pump (Gilson), a Model SPD-M10AV variable wavelength diode array detector (Shimadzu) set at 430 nm and a Model 7125 sample injector equipped with a 20 µl loop. The stainless steel column (150 mm X 4.6 mm i.d.) was packed with a 3-µm silica gel (Nucleosil 100-3, C18, Macherey-Nagel). Other conditions were the same as in the preparative HPLC mentioned above. Both extraction procedures yielded chlorophyll *a* samples of 96-98 % purity. The chlorophyll solution was dried immediately in a rotary evaporator, and the dried sample stored at -30 °C fridge.

4.1.2 Electrochemical generation of the chlorophyll a anion radical

Purified (98-99 %) and dried Chl *a* was stored in a -30 °C refrigerator. The concentration of Chl *a* was determined with procedure described by Porra [Porra, 1989]. For one electrochemical experiment 1mL of ~ 1 mM Chl *a* were used.

All sample treatments were done under green dim light. Samples were prepared as quickly as possible to limit Chl *a* degradation. All solvents were distilled and, directly before use, deoxygenated using three freeze-pump-thaw cycles.

The electrochemical cell used was designed by Christoph Laurich (Max-Planck Institute for Bioanorganic Chemistry, Mülheim an der Ruhr). The pyrex electrochemical cell was connected to a high-vacuum line and had the option to fill the line with nitrogen gas. The volume of the cell was 1 mL. It contained 4 electrodes (Fig. 4.2). The first working electrode (for coulometry) was Platinum (Pt) net, the second working electrode (for cyclovoltammetry) was Pt wire in a glass tube. The reference electrode was Ag wire in a glass tube with frits. The counter electrode was a Pt wire in a glass tube with frits. A magnetic stirrer was used to mix the solution.

The supporting electrolyte tetrabutylammonium-tetrafluoroborate $TBABF_4$ was purchased from Fluka (electrochemical grade). The concentration of $TBABF_4$ was set to 10 times higher than the concentration of Chl *a*. The pure supporting electrolyte was dissolved with distilled dimethoxyethane (DME). DME was dried over sodium-potassium (Na/K) alloy at the vacuum line.

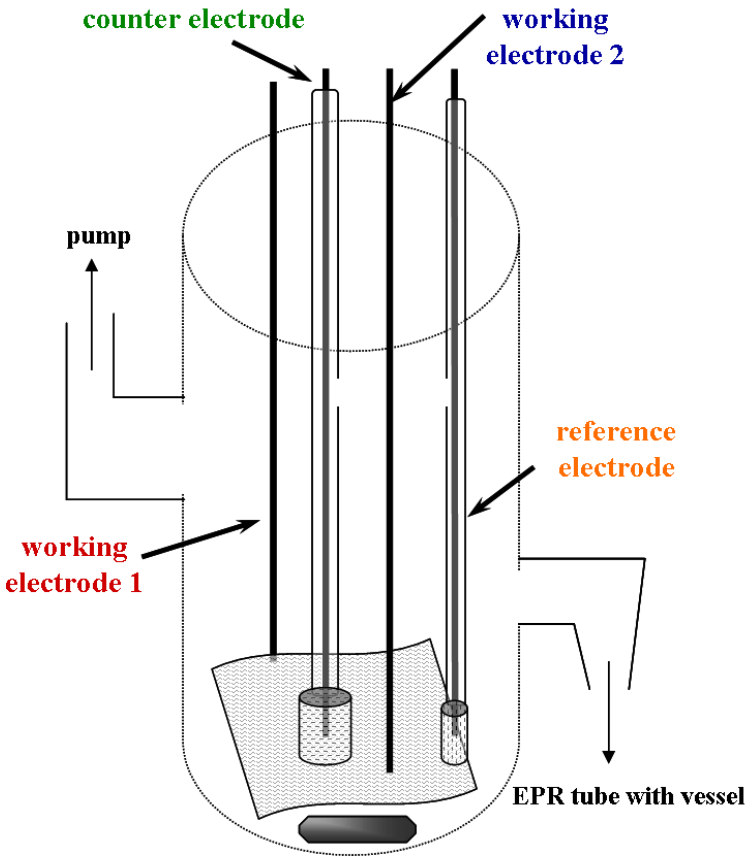

Figure 4.2 Scheme of electrochemical cell used for reduction of chlorophyll *a*.

A potensiostat EG&GM 283 was used. *Cyclovoltammetry* was measured before starting coulometry to check for the redox potential of the sample. In cyclovoltammetry a second working electrode (the Pt wire in a glass tube) was used. For *coulometry* the first working electrode was a Pt-net. Cyclovoltammetry was done using a scanning speed of 100 mV/s.

The reduction was performed using the first working electrode with 80 mC, which under ideal conditions yields ~80 % singly reduced Chl *a*. An EPR quartz tube (2.8 mm outer diameter o.d.) with additional vessel was directly connected to the cell. An additional vessel with solvent was used to change the concentration during the EPR measurements. About 40-100 µL of

the solution was transferred to the EPR tube and frozen in liquid nitrogen. The tube was then pumped and flame sealed.

4.2 Materials: Primary electron acceptor A_0^- in Photosystem I

4.2.1 PS I samples:

i) PS I samples from *Thermosynechococcus elongatus* crystals was provided by Prof. Petra Fromme (Arizona State University);

ii) PS I sample from wild type of *Synechocystis* sp. PCC 6803;

iii) *men B26* mutant of *Synechocystis* sp. PCC 6803, where the native phylloquinone was replaced by deuterated vitamin K_3. The samples were provided by Dr. Mikhail L. Antonkine and Dr. Jens Niklas (Max-Planck Institute for Bioanorganic Chemistry, Mülheim an der Ruhr).

4.2.2 Photoaccumulation experiments: preparation of stationary radicals in PS I

Preparation of A_1^- EPR samples: All steps were done under anaerobic conditions, under argon gas flow in a glass anaerobic box. Buffers were degassed and bubbled with argon. The photoaccumulation procedure for the preparation of stationary radicals in PS I, described previously was used [Heathcote, 1996] [Niklas, 2007]. For one Q-band sample, approx. 20 µL solution of PS I from *Thermosynechococcus elongatus* (~ 12 mM Chl *a*) was mixed with 2.5 µL 1 M glycine buffer pH 10. 2 - 3 µL of fresh sodium dithionite (Fluka) solution in 1 M glycine buffer pH 10 (final concentration 300 mM) was added to the PS I solution. The sample was then

transferred into a Q-band EPR tube (inner diameter 1.7 mm, outer diameter 2.8 mm) and was kept in the dark for 30 minutes at 4 °C (on ice) in order to pre-reduce the iron-sulfur centers. Afterwards, the PS I sample was dark frozen in liquid nitrogen.

Illuminations were performed at 240 K (in ethanol + dry ice mixture) and 274 K (water + ice mixture) using two 150 W halogen lamps from two sides. The illumination time was 10 minutes.

Preparation of A_0^- EPR samples: For preparation of A_0^- PS I samples from *i)* wild type of *Synechocystis* sp. PCC 6803, *ii) Synechocystis* sp. PCC 6803 growing in ^{15}N medium and *iii) men B26* mutant of *Synechocystis* sp. PCC 6803 were used, in which native phylloquinone were replaced by deuterated vitamin K_3. The same photoaccumulation procedure was used [Heathcote, 1996]. The Illumination was carried out at 205 K (ethanol + dry ice mixture) using two 150 W halogen lamps from two sides. The illumination time was 20 minutes.

4.3 Materials: Heliobacterial reaction centers from Heliobacterium modesticaldum (HbRC)

4.3.1 Isolation and purification of HbRC

Samples of *Heliobacterium modesticaldum* samples were provided by Mark Heinnickel and John H. Golbeck (The Pennsylvania State University). The whole cells were lysed by sonication and their membranes were pelleted by centrifugation at 200,000**g*. Solubilized membranes were passed over a diethylaminoethyl (DEAE) cellulose ion-exchange column, equilibrated in 50 mM MOPS, pH 7.0 [Heinnickel, 2007]. During purification using a DEAE-Cellulose (Diethylaminoethyl) chromatographic column, heliobacterial reaction centers

(HbRC) lose the top subunit PshB, together with the iron-sulfur clusters F_A and F_B [Heinnickel, 2005]. Thus, samples were taken from all the included purification steps: whole cells, membranes, cells lysate and purified HbRC after DEAE column.

All manipulations with HbRC (with exception of the experiment by conversion of BChl *g*) were conducted inside an anaerobic glove box (Coy, Topffer Lab System). All buffers and solutions were deoxygenated by bubbling with argon and kept inside the anaerobic glove box until use.

4.3.2 Oxygen sensitivity of HbRC (conversion of BChl g to Chl a)

Conversion of BChl *g* to Chl *a* in HbRC was done by incubation in the dark under aerobic conditions with potassium ferricyanide $K_3[Fe(CN)_6]$ (final concentration 20 mM). Complete conversion of BChl *g* to Chl *a* in HbRC occurred over a period of 4-5 hours. Conversion can also be achieved by prolonged aerobic incubation without the presence of potassium ferricyanide (approximately 120 hours). Excess of potassium ferricyanide was removed by purification over NAP-10 or PD-10 chromatographic columns containing G-25 medium (GE Healthcare). The conversion of BChl *g* to Chl *a* was monitored by UV/Vis absorption spectroscopy.

EPR samples were frozen in the dark in the presence of 5 mM sodium ascorbate as an external electron donor.

4.3.3 Quinone replacement

Quinones with different number of rings were used, namely to replace the putative quinone in the HbRC: 2-methyl-1,4-naphthoquinone (vitamin K_3, VK_3), tetramethyl-1,4-benzoquinone (duroquinone, DQ) and 9,10-dioxoanthracene (antraquinone, AQ).

A similar procedure was used before for successful quinone replacement in PS I [Itoh, 2001] [Pushkar, 2005].

Approx. 300 μM HbRC in 50 mM MOPS, pH = 7, 0.04% *n*-dodecyl-ß-D-maltoside a 15 mM solution of the respective quinone in ethanol was added (final concentration of quinone was 200 times stoichiometric excess of quinone to HbRC). The solution was stirred for 5 hours at room temperature in room light, followed by overnight dark incubation at +4 °C. NAP-10 or PD-10 columns (GE Healthcare) were used to remove excess of quinone. EPR samples were frozen in the dark on presence of 5 mM sodium ascorbate as an external electron donor.

4.3.4 Destruction of F_X

The procedure used here, involving chaotropic agents, is based on a previously published procedure for removing iron-sulfur clusters F_X in PS I [Golbeck, 1982]. 300 μM HbRC were incubated in 3 M urea, 5 mM potassium ferricyanide, MOPS 50 mM (pH = 7.0) and 0.04% *n*-dodecyl-ß-D-maltoside for 3 hours at room temperature in the dark. This was followed by purification over NAP-10 or PD-10 chromatographic column (GE Healthcare) in order to remove urea and ferricyanide. EPR samples were frozen in the dark in presence of 5 mM sodium ascorbate as an external electron donor.

4.3.5 Photoaccumulation procedure

Generation of stationary radicals in photosynthetic RC (photoaccumulation) was used to reduce electron acceptors in HbRC and block electron transfer to terminal electron acceptors. The HbRC samples (300 μM) were reduced by sodium ascorbate (final concentration 5 mM) in MOPS buffer, pH = 7 or sodium dithionite in glycine buffer, pH = 10 (final concentration of

sodium dithionite 30 mM, 100 mM glycine). Two types of samples with ascorbate-reduced HbRC were prepared. Both samples were pre-illuminated by a CW laser for 10 minutes. The first sample was the frozen in liquid nitrogen in the dark; and the second sample was frozen in liquid nitrogen under continuous illumination at 690 nm. The dithionite-reduced sample of HbRC was pre-illuminated with 690 nm CW laser for 10 minutes and frozen in liquid nitrogen under continuous illumination.

4.4 Methods: Electron paramagnetic resonance techniques

4.4.1 CW and TREPR (X, Q, W-band setups)

X-band transient EPR experiments were carried out using two setups: a Bruker ER046 XK-T Microwave Bridge equipped with a Flexline dielectric resonator (FU Berlin) and a Bruker ER042 MRH E Microwave Bridge with an ER 4118X-MD-W1 resonator (MPI Mülheim). The time resolution of both setups is approximately ~ 50-100 ns. In both setups an Oxford CF 935 helium cryostat was used. The transient EPR data were collected in direct detection EPR mode by a LeCroy 9450A digital storage oscilloscope (FU, Berlin) or SpecMan program with digitizer operated by a personal computer (MPI, Mülheim).

All X-band transient EPR spectra of the radical pair were recorded at 80 K and for triplets at 10 K and 80 K using the following parameters: mw frequency = 9.7 GHz, mw power 0.2 mW, field dimension: field sweep for measuring of the radical pair was 80 G, for triplet detection 1000 G, 256 magnetic field points; time dimension: time window 40 μs, 2000 time points. Spectra were obtained by boxcar integrating the transients signals in a time window of 0.6 – 1.6 μs.

Q-band transient EPR experiments were carried out using a Bruker ER051 QG Microwave Bridge with a home-build cylindrical resonator with optical window (MPI, Mulheim). An Oxford CF 935 helium cryostat was used. Transient EPR data was collected using the direct detection EPR mode by the SpecMan program with digitizer operated by a personal computer. Q-band transient EPR spectra of the radical pair were recorded at 80 K with the following parameters: mw frequency = 33.9 GHz, mw power 0.2 mW. All other parameters are the same.

W-band EPR measurements were performed using a home-built W-band (95 GHz) multipurpose EPR spectrometer described previously [Möbius, 2009] [Mobius, 2005]. The spectrometer was equipped with a TE_{011} optical transmission cavity. The heterodyne microwave bridge allowed us to perform continuous wave (cw), transient and pulsed EPR experiments.

A home-built high-field (HF) EPR spectrometer [Reijerse, 2007] equipped with an ICE-Oxford cryogenic system was used for the experiments at 244 GHz. These high-field EPR experiments have been carried out without a resonator using induction mode detection.

Recombination kinetics data was obtained by recording X-band transient EPR absorption after laser flash (532 nm), using lock-in transient detection with magnetic field modulation (100 kHz, 0.3 mT modulation amplitude). The transient EPR measurements of the short lived transients were performed using the direct detection technique, with a time resolution of ~100 ns.

Samples for time-resolved EPR were excited using the second harmonic of the Nd:YAG Laser (Vibrant 355 II, OPOTEK Inc.) at 532 nm with a repetition rate of 10 Hz. The OPO (Optical Parametric Oscillator, OPOTEK Inc.) setup was used for wavelength-dependent measurements (action spectrum). The laser power after OPO was ≈ 10 mJ/cm^2 for 532 nm. Light was supplied to the resonator by an optical fiber. For excitation at 690 nm, a CW diode laser

(25mW output, about 10mW on the sample surface, light saturation condition) was used, guided to the center of the EPR cavity through a quartz fiber.

4.4.2 Pulsed EPR/ENDOR (X- and Q-bands setups)

EPR and ENDOR experiments in liquid solution were performed at 260 K and special TRIPLE experiments were carried out over a temperature range of 200-280 K. CW EPR, ENDOR, general and special TRIPLE measurements at X-band were performed on a Bruker ESP 300 X-band EPR spectrometer with a home-built ENDOR TM_{110}-type cavity, similar to the one previously described [Zweygart,1994]. For special TRIPLE experiment a Rhode & Schwarz RF signal generators Type SMT 02 and Type SMX and home build 2 side band modulator were used. The temperature was controlled with a Bruker ER4111 VT nitrogen flow system.

EPR spectra of Chl a^- in liquid solution were measured under the following conditions: modulation frequency 12.5 kHz, modulation amplitude 1G, microwave power 0.7 mW, time constant 20 ms, 3 scans. ENDOR spectra of Chl a^- in liquid solution were measured with the following conditions: rf power 100 W, microwave power 40 mW, field modulation ± 50 kHz deviation, 30 scans, time constant 163 ms. For special TRIPLE the following conditions were used: rf power 100 W, fm deviation ± 25 kHz, 20 scans. The baseline was recorded under the same conditions, but on a off-resonance magnetic field position. Subtraction was done to remove possible artificial broad lines from the resonator.

X-band pulse EPR, ENDOR and HYSCORE measurements on frozen solution samples at 80 K were performed on a Bruker ELEXSYS E580 FT EPR X-band spectrometer with a Super X-FT microwave bridge equipped with an ER 4118X-MD5-W1 resonator. Temperature was controlled with an Oxford CF935 helium cryostat. For pulse EPR and ENDOR

measurements a travelling wave tube (TWT) amplifier was used. ENI A-500 (500W) RF amplifier was used for the ENDOR measurements. Field-sweep echo-detected EPR (FSE EPR) spectra were detected using a two-pulse echo sequence ($\pi/2$-τ-π-τ-echo), where the echo intensity was detected as a function of applied magnetic field. Microwave (MW) pulses lengths were $\pi/2$ = 8 ns, π = 16 ns. Two-pulse ESEEM experiment were detected using a two-pulse echo sequence ($\pi/2 - \tau - \pi - \tau$ - echo): $\pi/2$ = 8 ns, π = 16 ns, τ = 160 ns.

In addition to ESEEM and HYSCORE experiments, matching ESEEM and HYSCORE experiment were done to increase the resolution of spectra [Schweiger, 2001]. Three-pulse ESEEM experiment were detected using the three-pulse echo sequence ($\pi/2 - \tau$ - $\pi/2 - T$ - $\pi/2 - \tau$ - echo), τ = 100 ns. HYSCORE experiments were detected using the two-dimensional four-pulse stimulated-echo ($\pi/2 - \tau$ - $\pi/2 - t1$ - $\pi - t2$ - $\pi/2$ - echo): $\pi/2$ = 8 ns, π = 16 ns, τ = 128 ns, t1 = t2 = 100 ns with step *dx* = *dy* = 20 ns. In order to avoid artefacts in the spectra caused by unwanted echoes four-step phase cycles were employed in the stimulated echo ESEEM and HYSCORE experiments [Schweiger, 2001].

Q-band pulse EPR, ENDOR, ESEEM, HYSCORE and TRIPLE measurements on frozen solution samples at 80 K were done on a Bruker ELEXSYS E580 FT EPR Q-band spectrometer with a Super Q-FT Microwave Bridge equipped with a home-built resonator [Sienkiewicz, 1996]. An ENI 3200L (300W) RF amplifier for ENDOR or Amplifier Research Model 2500L (2500/4000 W) RF amplifier for TRIPLE were used. Q-band FSE spectra were recorded using the following conditions: MW pulses lengths were $\pi/2$ = 40 ns, π = 80 ns and time between pulses was τ = 340 ns for Chl a^- samples and τ = 400 ns for A_0^- samples. Proton ENDOR was recorded using the Davies ENDOR pulse sequence with an inversion pulse π = 200 ns, t = 25 μs, radiofrequency (RF) π-pulse of 20 μs and detection sequence ($\pi/2 - \tau - \pi - \tau$ - echo). Q-band

ENDOR spectra were recorded in stochastic mode. Two-pulse ESEEM experiment were detected using the two-pulse echo sequence ($\pi/2 - \tau - \pi - \tau$ - echo): $\pi/2$ = 40 ns, π = 80 ns, τ = 148 ns. HYSCORE experiments were detected using the two-dimensional four-pulse stimulated-echo ($\pi/2 - \tau$ - $\pi/2$ – t1 - π – t2 - $\pi/2$ - echo): $\pi/2$ = 8 ns, π = 16 ns, t1 = t2 = 100 ns with step $dx = dy$ = 32 ns. HYSCORE experiments were recorded for three different τ values: 296, 392, 464 ns.

All spectra were recorded using the standard Bruker data acquisition software. All data processing and simulations were done using the MatLab™ program. EPR and ENDOR data were simulated using the Easy Spin software package version 3.0.0 [Stoll, 2006].

Bibliography to Chapter 4

Golbeck J.H., Warden J.T. (1982) Electron Spin Resonance Studies of the Bound Iron-sulfur Centers in Photosystem I - Photoreduction of Center A Occurs in the Absence of Center B. Biochimica et Biophysica Acta, 681, 77-84.

Heathcote P., Moenne-Loccoz P., Rigby S. E. J, Evans M. C. W. (1996) Photoaccumulation in Photosystem I Does Produce a Phylloquinone $A_1^{\bullet-}$ Radical. Biochemistry, 35, 6644-6650.

Heinnickel M. (2007) Study of the Iron-sulfur Cluster and Polypeptide Composition of the Photosynthetic Reaction Center from Heliobacterium modesticaldum. Doctoral thesis, The Pennsylvania State University.

Heinnickel M., Shen G., Agalarov R., Golbeck J.H. (2005) Resolution and Reconstitution of a Bound Fe-S Protein from the Photosynthetic Reaction Center of *Heliobacterium modesticaldum*. Biochemistry,. 44, 9950-9960.

Iriyama K., Ogura N., Takamiya A. (1974) A Simple Method for Extraction and Partial Purification of Chlorophyll from Plant Material, Using Dioxane. J. Biochemistry, 76, 901-904.

Itoh S., Iwaki M., Ikegami I. (2001) Modification of Photosystem I Reaction Center by the Extraction and Exchange of Chlorophylls and Quinones. Biochimica et Biophysica Acta,. 1507, 115-138.

Jubert C, Bailey G. (2007) Isolation of Chlorophylls *a* and *b* from Spinach by Counter-current Chromatography. J. Chromatography A, 1140, 95-100.

Möbius K. and Savitsky A. (2009) High-Field EPR Spectroscopy on Proteins and their Model Systems: Characterization of Transient Paramagnetic States. Publisher: London: RSC.

Möbius K., Savitsky A., Schnegg A., Plato M. and Fuhs M. (2005) High-field EPR Spectroscopy Applied to Biological Systems: Characterization of Molecular Switches for Electron and Ion Transfer. Phys. Chemistry Chem. Physics,. 7, 19-42.

Niklas J. (2007) Investigation of the Electron donor P_{700} and the Electron Acceptor A_1 in Photosystem I of Oxygenic Photosynthesis Using EPR Spectroscopy. Technical University: Berlin.

Parriott D. (1993) A Practical Guide to HPLC Detection. Publishers: Acad. Pr., San Diego.

Porra R.J., Thompson W.A., Kriedemann P.E. (1989) Determination of Accurate Extinction Coefficients and Simultaneous Equations for Assaying Chlorophylls a and b Extracted with Four Different Solvents: Verification of the Concentration of Chlorophyll Standards by Atomic Absorption Spectroscopy. Biochimica et Biophysica Acta, 975, 384-394.

Pushkar Y.N Karyagina I., Stehlik D., Brown S., van der Est A. (2005) Recruitment of a Foreign Quinone into the A_1 Site of Photosystem I. Consecutive Forward Electron Transfer from A_0 to A_1 to F_X with Anthraquinone in the A_1 Site as Studied by Transient EPR. J. Biol. Chemistry, 280, 12382-12390.

Schweiger A. and Jeschke G. (2001) Principles of Pulse Electron Paramagnetic Resonance. Publishers: Oxford University Press, Oxford.

Sienkiewicz A., Smith, B. G., Veselov, A., Scholes, C. P., (1996) Tunable Q-band Resonator for Low Temperature Electron Paramagnetic Resonance Electron Nuclear Double Resonance Measurements. Review of Scientific Instruments, 67, 2134-2138.

Stoll S. and Schweiger A., (2006) EasySpin, a Comprehensive Software Package for Spectral Simulation and Analysis in EPR. J.Magn. Resonance, 178, 42-55.

Zweygart W., Thanner R., Lubitz W. (1994) An Improved TM110 ENDOR Cavity for Investigation of Transition Metal Complexes. J.Magn.Resonance, 109, 172-176.

Chapter 5. Results: primary electron acceptor A_0 in PS I: *in vitro* and *in vivo*

5.1 Introduction

Photosystem I (PS I) is a pigment protein complex in the membrane of oxygenic photosynthetic organisms, *i.e.* cyanobacteria, algae and higher plants. The PS I, a Type I reaction center, has as the terminal acceptor in the electron transfer chain [4Fe-4S] clusters. The main process in PS I is light-induced transmembrane electron transfer (ET). The ET process starts by charge separation between donor and acceptor molecules (cofactors) and subsequent electron transfer steps involve a series of redox active cofactors, separating the charge across the membrane.

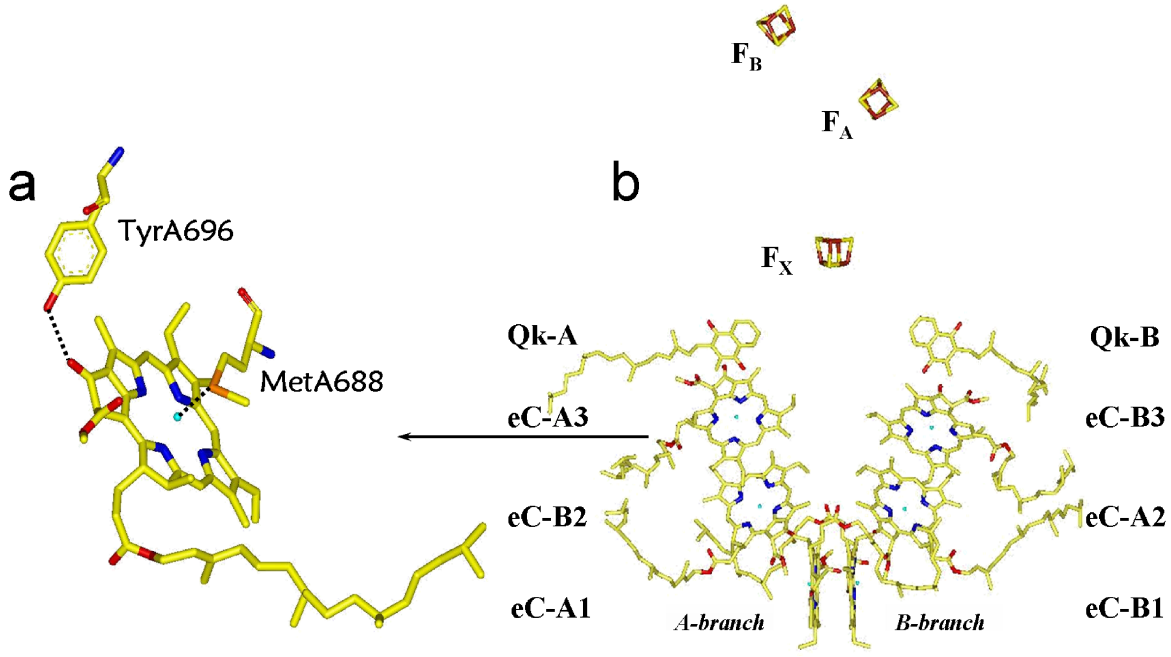

Figure 5.1 (*a*) Binding pocket of A_0 in the A branch of the ET chain. The chlorophyll cofactor (eC-A3) is axially liganded by MetA688 and forms an additional hydrogen bond with TyrA696 (details see in text). (*b*) ET cofactors in cyanobacterial PS I located in PsaA, PsaB and PsaC subunits (PDB entry 1JB0, *Synechococcus elongates* [Jordan, 2001]). Cofactors are arranged in two ET branches A and B.

The ET cofactors are arranged in two branches A and B (Fig.5.1*b*), corresponding to the main subunits of PS I. Uni- or bidirectionality of the ET in PS I is still a subject of debate [Redding, 2006] [Golbeck, 2009]. The key cofactors of the ET are described in Chapter I. Chapter 5 is focused on the electronic structure of the primary electron acceptor A_0. The understanding of features of the A_0 cofactor in the PS I complex is important in the investigation of the initial processes of PS I.

The question about the nature of the electron acceptor A_0 in PS I was resolved by absorption difference spectroscopy. The absorption difference spectrum of A_0/A_0^- was obtained from a study of charge recombination in the primary pair $P_{700}^{\bullet+}A_0^{\bullet-}$ in a PS I, where the secondary acceptor A_1 (phylloquinone) and antenna pigments (carotenoids and chlorophylls) were extracted by ethyl ether [Mathis, 1988]. This study showed bleaching around 690 and 430 nm and absorption increases at 760 and 460 nm, compatible with A_0 being a Chl *a* with its Q_Y transition shifted to 690 nm. Similar results were obtained in the PS I treated with Triton X-100 under reducing condition, that blocked ET from A_0 to A_1 [Nuijs, 1986].

The X-ray crystallographic structure of PS I confirmed the presence of two Chl *a* molecules (eC-A3/eC-B3), which are symmetrically arranged in the A and B branches of the ET chain [Jordan, 2001]. The primary electron acceptor A_0 is a Chl *a* monomer (eC-A3/eC-B3), which is located between the donor P_{700} and the secondary acceptor A_1 (Fig.5.1*b*) [Jordan, 2001]. The Chl *a* molecules in the A_0 binding sites have methionine sulfur (S) as ligand to the central metal ion Mg^{2+} of Chl *a* in both ET branches (MetA688 in A-branch of ET and MetB668 in B-branch [Jordan, 2001] (Fig.5.1*a*)). The Mg^{2+} - S distance is 2.6 Å. The interaction between the hard acid Mg^{2+} and the soft base S is energetically unfavorable due to Pearson's acid

base concept [Pearson, 1963]. This unusual interaction could contribute to its extremely low redox potential (approximately -1050 mV).

Short hydrogen bonds are provided by the hydroxyl groups of tyrosines TyrA696 (A-branch) and TyrB676 (B-branch) to the keto oxygens of rings V of the Chls *a* in the A_0 binding sites (distance O-O = 2.7 Å), respectively [Jordan, 2001].

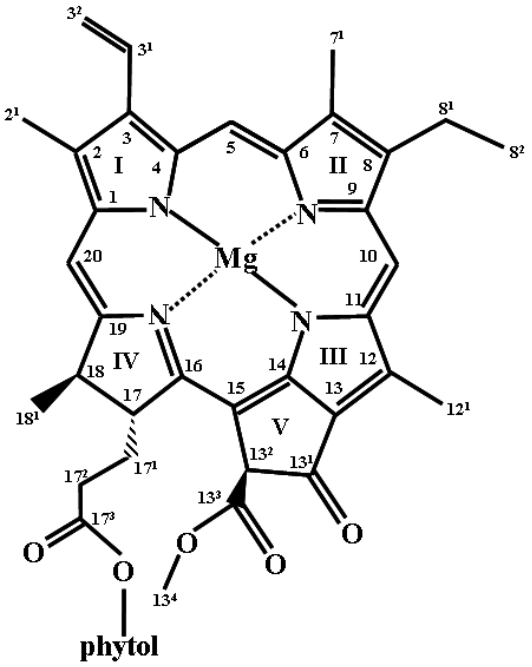

Figure 5.2 Structure of Chl *a*. The numbering of the protons is according to the IUPAC system.

The properties and function of the Chl *a* anion radical (Chl $a^{\bullet-}$) in the A_0 binding site in the PS I are largely determined by the local environment, including hydrogen bonds and electrostatic and/or dielectric fields. These factors determine the spin distribution of the Chl $a^{\bullet-}$ in the A_0 binding site, which from this point will be called to as the $A_0^{\bullet-}$ radical. The **g**-tensor, hyperfine

(hfc) and nuclear quadrupole (nqc) coupling tensors, which can be resolved by advanced EPR techniques, are sensitive to the electronic structure of $A_0^{\bullet-}$.

Electron paramagnetic resonance (EPR) spectroscopy is a very informative method to determine the electronic structure of paramagnetic species, which appear during the photosynthetic processes. The investigation of short-lived intermediate states is possible by transient and pulse EPR techniques [Stehlik, 1997] [Hoff, 1982] [Prisner, 2001] [Lubitz, 2002] [Lubitz, 2003]. The EPR spectroscopic investigation of the radical pair $P_{700}^{\bullet+}A_0^{\bullet-}$ is very difficult due to the short lifetime of this state (~ 10 ns). However, studies of the photoaccumulated radical of cofactor A_0 are feasible. The photoaccumulation procedure in the presence of reducing agent (sodium dithionite) is widely used for generation of the stationary phyllosemiquinone radicals of the A_1 in PS I [Bonnerjea, 1982] [Heathcote, 1996]. However, modifications of the photoaccumulation procedure (temperature, illumination time) can result in accumulation of the A_0 radical. These radicals can be often stabilized and studied with continuous wave EPR spectroscopy [Feher, 1978].

The analysis of the EPR spectra of the $A_0^{\bullet-}$ radical is difficult because of the effect of interaction between protein and cofactors. Thus, the first step of the work was a detailed investigation of a model system of the photoaccumulated radical of $A_0^{\bullet-}$, the electrochemically generated Chl *a* anion radical. The electrochemical experiments were done in a home-build setup under dim green light to protect Chl molecules from damage.

Advanced EPR techniques (ENDOR, TRIPLE, ESEEM and HYSCORE) were used for a determination of the hyperfine and quadrupole coupling parameters of the electrochemically generated Chl $a^{\bullet-}$ and the photoaccumulated radical of $A_0^{\bullet-}$ (see details of the methods in

Chapter 2 and 3). Davies ENDOR was applied for the determination of proton hyperfine couplings of the radicals. The ESEEM techniques (3-pulse ESEEM and HYSCORE) were used for measurements of small hyperfine and nuclear quadrupole interactions, especially for the ^{14}N atoms in the porphyrin macrocycle of Chl *a*. The relative signs of the hfcs of Chl $a^{\bullet-}$ were studied by TRIPLE resonance spectroscopy. The details of these methods are described in Chapter 2.

EPR spectroscopic results were compared with density function theory (DFT) calculations. By comparison with the Chl *a* radical anion in organic solvent, the electronic structure of the primary electron acceptor A_0 and the role of the protein surrounding, can be further resolved.

5.2 Results and discussion: Chlorophyll a anion radical in solution

5.2.1 Electrochemistry of chlorophyll a

Several authors have previously discussed the electrochemical behavior of Chl *a* in solution [Felton, 1964] [Kiselev, 1973] [Saji, 1977]. The reduction of Chl *a* is characterized by two one-electron waves. The cyclic voltammogram of Chl *a* in DME solvent shows reduction waves with half-wave potentials of -1.14 and -1.61 V *vs.* the saturated calomel electrode (SCE) [Saji, 1977]. These potentials corresponded to reduction of Chl *a* to Chl $a^{\bullet-}$ (anion radical) and to Chl $a^{2\bullet-}$ (double reduced anion radical). The reduction of Chl *a* is attributed to an electron transfer to the porphyrin ring rather than to the central metal atom.

The cyclic voltammogram (CV) for the sample of ~1 mM Chl *a* in the solvent dimethoxyethane (DME) with electrolyte 0.1 M tetrabutylammonium-tetrafluoroborate ($TBABF_4$)

is shown at Fig.5.3. CV was used for control of the potential for the singly reduced anion of the Chl *a*. The coulometry technique determines the amount of sample transformed during an electrolysis reaction by measuring the amount of charge (in coulombs) (see calculation of production of the anion below). For details of the electrochemical treatment of Chl *a* anion radical see in Chapter 4.

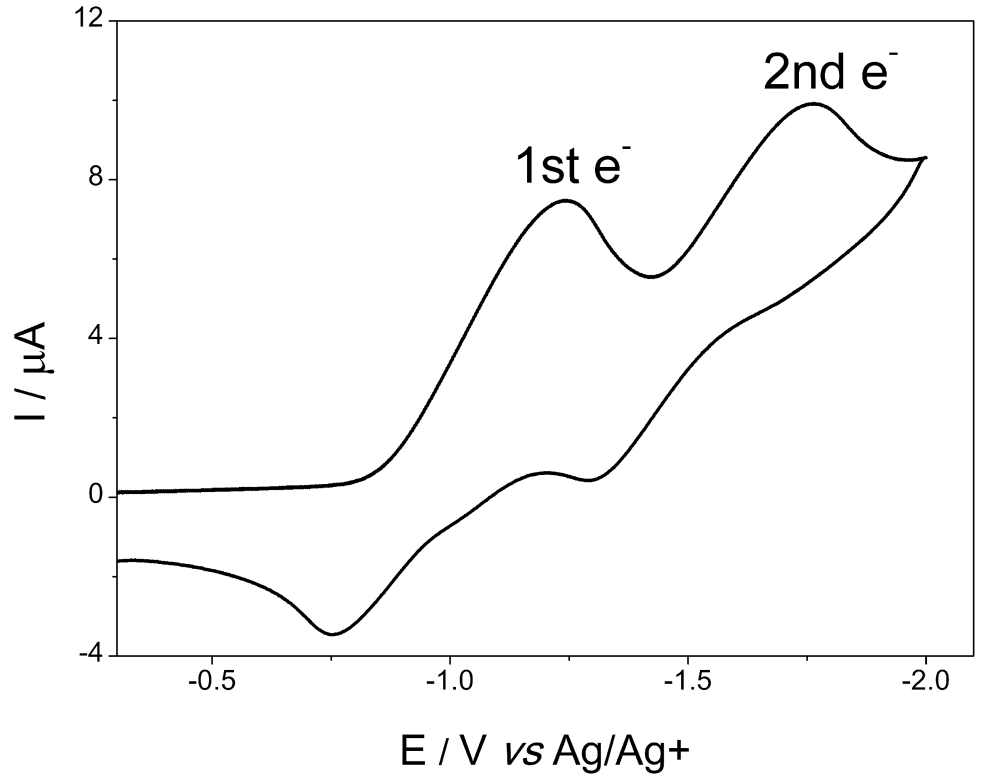

Figure 5.3 Cyclic voltammogram (CV) for 1 mM Chl *a* in DME solution with supporting electrolyte 0.1 M $TBABF_4$ recorded at room temperature. Scan rate of the CV was 100mV/s.

The CV of Chl *a* shows two reduction waves with potentials of -1.23 and -1.76 V *vs.* Ag/Ag+ reference electrode. This reference electrode was used for determination of the potential, which further used for coulometry. The potential *versus* Ag/Ag+ reference electrode are relative, therefore for further coulonometry was taken not the

midpotential, but maximum. Clear reversal peaks for the two reduction waves were observed. The small signal between reversible waves probably corresponds to impurities of the sample.

The reduction processes, Chl *a* to Chl $a^{\bullet-}$ and to Chl $a^{2\bullet-}$**,** can be attributed to electron transfer to the porphyrin ring [Felton, 1966] rather than to the central metal atom. The half-wave potential separation of 0.52 V compares well with that of a series of metalloporphyrins and chlorophyll [Clack, 1965] [Saji, 1977]. A potential of -1.23 V was chosen for production of the singly reduced Chl *a* anion radical.

The coulometry (figure not shown) at a selected potential (-1.23 V) in the electrochemical cell charge of 81.2 mC was produced. Theoretical calculations, based on the Faraday law of electrolysis, require that one-electron reduction for 1 mM sample in a 1 ml cell creates a charge equals 96.5 mC. This value denotes total reduction of the sample that means sample consists of 100 % anion radicals. Thus, during the performed experiment of the electrochemical treatment on Chl *a* ~ 84% of one-electron reduced anion radical in the solution was obtained. Additional CV measurements were performed after each coulometry experiment to confirm that a potential did not shift. The next step of investigation was the characterization of the electrochemical generated Chl $a^{\bullet-}$ by EPR methods.

5.2.2 CW EPR and ENDOR spectra of the Chl $a^{\bullet-}$ radical in liquid solution

The X-band EPR spectrum of the electrochemically generated Chl $a^{\bullet-}$ in liquid DME solution, recorded at 260 K, is shown in the insert panel of Fig. 5.4. Chl $a^{\bullet-}$ in solution exhibits an unresolved isotropic EPR spectrum with linewidth ~ 10 ± 0.5 G, which was previously observed by Hoff et al. [Hoff, 1982]. The study of the electronic structure by EPR

methods is difficult due to the low spectral resolution. However, the spectral resolution can be greatly improved by ENDOR measurements.

The ^{1}H ENDOR spectrum of the Chl $a^{\bullet-}$ in liquid and frozen solution was reported previously [Fujita, 1978] [Hoff, 1982]. Fujita et al. determined the hyperfine couplings (hfcs) of the two methyl group protons at position 2^1 and 12^1 (5.47 and 11.35 MHz respectively). The ENDOR resonances of the methyl groups were relatively narrow and weakly axial, because the methyl groups can rotate at the temperatures at which measurements were made [Hyde, 1968]. A more detailed analysis of ENDOR measurements of Chl $a^{\bullet-}$ in solution was done in the work of Hoff et al. [Hoff, 1982]. As a consequence, EPR/ENDOR measurements of the electrochemical generated Chl $a^{\bullet-}$ in liquid solution in this work were done for control of the quality of the sample by the use of the comparison with previous work of Hoff at al.

The X-band CW ENDOR spectrum of the electrochemical generated Chl $a^{\bullet-}$ in liquid DME solution recorded at 260 K is depicted at Fig. 5.4. An ENDOR spectrum of the Chl $a^{\bullet-}$ shows seven pairs of lines. Only the isotropic hfc parameters can be determine from such CW ENDOR spectrum in liquid solution, because the motion of radicals in solution is fast enough to average out the dipolar part of the hyperfine interaction of the spin Hamiltonian. The proton hfc constants obtained from the ENDOR spectrum of the electrochemically generated Chl $a^{\bullet-}$ in DME solution are collected in the Table 5.1 and compared with previously published data.

The comparison of the ENDOR spectrum of the Chl $a^{\bullet-}$ in DME solution is in good agreement with previously reported data [Hoff, 1982]. The agreement of the hfcs of Chl $a^{\bullet-}$ provides additional evidence that during the electrochemical treatment generated the singly reduced Chl $a^{\bullet-}$.

The next step of the work was the investigation of the Chl $a^{\bullet-}$ by advanced pulse EPR techniques in X and Q-band in frozen solution (80 K). The measurements at low temperature are necessary to compare the EPR data of model Chl $a^{\bullet-}$ with the photoaccumulated radical $A_0^{\bullet-}$ in PS I, because the $A_0^{\bullet-}$ radical can only be trapped by freezing.

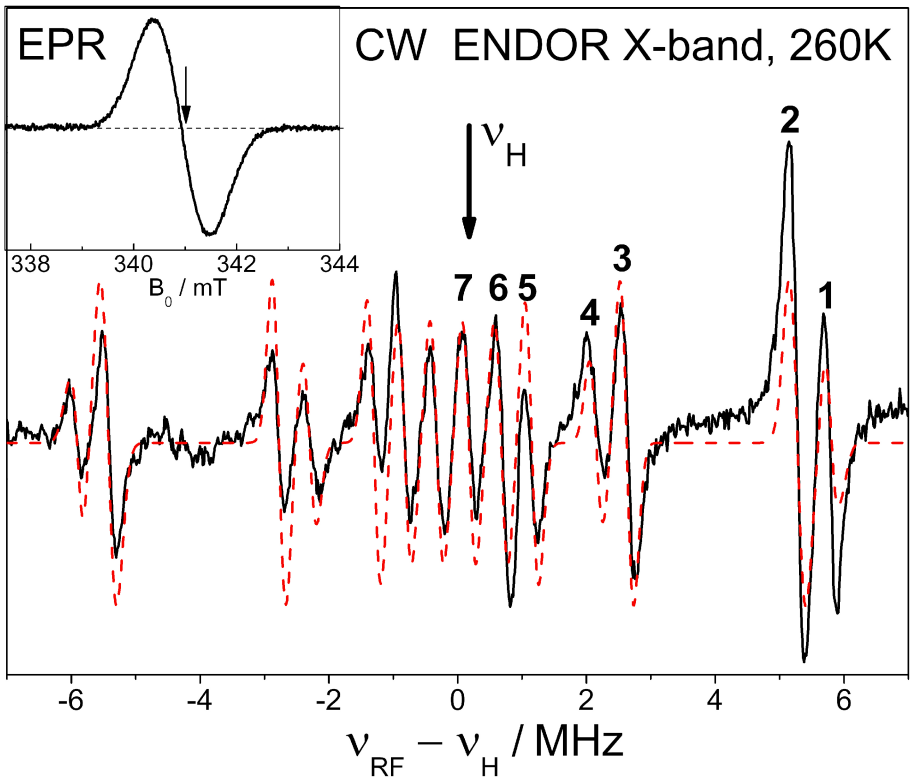

Figure 5.4 CW X-band EPR spectrum (insert) and CW ^{1}H ENDOR spectrum of the electrochemically generated Chl $a^{\bullet-}$ in DME solution with electrolyte ($TBAF_4$) recorded at T = 260 K. ^{1}H ENDOR spectrum taken at the field position which corresponds to the maximum of the EPR absorption indicated with an arrow in the EPR spectrum in the insert panel. The black curve corresponds to experimental ENDOR spectrum and red line is simulation of ENDOR spectrum. Experimental conditions: field modulation 12,5 kHz, modulation amp. 1 G, MW power 0.2 mW; ^{1}H ENDOR spectrum parameters: field 3410.6 G, RF power 100 W, MW power 40 mW, T = 260 K, 30 scans.

Table 5.1 Experimental isotropic ^{1}H hyperfine constants (MHz) of Chl a$^{\bullet-}$ in DME solution are obtained from liquid solution ENDOR measurements (260 K).

Line #	a_{iso} experimental values [a] (^{1}H ENDOR spectrum of the Chl *a*$^-$ at 260 K)	a_{iso} experimental values from [Hoff, 1982]	^{1}H position, Fig.5.2
1	- 11.73	- 11.68	**10**
2	10.69	10.58	**12^1**
3	5.44	5.43	**2^1**
4	- 4.46	- 4.67; - 4.37	**20, 5**
5	- 2.45	- 2.48; - 2.32	**3^2**
6	1.51	1.7; - 1.53; 1.45	**13^3, 8^1, 18^1**
7	0.48	0.54; 0.3	**7^1, 3^1, 17^2**

a) Signs of hfc constants were determined by general TRIPLE of the electrochemical generated Chl *a*$^{\bullet-}$ in frozen solution (see below), details see in the text.

5.2.3 Advanced EPR/ENDOR measurements on the Chl a$^{\bullet-}$ in frozen solution

Previously ENDOR studies of the Chl *a*$^{\bullet-}$ in frozen solution were done in X-band and showed hfcs only from the methyl groups 2^1 and 12^1 [Fujita, 1978]. In the present work, studies were conducted using two frequency ranges X- (9.8 GHz) and Q- (34 GHz) bands, which provided better resolution.

The pulse Q-band EPR (insert) and ENDOR (black line) spectra of the electrochemically generated Chl *a*$^{\bullet-}$ in frozen solution at 80 K are presented in Fig.5.6. The EPR spectrum of the Chl *a*$^{\bullet-}$ consists of an inhomogeneously broadened Gaussian line with a width of ~ 17 ± 1 G. Unfortunately, the EPR spectrum of Chl *a*$^{\bullet-}$ shows no resolved **g**-tensor components and no hfc structure. Therefore, the EPR spectrum does not allow to obtain any additional information about

parameters of the electronic structure in Chl $a^{\bullet-}$. The hyperfine and quadrupole coupling parameters can, however, be obtained from ENDOR and HYSCORE methods, which are presented below. The **g**-tensor components can be resolved in high-field EPR measurements.

CW high-field (244 GHz) EPR measurements on Chl $a^{\bullet-}$: The majority of the published transient EPR data on photosynthetic reaction centres have been measured at a microwave frequency of X-band (9 GHz). However, high field/frequency EPR techniques can give more detailed information about magnetic field-dependent interactions. For example, comparison of multi-frequency EPR data helps to more accurately determine the components of the **g**-tensor in paramagnetic molecule. For instance, due to high field EPR (W-band) measurements g-factors of partners $P_{700}^{\bullet+}$ and $A_1^{\bullet-}$ in light-induced radical pair in electron transfer chain of PS I were resolved [van der Est, 1997] [Zech, 2000]. In this section high field EPR experiments on the electrochemically generated Chl $a^{\bullet-}$ are reported.

For field calibration in high field EPR measurement, a standard sample with well known spectroscopic parameters in the resonator together with the sample was used. The field calibration and *g*-factor determination were performed, as previously described, by using a Li:LiF4 crystal (g = 2.002293) [Stesmans, 1989]. This sample is prepared from a LiF crystal by heavy neutron irradiation and thermal treatment; as a result microscopic metallic Li clusters are formed.

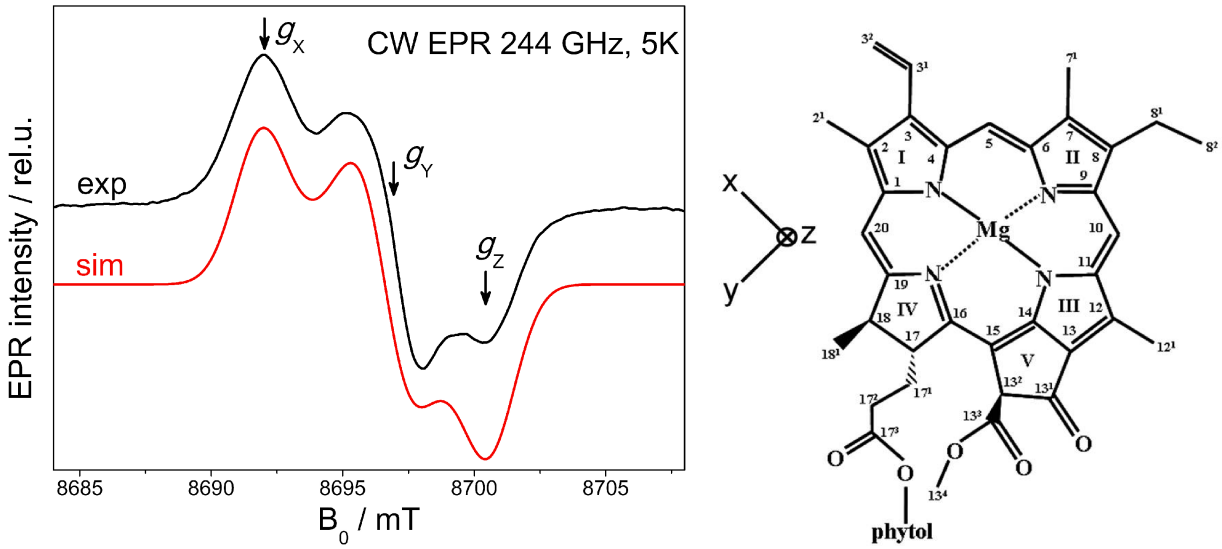

Figure 5.5 High-field (244 GHz) CW EPR spectrum of the electrochemically generated Chl $a^{\bullet-}$ (black line). Experimental conditions: temperature 5 K, microwave power 0.2 W, time constant 40 ms, modulation amplitude 1 G, modulation frequency 100 kHz. The red line is simulations using the parameters given in the text. The orientation of the **g**-tensor corresponds to Chl *a* structure is shown on the right side.

In Fig.5.5 a CW high-field (244 GHz) EPR spectrum of the electrochemically generated Chl $a^{\bullet-}$ measured at 5 K and calibrated with Li:LiF4 standard (black line) and its simulation (red line) are presented. The good resolution of the spectrum allowed the principal **g**-tensor values to be determined with high accuracy. The fitted **g**-tensor values were: $g_X = 2.00391$; $g_Y = 2.00282$; $g_Z = 2.00190$ (error $\pm 3 \cdot 10^{-5}$).

Davies ENDOR spectrum (Q-band): The Q-band ENDOR spectrum of the electrochemically generated Chl $a^{\bullet-}$ in DME solution was measured at 80 K in the spectral position, which corresponds to the maximum of the EPR absorption, indicated on the EPR spectrum (insert) with an arrow. The Q-band ENDOR spectrum of the Chl $a^{\bullet-}$ in frozen solution

shows six pairs of lines and an unresolved central line. The ENDOR lines of Chl $a^{\bullet-}$ in frozen solution (80 K) are broader than the lines in liquid solution (260 K). However, the isotropic hfcs determined in liquid solution are assumed to be similar to the ones determined in frozen solution.

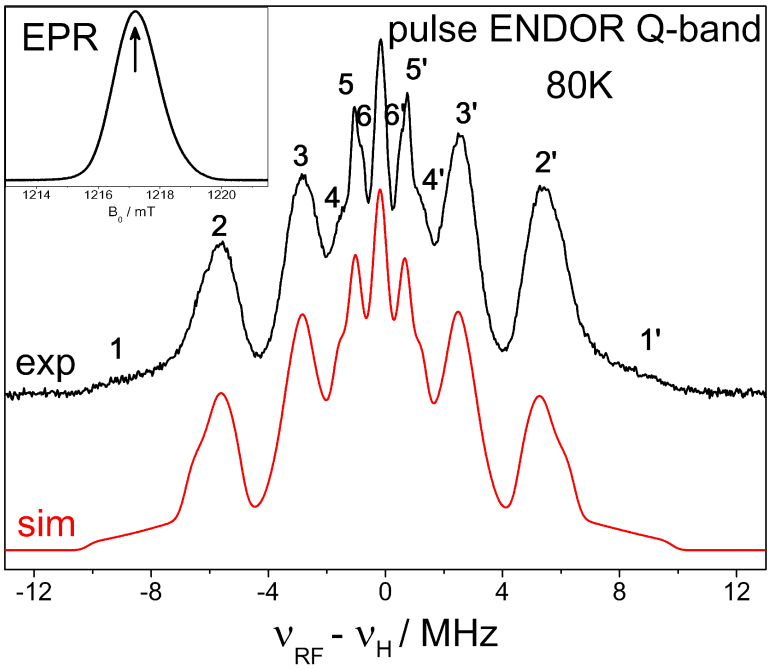

Figure 5.6 Pulse Q-band EPR spectrum (insert) and ^{1}H Davies Q-band ENDOR spectrum (black line) of the electrochemically generated Chl $a^{\bullet-}$ in DME solution recorded at T = 80 K and simulated ENDOR spectrum (red line) with hfcs from Table 5.2. The ^{1}H ENDOR spectrum was taken at the field position corresponding to the maximum of the EPR absorption.

Since the lineshapes of ENDOR spectra are quite complicated, direct analysis of the spectrum is difficult. Therefore, a simulation of the ENDOR spectra was performed in order to extract the hfc constants. The simulated ENDOR spectrum showed good agreement with the experimental data as presented in Fig.5.6, red line. The parameters used for simulations are summarized in Table 5.2. The assignment of ENDOR lines was done on the basis of previously

determined hfcs of Chl $a^{\bullet-}$ in liquid solution and the simulation of the ENDOR spectrum of Chl $a^{\bullet-}$ in frozen solution.

ENDOR lines assignment: The broad and weak line 1/1', (a_{iso} is 12.8 MHz) is assigned to the methine proton at position 10 (see structure of Chl *a* at Fig.5.2).

ENDOR lines 2/2' result from the methyl groups at positions 12^1. The hfcs corresponding to the 12^1 methyl group (11.3 MHz) was always larger than that of the other methyl protons [Fujita, 1978]. For the methyl group, an average isotropic hfc constant is given under the assumption that the methyl group can rotate freely.

The simulation of the ENDOR spectrum of the Chl $a^{\bullet-}$ in frozen solution shows that line 3/3' is a superposition of ENDOR lines, which correspond to several protons: methine protons at positions 5, 20; protons of the methyl group at position 2^1 and protons of the vinyl group at position 3^2. All these protons give one ENDOR line in the range of 5.4 MHz. However, the simulation of the ENDOR spectrum allows to separate contributions and to determine hfcs for each individual proton group, seeing Table 5.2.

Line 4/4' corresponds to protons of the methyl group at the position 7^1 with hfc equal to 2.6 MHz. Line 5/5' assigned to protons at position 18^1 and 13^3, respectively. The partially resolved line 6/6' probably arises from protons of the methyl group 3^1. The central line contains small hfcs and corresponds to the matrix line which is common for ENDOR spectra of frozen samples [Schweiger, 2001]. The experimental and simulated hfcs are collected in Table 5.2. The simulated hfcs are in good agreement with DFT calculation (see details of calculation below).

Table 5.2 The simulated and DFT calculated ^{1}H hyperfine constants (MHz) of the electrochemically generated Chl $a^{\bullet-}$ obtained from frozen solution ENDOR measurements (T = 80 K).

Line	A1 / MHz		A2 / MHz		A3 / MHz		a_{iso} / MHz		Line
	exp	DFT	exp	DFT	exp	DFT	exp	DFT	
1	-8.2	-5.2	-10.3	-12.9	-20.0	-18.4	-12.8	-12.2	**10**
2	10.9	12.7	11.2	12.4	12.1	15.2	11.7	13.4	**12**^{1}
3	-1.9	-1.9	-5.7	-6.7	-8.2	-9.0	-5.3	-5.9	**5**
	-0.5	-0.8	-4.8	-4.6	-5.2	-4.9	-3.5	-3.4	**20**
	-3.8	-2.0	-5.2	-5.2	-6.9	-7.9	-5.3	-5.0	**3**^{2}
	4.5	5.6	5.2	5.8	6.2	7.7	5.3	5.9	**2**^{1}
4	-2.3	-1.8	-2.6	-2.5	-2.9	-2.6	-2.6	-2.3	**7**^{1}
5	1.5	0.7	1.5	1.0	2.3	2.5	1.8	1.4	**18**
6	0.8	0.3	0.9	0.7	1.3	3.1	1.0	1.4	**3**^{1}

TRIPLE resonance: In general, ENDOR spectroscopy does not provide information about the signs of the hfc. Therefore, the determination of the signs of the hfcs in Chl $a^{\bullet-}$ was done by using electron-nuclear nuclear TRIPLE resonance. TRIPLE spectra were subtracted from the ENDOR spectrum, which was recorded using the same experimental conditions, to make a proper analysis. Difference TRIPLE/ENDOR and corresponding ENDOR spectra of electrochemically generated Chl $a^{\bullet-}$ in DME solution at 80 K recorded at the maximum of the EPR absorption is shown at Fig.5.6. The difference TRIPLE spectrum shows only those peaks, which belong to NMR transitions of the same electron spin manifold.

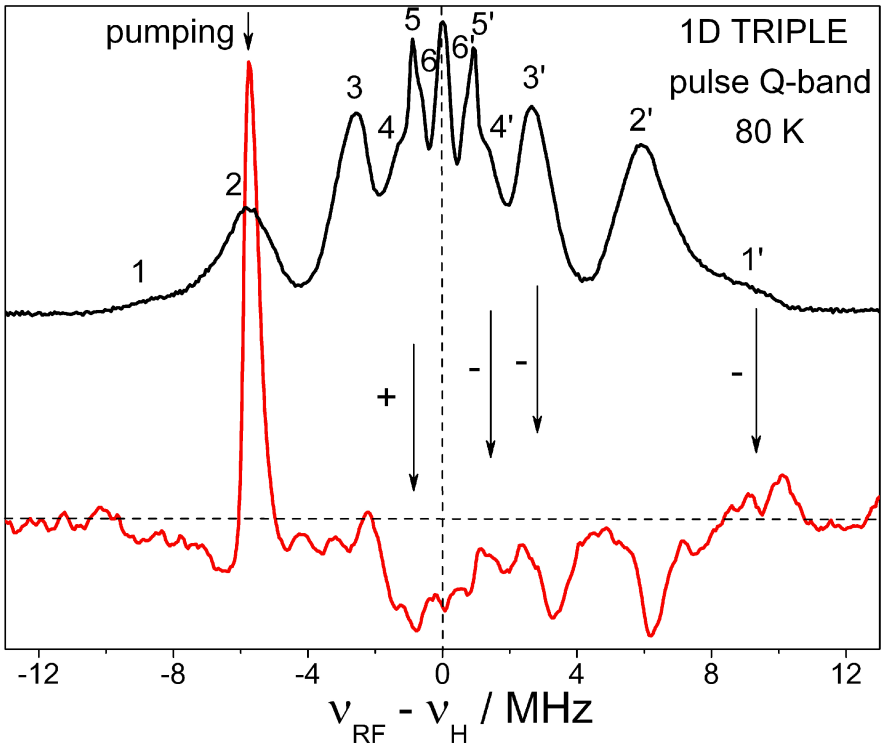

Figure 5.7 Pulse Q-band ENDOR (black line) and difference general TRIPLE/ENDOR (red line) spectra of the electrochemically generated Chl $a^{\bullet-}$ in DME solution recorded at the maximum of the EPR absorption at T = 80 K. The pumped frequency is indicated by an arrow.

The low frequency ENDOR transition of the methyl group (12^1) was used as the pumping radio frequency (marked with an arrow). The positive sign of the 12^1 methyl group is known from previous works [Fujita, 1978] [Hoff, 1982]. The nuclear transitions from the same electron spin manifold, as transition excited by the pump frequency, appear in the TRIPLE spectrum.

Since the methyl group proton hfc is positive, signals from other protons with positive hfcs are expected on the same side of the ENDOR spectrum, while negative hfcs will be observed on the opposite side with respect to the Larmor frequency. The electron spin relaxation effect which is comparable to duration of the pulse sequence can lead to the presence of "indirect" TRIPLE peaks. In Fig 5.7 peaks resulting from the "direct" TRIPLE effect, have negative

amplitude, while the peak due to spin relaxation effects is positive [Silakov, 2007]. These peaks appear due to nuclear transitions in the other electron spin manifold.

The three lines 1, 3, 4 and 5 show signals in the high frequency region. Hence it is concluded that these hfcs have negative signs. In the low frequency part of the spectrum two lines are clearly observed. These lines correspond to ENDOR line 2 and 3. The line 3 has contribution in the high and low frequency range, because this line contains proton resonances from several proton groups. The general TRIPLE spectrum of Chl $a^{\bullet-}$ in frozen solution confirms the signs of the hfcs obtained from simulation of the ENDOR spectrum. The results are collected in Table 5.1

5.2.4 Nitrogen hyperfine and quadrupole couplings of the Chl $a^{\bullet-}$.

A Chl *a* molecule has four nitrogens in its porphyrin ring (Fig.5.2). The hfcs of the nitrogens in the Chl $a^{\bullet-}$ are very small and ENDOR measurements can not clearly resolved them. In contrast to ENDOR, the electron echo envelope modulation (ESEEM) method is highly sensitive to nuclei with small magnetic moments and low lying transition frequencies such as the ^{14}N nuclei. In this work 2-pulses ESEEM and HYSCORE experiments were performed. A detailed description of these methods is given in chapter 2.

The Fourier transformation of 2-pulse ESEEM of the electrochemically generated Chl $a^{\bullet-}$ in DME solvent measured at 80 K is depicted in Fig.5.8. The modulations are caused by the presence of nuclei with I > 0, in this case four pyrrole nitrogens ($I(^{14}N) = 1$). The ESEEM spectrum of the Chl $a^{\bullet-}$ is difficult to analyze. Therefore, a further investigation was done using hyperfine sublevel correlation spectroscopy (HYSCORE).

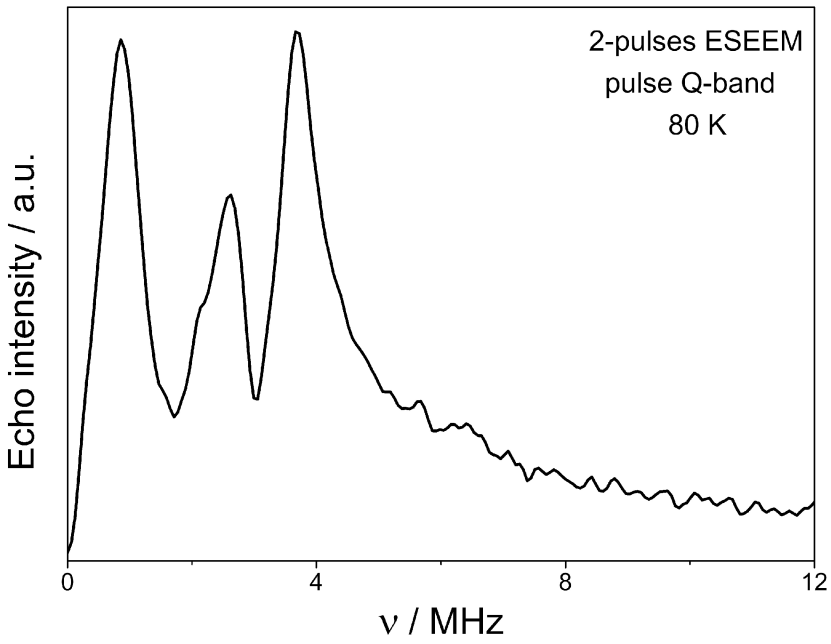

Figure 5.8 Fourier transformations of 2-pulse ESEEM time-domain traces for the electrochemically generated Chl $a^{\bullet-}$ in DME solvent recorded at the maximum of the EPR absorption at 80 K.

The X-band HYSCORE spectrum measured at the field position corresponding to the maximum of the EPR absorption is shown Fig.5.9. Since the HYSCORE spectrum is very sensitive to the value of τ, several measurements were performed with different τ (data not shown). It was found that for τ = 436 ns, spectra were obtained with maximum information.

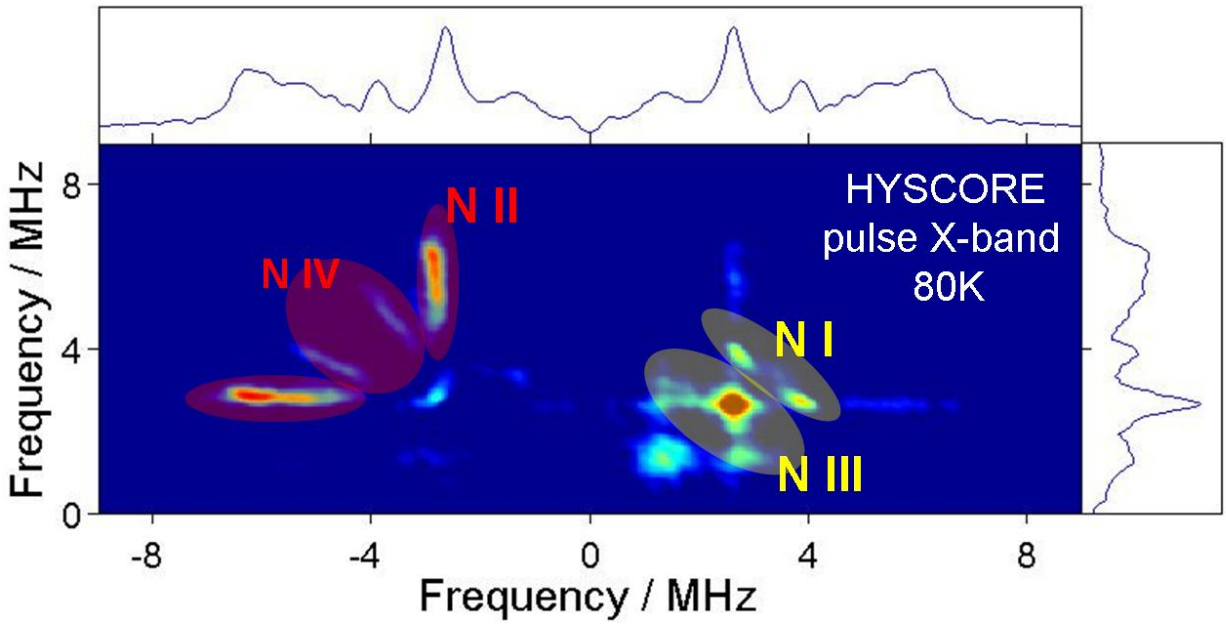

Figure 5.9 X-band HYSCORE spectra of the electrochemically generated Chl $a^{\bullet-}$ in DME solvent recorded at the maximum EPR absorption and its simulation (red and yellow areas corresponding to two groups of nitrogen). Experimental conditions: T = 80 K, τ = 436 ns.

The simulation of the X-band HYSCORE spectrum (color ranges in Fig.5.9) reveals the presence of two pairs of ^{14}N nuclei substantially differing in hyperfine couplings. Table 5.3 shows the parameters used for the simulations. The theoretical spectrum fits the experimental data well. The simulated hyperfine and quadrupole parameters are in good agreement with DFT calculation of Chl $a^{\bullet-}$, see Table 5.3.

Table 5.3 The simulated and DFT calculated hyperfine (MHz) and quadrupole constants of the electrochemically generated Chl $a^{\bullet-}$.

	A1 / MHz		A2 / MHz		A3 / MHz		a_{iso} / MHz		4K = e^2qQ/h / MHz		η	
14N	exp	DFT	exp	DFT	exp	DFT	exp	DFT	exp	DFT	exp	DFT
N I	-1.0	-0.8	-0.5	-0.8	-3.8	-3.4	-1.8	-1.7	2.36	2.44	0.60	0.61
N II	0	0	0.5	0.2	11.0	12.9	3.8	4.4	2.63	2.62	0.43	0.46
N III	-0.1	-0.2	-0.6	-0.3	-1.2	-1.4	-0.6	-0.6	2.44	2.40	0.73	0.74
N IV	0	0	-0.2	-0.1	15.0	14.6	4.9	4.8	2.40	2.44	0.80	0.79

5.3 Results and discussion: Primary electron acceptor $A_0^{\bullet-}$ in PS I

The stationary radical of the electron acceptor $A_0^{\bullet-}$ was produced by the photoaccumulation procedure that was previously used for PS I [Bonnerjea, 1982] [Heathcote, 1996]. The illumination of frozen PS I samples in the presence of sodium dithionite as reducing agent creates a phyllosemiquinone radical $A_1^{\bullet-}$ and a chlorophyll anion radical $A_0^{\bullet-}$. PS I samples with a photoaccumulated $A_0^{\bullet-}$ always contain a significant amount of the $A_1^{\bullet-}$ radical, which has an overlapping EPR spectra. Therefore, photoaccumulation conditions were selected to increase the amount of $A_0^{\bullet-}$ relative to $A_1^{\bullet-}$ in the PS I samples. The ratio of the $A_1^{\bullet-}/A_0^{\bullet-}$ radicals depends on illumination and temperature conditions in the photoaccumulation procedure. Hard photoaccumulation leads to the unwanted reduction of antenna chlorophylls [McLean, 1982]. It was shown that under carefully defined conditions the photoaccumulation was reducing one phyllosemiquinone and one chlorophyll anion species per P_{700} [Hethcote, 1993].

The contribution of the photoaccumulated $A_0^{\bullet-}$ radical was observed by the field swept echo (FSE) EPR method. . The ENDOR technique was used to determine the hyperfine couplings in the photoaccumulated $A_0^{\bullet-}$ radical. Unfortunately, the ^{14}N signals in $A_0^{\bullet-}$ are not detectable, due to protein influence to the relaxation processes. To separate the contribution of radicals $A_1^{\bullet-}$ and $A_0^{\bullet-}$ high frequency EPR/ENDOR techniques (Q-band, 34 GHz) were used. The 244 GHz high field EPR measurements were done for resolution of the **g**-tensor components of $A_0^{\bullet-}$.

Additionally, to create a maximum concentration of the $A_0^{\bullet-}$ radical the photoaccumulation procedure was performed in PS I extracted from different photosynthetic cyanobacterial organisms: *Thermosynechococcus elongatus*, *Synechocystis* sp. PCC 6803 and *men B26* mutant of *Synechocystis* with substituted deuterated vitamin K_3.

To investigate the influence of the protein surrounding on the electronic structure of the cofactor, the proton hfc tensors obtained for the photoaccumulated $A_0^{\bullet-}$ radical in PS I were compared to the proton hfc tensors obtained from the electrochemically generated Chl $a^{\bullet-}$ in frozen DME solvent. The observed changes in magnetic parameters and spin density may explain the specific interactions between Chl $a^{\bullet-}$ and the protein surrounding in the A_0 binding site in PS I.

5.3.1 EPR measurements on the photoaccumulated PS I samples

The photoaccumulation procedure for the preparation of stationary radicals in PS I was described in Chapter 4. Previous studies of the photoaccumulated radical $A_0^{\bullet-}$ in PS I were done only at X-band frequencies [Forman, 1981] [Rigby, 2003]. In this work Q-band EPR measurements are presented. The higher frequency study allows to improve the resolution of the EPR spectrum and, as a consequence, allows the contributions of the $A_0^{\bullet-}$ and $A_1^{\bullet-}$ radicals to be distinguished.

The pulse Q-band EPR spectrum of the photoaccumulated PS I sample of the *Synechocystis 6803* wild type (black line) at 80 K is shown in Fig.5.11. The additional broad line, which is indicated with a star *, at low-field range of the spectrum corresponds to the so-called signal B [Golbeck, private communication]. The nature of the signal B is unknown, but this peak appears in many EPR spectra of the PS I.

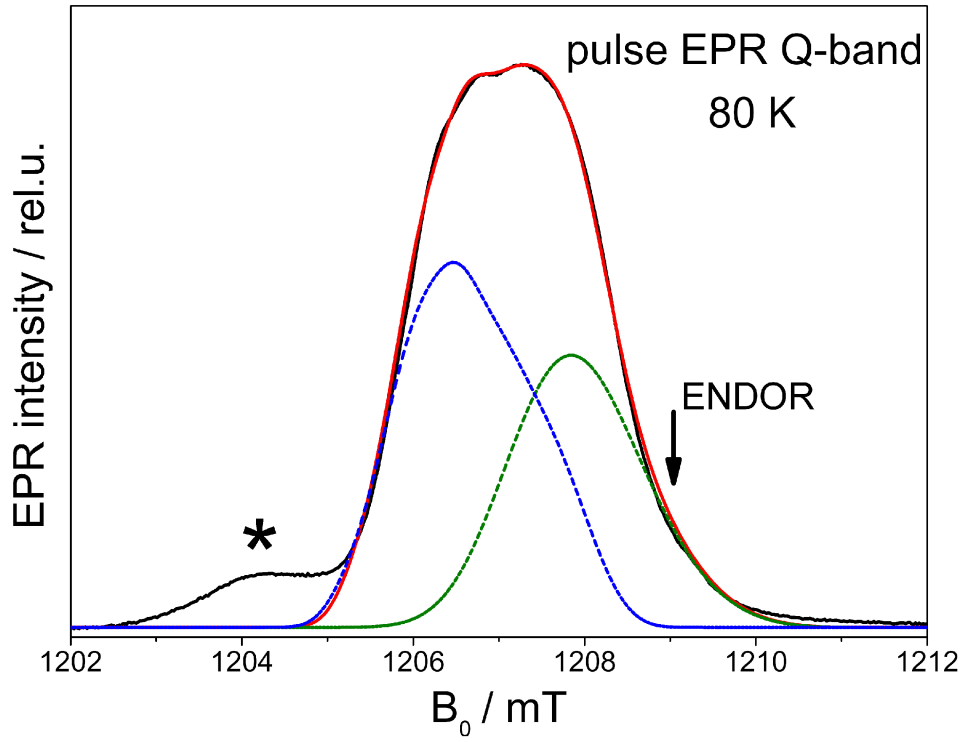

Figure 5.10 Pulse Q-band EPR spectrum of the photoaccumulated PS I from *Synechocystis 6803* wild type (black line), simulated spectrum (red line), which is sum of simulated EPR lines of the semiphylloquinone (blue line) and Chl $a^{\bullet-}$ (green line) *in vacuo*. The EPR spectrum shows a mixture of the photoaccumulated radicals $A_1^{\bullet-}$ and $A_0^{\bullet-}$. The arrow indicates the field position for ENDOR spectrum at Fig.5.13. The signal B is indicated with a star *.

As both the secondary electron acceptor $A_1^{\bullet-}$ and the primary electron acceptor $A_0^{\bullet-}$ are generated by the photoaccumulation procedure, therefore, it is unsurprised that the EPR spectra above are contained both signals (Fig.5.10). Blue and green lines in Fig.5.10 represent the simulated EPR spectrum of the semiphylloquinone, $A_1^{\bullet-}$ (blue line) and Chl $a^{\bullet-}$, $A_0^{\bullet-}$ (green line). A phylloquinone is known to function as the acceptor A_1 in the PS I complex. The parameters of both simulations are given in Table 5.4.

Table 5.4 Parameters used for simulation of the EPR spectra corresponding to phylloquinone and Chl *a*. Results are presented in Fig.5.10.

	g_1; g_2; g_3	Linewidth / mT
PhQ / A_1	2.0067; 2.0051; 2.0021	0.48
Chl *a* / A_0	2.0037; 2.0029; 2.0020	0.7

CW high-field (244 GHz) EPR measurements on the $A_0^{\bullet-}$ radical: CW high-field (244 GHz) EPR spectrum of the photoaccumulated $A_0^{\bullet-}$ radical measured at 5 K, calibrated with Li:LiF4 standard (black line) and its simulation (red line) are shown at Fig.5.11. The signal in a low-field range corresponds to the contribution of the $A_1^{\bullet-}$ radical and signal in high field position corresponds to one of the six lines of Mn contamination in PS I sample. The spectrum shows resolved anisotropy of **g**-tensor. The high resolution of the spectrum allowed the determination of the principal **g**-tensor values. Table 5.5 compares these values against the components of **g**-tensor for the electrochemically generated Chl $a^{\bullet-}$.

Table 5.5 Comparison of the principal values of the **g**-tensor of the electrochemically generated Chl $a^{\bullet-}$ and the photoaccumulated $A_0^{\bullet-}$ (error ± $3 \cdot 10^{-5}$).

g-tensor components	Chl $a^{\bullet-}$	$A_0^{\bullet-}$
g_X	2.00391	2.00378
g_Y	2.00282	2.00281
g_Z	2.00190	2.00206

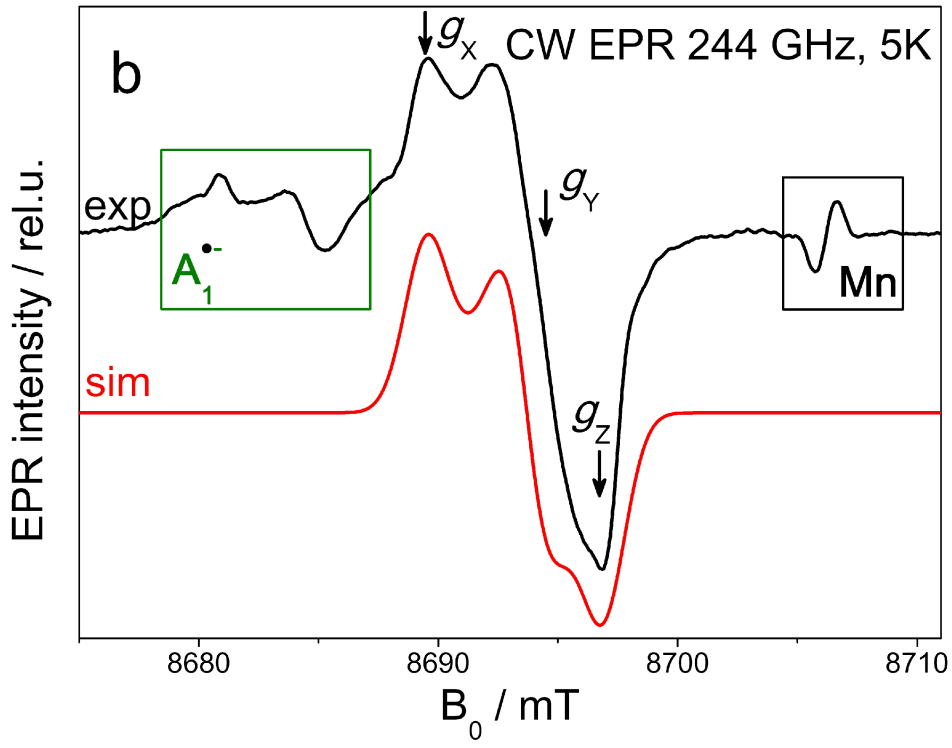

Figure 5.11 High-field (244 GHz) CW EPR spectrum of the $A_0^{\bullet-}$ radical in PS I extracted from *Synechocystis 6803* wild type. The red line is simulations using the parameters given in the text. The signal in low-field range corresponds to the contribution of the $A_1^{\bullet-}$ radical and signal in high field position corresponds to one of the six lines of Mn contamination in PS I sample. Experimental conditions: temperature 5 K, microwave power 0.2 W, time constant 40 ms, modulation amplitude 1 G, modulation frequency 100 kHz.

The ratio of the $A_1^{\bullet-}$ and $A_0^{\bullet-}$ radicals depend on the photoaccumulation conditions. The prolongation of the illumination time increases the amount of the $A_0^{\bullet-}$ radical. In the presented sample of the *Synechocystis 6803* wild type, the illumination time was 20 minutes without water filters at 205 K. These conditions were selected as the optimum for generating of the $A_0^{\bullet-}$ radical in PS I extracted from this organism.

Since the conditions for the photoaccumulation of the radical $A_0^{\bullet-}$ were determined, the question of the selection of a suitable organism for creation of significant amount of the

photoaccumulated $A_0^{\bullet-}$ radical was the next step of the study. Previous investigations of the photoaccumulated radical $A_0^{\bullet-}$ were done on PS I from subchloroplast particles [Forman, 1981] and PS I from spinach [Rigby, 2003]. PS I samples extracted from the following organisms were investigated in this work: *T.elongatus* wild type, *Synechocystis 6803* wild type and *Synechocystis 6803* menB26 with substituted deuterated vitamin K_3.

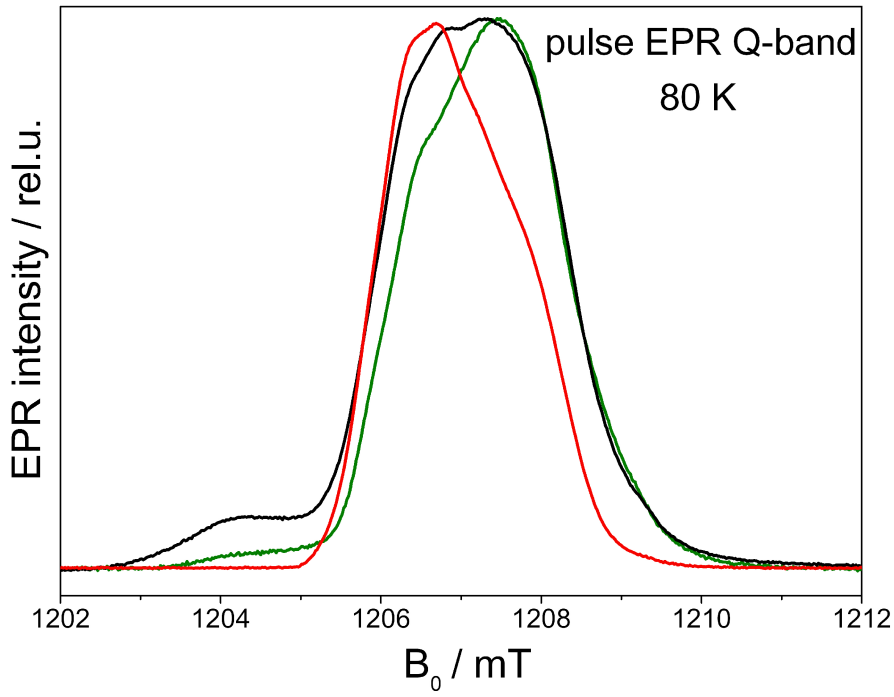

Figure 5.12 Pulse Q-band EPR spectra of the photoaccumulated samples of PS I from the three different samples: *T.elongatus* wild type (red line), *Synechocystis 6803* wild type (black line) and *Synechocystis 6803* menB26 with substituted deuterated vitamin K_3 (green line). Spectra recorded at 80 K.

It Fig.5.12, pulse Q-band EPR spectra of the photoaccumulated samples of PS I from the three different species are presented: *Synechocystis 6803* wild type (black line), *T.elongatus* wild type (red line) and *Synechocystis 6803* menB26 with substituted deuterated vitamin K_3 (green line). The photoaccumulation conditions were identical: illumination without water filters in 205 K. The comparison of EPR spectra shows that in the PS I from *Synechocystis 6803*

a photoaccumulation of the A_0^- radical proceeds easier than in *T.elongatus*. Thus, in further studies of the radical $A_0^{\bullet-}$ the PS I complex from *Synechocystis 6803* was used.

Unfortunately, a clear interpretation of the overlapping EPR spectra is difficult. However, ENDOR spectroscopy can be used for determination of the hyperfine coupling constants (hfcs) of the individual radicals.

5.3.2 ENDOR measurements on photoaccumulated PS I samples

Pulse Q-band ENDOR spectra of Chl $a^{\bullet-}$ in frozen DME solvent and the photoaccumulated $A_0^{\bullet-}$ PS I sample from the *Synechocystis 6803* wild type are presented in Fig.5.13. ENDOR spectra were recorded at a high-field position which is indicated by arrow in Fig.5.10. A negligible contribution of the radical $A_1^{\bullet-}$ is expected at this spectral position, while the radical $A_0^{\bullet-}$ does show significant contribution to the ENDOR spectrum due to its broader EPR linewidth. The comparison of the spectra shows that ENDOR signals in the photoaccumulated PS I sample (black line) correspond to ENDOR lines in the sample of the electrochemical generated Chl $a^{\bullet-}$ in frozen solvent (green line). The only difference in the photoaccumulated sample of the PS I is the additional pair of lines indicated by star * with a hfc equal to 7.1 MHz. The simulated ENDOR spectrum (Fig.5.13, red line) shows a good agreement with experimental data. The hfcs which were used for simulation are collected in Table 5.6. The spectroscopic parameters of Chl $a^{\bullet-}$ in frozen solution obtained from DFT calculations (details see above) are in good agreement with experimental data. However, the DFT calculations for the $A_0^{\bullet-}$ radical show some deviations in hfcs. This problem can be resolved in the future by DFT calculation of the influence of the individual ligand (Tyr/Met).

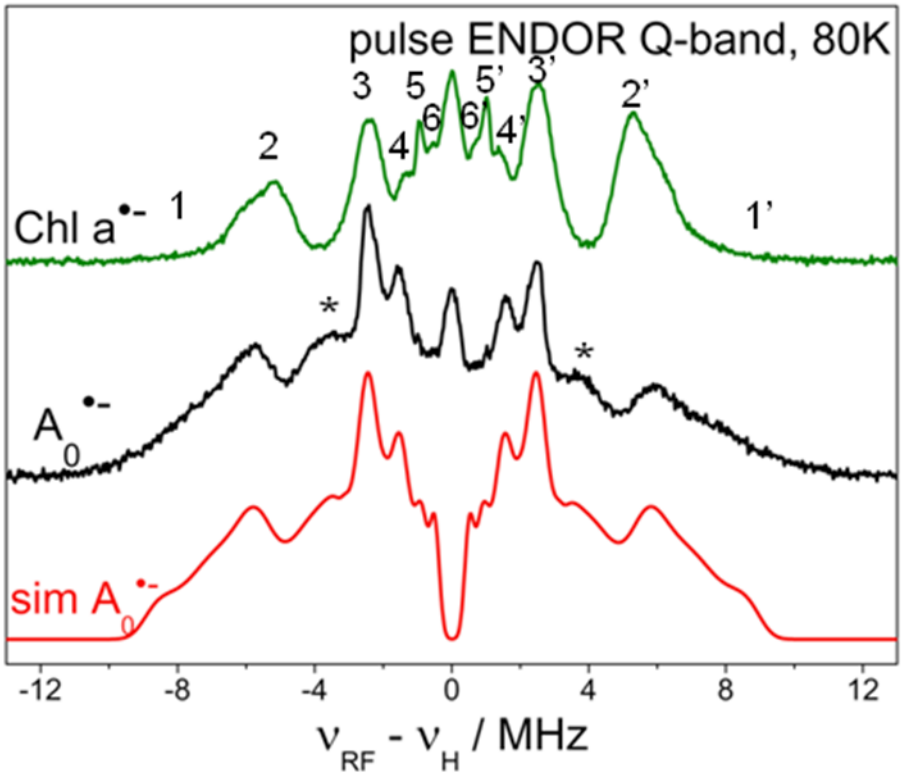

Figure 5.13 Pulse Q-band ^{1}H Davies ENDOR spectra of Chl *a*$^{\bullet-}$ in DME solvent (green line) and photoaccumulated radical $A_0^{\bullet-}$ in PS I from *Synechocystis 6803* wild type (black line) at T = 80 K. The ENDOR spectra are taken in the field position which is indicated by arrow in Fig.5.10. The parameters obtained from the simulated ENDOR spectrum of the photoaccumulated radical $A_0^{\bullet-}$ in PS I (red line) are shown in Table 5.6.

Table 5.6 The simulated and DFT calculated ^{1}H hyperfine constants (MHz) of the photoaccumulated $A_0^{\bullet-}$ radical obtained from frozen solution ENDOR measurements (T = 80 K).

Line	A1 / MHz		A2 / MHz		A3 / MHz		a_{iso} / MHz		Line
	exp	DFT	exp	DFT	exp	DFT	exp	DFT	
1	-5.8	-6.3	-8.6	-14.4	-17.9	-20.5	-10.8	-13.7	**10**
2	11.0	14.9	11.4	15.6	15.0	18.5	12.5	16.3	**12**^{1}
3	-1.7	-1.0	-4.1	-4.5	-5.1	-5.6	-3.6	-3.7	**5**
	-1.2	-0.6	-4.2	-4.3	-4.6	-4.6	-3.3	-3.2	**20**
	-2.9	-2.2	-5.1	-4.6	-5.2	-5.9	-4.4	-4.2	**3**^{2}
	3.3	5.5	3.9	5.6	6.4	7.4	4.5	6.2	**2**^{1}
4	-2.6	-2.4	-3.1	-3.0	-3.2	-3.1	-3.0	-2.8	**7**^{1}
5	1.2	0.2	1.7	0.6	2.0	0.8	1.6	0.6	**18**
6	0.9	0.2	1.0	0.6	1.2	2.8	1	1.2	**3**^{1}

The simulation of the ENDOR spectrum of the photoaccumulated radical $A_0^{\bullet-}$ shows that the additional line (*) can be explain by the large anisotropy of the hfc of the proton at position 10 and methyl group at position 12[1]. Most probably this interaction is between the reduced cofactor A_0 and the protein surrounding that leads to a slight redistribution of the spin density that manifest as small changes of the hfcs of the close protons. It is known from the X-ray structure of PS I [Jordan, 2000], the Chl *a* molecule in the A_0 binding site forms a H-bond between tyrosine (Tyr A696/Tyr B676) and the keto oxygen of ring V of the Chl *a*. It was proposed that the additional line, which appears in the ENDOR spectrum of the photoaccumulated radical $A_0^{\bullet-}$, corresponds to the H-bond between Chl *a* - Tyrosine. The additional improvement of the influence of H-bond to electronic structure of Chl *a* in A_0 binding site can be found from the measurements of PS I sample where tyrosine ligand will be deuterated or change by other ligand. In the frame of this work such samples are unavailable.

In order to exclude a contribution of $A_1^{\bullet-}$ radical to the proton ENDOR spectrum PS I from *Synechocystis 6803* menB26 with a substituted deuterated vitamin K_3 was used. In the *menB26* mutant of PS I from *Synechocystis 6803*, the pathway for biosynthesis of phylloquinone is blocked in the *menB* gene [Jonhson, 2000]. In this case, the A_1 binding site in PS I is occupied by plastoquinone-9 (PQ_9) instead of phylloquinone. The PQ_9 is only weakly bound to the A_1 protein pocket in PS I and can be easily exchanged with other quinones [Pushkar, 2004] [Niklas, 2009]. In the present study, PS I isolated from *Synechocystis menB26* with substituted deuterated vitamin K_3 (d8-VK_3) was used. Deuterated VK_3 differs from phylloquinone by a change of all protons to deuterium atoms and the lack of the phytyl tail. This sample helps to exclude proton resonances of the quinone in the ^{1}H ENDOR spectrum, but proton signal from the

H-bonding between quinone and the protein environment (Leu A722/Leu B706) still remains [Niklas, 2009].

In Fig.5.14 a Q-band EPR spectrum of the photoaccumulated radical $A_0^{\bullet-}$ in the PS I from the *Synechocystis 6803* menB26 with substituted deuterated vitamin K_3 and the simulated EPR spectrum (red line) are presented. The simulated EPR spectrum is a sum of the simulated EPR spectrum of the deuterated vitamin K_3 (blue line) and Chl $a^{\bullet-}$ (green line). As we can see in the high field range the contribution of the quinone is negligible. Thus, the ENDOR spectrum, which is detected in the high field spectral position not have contribution from the radical $A_1^{\bullet-}$ or contribution will be very small.

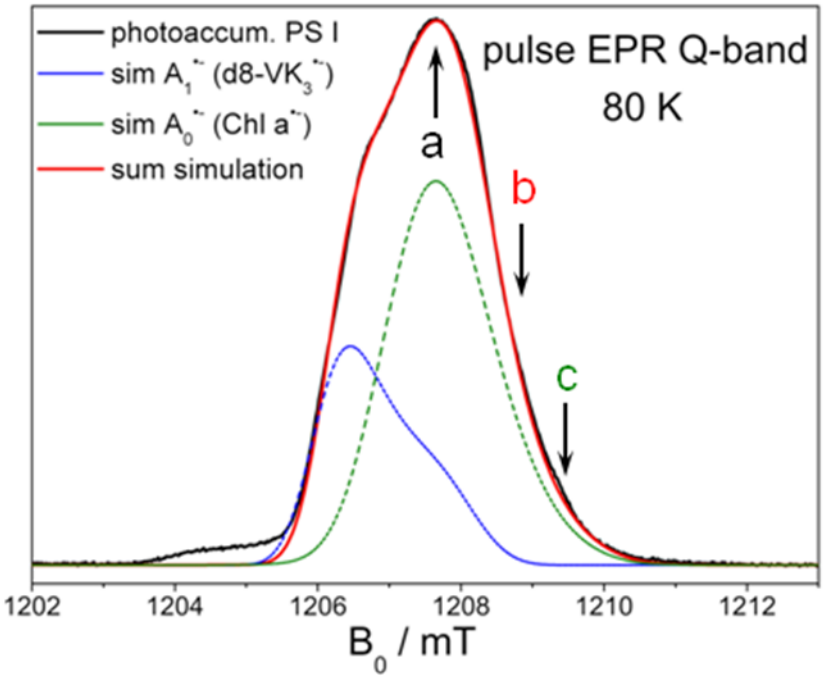

Figure 5.14 Pulse Q-band EPR spectrum of the photoaccumulated radical $A_0^{\bullet-}$ in PS I from *Syn.6803* menB26 with substituted deuterated vitamin K_3 at T = 80 K (black line). ^{1}H ENDOR spectra at Fig.5.15 are taken at the high field positions which are indicated with arrows (a, b, c). The simulated EPR spectrum (red line) is a sum of the simulated EPR spectrum of the deuterated vitamin K_3 (blue line) and Chl $a^{\bullet-}$ (green line).

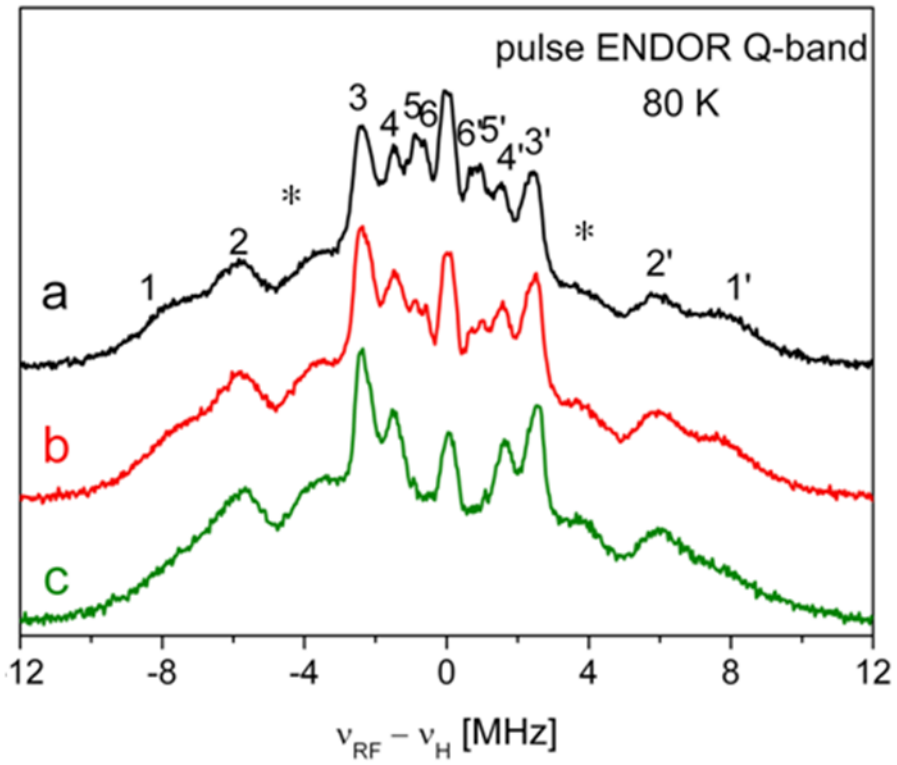

Figure 5.15 Pulse Q-band ^{1}H Davies ENDOR spectra of the photoaccumulated radical $A_0^{\bullet-}$ in PS I from *Syn.6803* menB26 with substituted deuterated vitamin K_3 at T = 80 K. The ^{1}H ENDOR spectra are taken at the field positions which are indicated by arrows (a, b, c) in the EPR spectrum (Fig.5.14). The ENDOR lines indicated with star * are additional line in the photoaccumulated $A_0^{\bullet-}$ in PS I.

Q-band ^{1}H Davies ENDOR spectra of the photoaccumulated radical $A_0^{\bullet-}$ in PS I from *Syn.6803* menB26 with substituted deuterated vitamin K_3 at T = 80 K are presented in Fig.5.15. ENDOR spectra were detected in the three different field positions, which are indicated by arrows (a, b, c) on the corresponding EPR spectrum in the Fig.5.14. The ENDOR line positions are identical in all three measurements (Fig.5.15), and the additional pair of lines (indicated with stars *) does not change significantly in all spectra. Note, that in the position ***c*** the contribution from the deuterated quinone VK_3 is negligible and thus a possible proton resonance from the H-bond between quinone in the A_1 binding site and protein should not be observed. The

additional ENDOR lines in the spectrum of the photoaccumulated PS I samples can be explained by anisotropy of the hfcs of the proton at position 10 and methyl group at position 12^1.

5.4 DFT calculations: electronic structure of Chl $a^{\bullet-}$ and $A_0^{\bullet-}$ radical

DFT calculations were performed for two model systems: *i)* Chl $a^{\bullet-}$ and *ii)* a $A_0^{\bullet-}$ model system that contains Chl $a^{\bullet-}$ with tyrosine ligand (in the native binding site - Tyr695), which creates a hydrogen bond to an oxygen molecule in the ring V of the Chl *a* molecule, and with a methionine ligand (in the native binding site - Met688) to the Mg atom (Fig.5.1*a,* [Jordan, 2000]). The phytyl chain was replaced by a methyl group. A restricted geometry optimization was performed. The optimized geometry (see Appendix) was used as input for single point calculations, which provided the spectroscopic parameters. These calculations were performed with the program package ORCA. The B3LYP functional was used in combination with the EPR II basis set, which was developed for an accurate calculation of all magnetic properties: hyperfine and quadrupole couplings. The spectroscopic parameters of Chl $a^{\bullet-}$ in solution, obtained from DFT calculations, are in good agreement with experimental data and previous calculation [Sinnecker, 2002]. However, the DFT calculations for the $A_0^{\bullet-}$ model showed some deviations. The results of the DFT calculation on the Chl $a^{\bullet-}$ in solution and $A_0^{\bullet-}$ are compared with experimental values and collected in Table 5.2, 5.3 and 5.6, the whole set of output results are presented in Table 5.7.

The single occupied molecular orbital (SOMO) of Chl $a^{\bullet-}$ and $A_0^{\bullet-}$, which were obtained by DFT calculation, are depicted at Fig.5.16. The spin density is distributed on a porphyrin ring of the Chl *a*. The largest hyperfine couplings correspond to methyl group 2^1 and 12^1 as expected

from experimental and simulated data. Also the SOMO orbital show the spin distribution between two groups of the nitrogen nuclei.

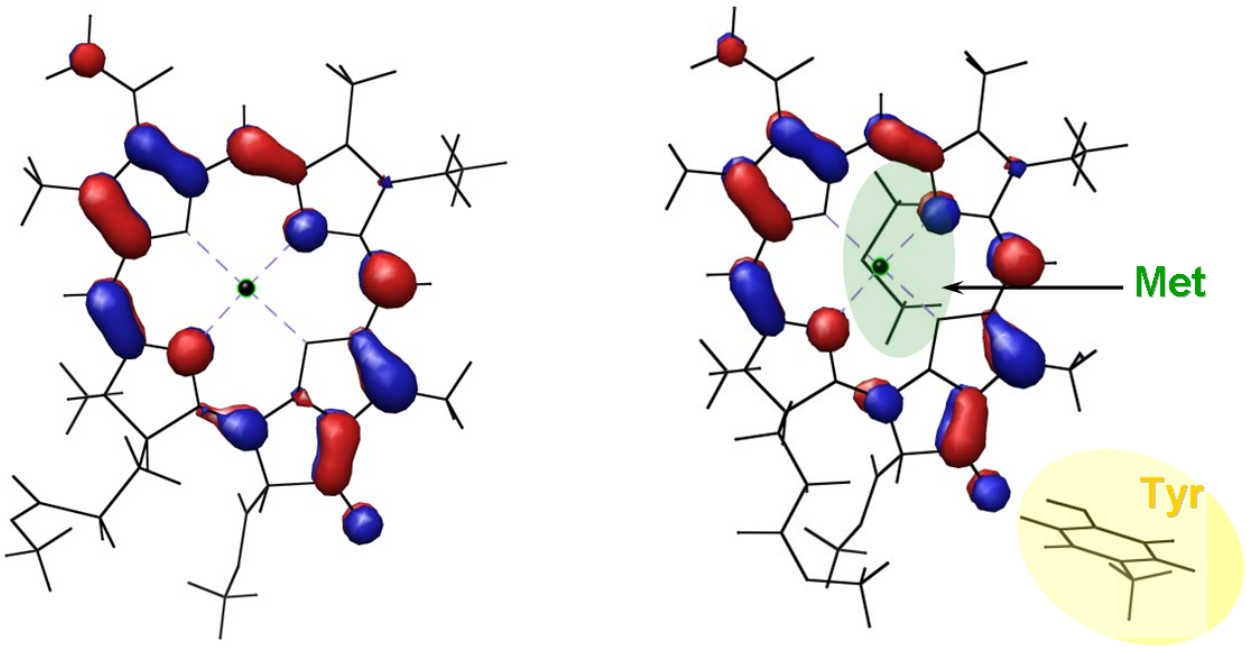

Figure 5.16 The SOMO orbital, which was obtained by DFT calculation for Chl $a^{\bullet-}$ (*a*) and Chl $a^{\bullet-}$ with tyrosine (Tyr) and methionine (Met) ligands ($A_0^{\bullet-}$) (*b*). Note: The phytyl chain was replaced by a methyl group.

Table 5.7 Results of the DFT calculation of spectroscopic parameters for the Chl $a^{\bullet-}$ radical and model of $A_0^{\bullet-}$ radical with tyrosine and methionine ligands. Numbering of the nuclei corresponds to the Chl *a* structure at Fig.5.2.

Nuclei			Chl $a^{\bullet-}$					$A_0^{\bullet-}$			
			A1 / MHz	A2 / MHz	A3 / MHz	a_{iso} / MHz	a_{iso} [a] / MHz	A1 / MHz	A2 / MHz	A3 / MHz	a_{iso} / MHz
β-proton	**17**	exp	-	-	-	-	-	-	-	-	-
		DFT	-0.2	-0.9	-1.5	-0.9	-0.5	-0.7	-1.2	-1.7	-1.2
	18	exp	1.5	1.5	2.3	1.8	-	1.2	1.7	2.0	1.6
		DFT	0.7	1.0	2.5	1.4	1.3	0.6	0.8	2.3	1.2
	13^2	exp	-	-	-	-	-	-	-	-	-
		DFT	-0.3	0.7	-1.4	-0.2	-0.4	-0.4	1.1	-2.3	-0.6
methime protons	**5**	exp	-1.9	-5.7	-8.2	-5.3	-	-1.7	-4.1	-5.1	-3.6
		DFT	-2.0	-6.7	-9.0	-5.9	-5.9	-0.9	-4.5	-5.6	-3.7
	10	exp	-8.2	-10.3	-20.0	12.8	-	-5.8	-8.6	-17.9	-10.8
		DFT	-5.2	-13.0	-18.4	-12.2	-12.1	-6.3	-14.4	-20.5	-13.7
	20	exp	-0.5	-4.8	-5.2	-3.5	-	-1.2	-4.2	-4.6	-3.3
		DFT	-0.8	-4.6	-4.9	-3.4	-3.6	-0.6	-4.3	-4.6	-3.2
vinyl protons	**3^1**	exp	0.8	0.9	1.3	1.0	-	0.9	1.0	1.2	1.0
		DFT	0.3	0.7	3.2	1.4	1.2	0.2	0.6	2.8	1.8
	3^2	exp	-3.8	-5.2	-6.9	-5.3	-	-2.9	-5.1	-5.2	-4.4
		DFT	-2.0	-5.2	-7.9	-5.0	-4.8	-1.7	-4.6	-6.9	-4.4
	3^2	exp	-	-	-	-	-	-	-	-	-
		DFT	-2.5	-5.3	-6.8	-4.9	-4.7	-2.2	-4.6	-5.9	-4.2
methyl-groups CH_3	**2^1**	exp	4.5	5.2	6.2	5.3	-	3.3	3.9	6.4	4.5
		DFT	5.7	5.9	7.7	6.4	6.4	5.5	5.7	7.4	6.2
	7^1	exp	-2.3	-2.6	-2.9	-2.6	-	-2.6	-3.1	-3.2	-3.0
		DFT	-1.8	-2.5	-2.6	-2.3	-2.2	-2.4	-3.0	-3.1	-2.8
	12^1	exp	10.9	11.2	12.1	11.7	-	11.0	11.4	15.0	12.5
		DFT	12.2	12.4	15.2	13.3	12.7	14.9	15.6	18.5	16.3
	18	exp	-	-	-	-	-	-	-	-	-
		DFT	0.7	1.0	2.5	1.4	1.4	0.2	0.6	0.8	0.5
	8^2	exp	-	-	-	-	-	-	-	-	-
		DFT	-0.2	-0.3	0.60	0.05	-	-0.2	-0.3	0.6	0.05
	13^4	exp	-	-	-	-	-	-	-	-	-
		DFT	-0.2	-0.2	0.30	0.05	-	-0.1	-0.2	0.3	0
	Phytol CH_3	exp	-	-	-	-	-	-	-	-	-
		DFT	-0.1	-0.1	0.2	0	-	-0.1	-0.2	0.3	0
CH_2	**17^1**	exp	-	-	-	-	-	-	-	-	-
		DFT	-0.3	-0.1	1.0	0.2	0.19	0	-0.1	0.2	0.03
	8^1	exp	-	-	-	-	-	-	-	-	-
		DFT	-0.1	-0.1	1.1	0.3	0.25	-0.2	-0.3	1.5	0.4
	17^2	exp	-	-	-	-	-	-	-	-	-
		DFT	-0.1	-0.2	0.3	0	-	-0.4	-0.4	0.5	-0.1

Nuclei			Chl *a*$^{\bullet-}$						
			A1 / MHz	A2 / MHz	A3 / MHz	a_{iso} / MHz	a_{iso} [a)] / MHz	4K / MHz	η
^{14}N Nitrogens	**I**	exp	-1.0	-0.50	-3.80	-1.80	-	2.36	0.6
		DFT	-0.78	-0.81	-3.39	-1.66	-1.52	2.44	0.605
	II	exp	0	0.50	11.0	3.80	-	2.63	0.430
		DFT	-0.02	0.24	12.88	4.37	4.20	2.62	0.457
	III	exp	-0.10	-0.60	-1.20	0.60	-	2.44	0.730
		DFT	-0.16	-0.27	-1.38	-0.60	-0.65	2.40	0.735
	IV	exp	0	-0.20	15.0	4.90	-	2.40	0.8
		DFT	0.02	-0.13	14.56	4.81	4.61	2.44	0.792

a) see ref. [Sinnecker, 2002]

Nuclei			$A_0^{\bullet-}$					
			A1 / MHz	A2 / MHz	A3 / MHz	a_{iso} / MHz	4K / MHz	η
^{14}N Nitrogens	**I**	exp	-	-	-	-	-	-
		DFT	-0.71	-0.76	-3.84	-1.77	2.45	0.69
	II	exp	-	-	-	-	-	-
		DFT	-0.08	0.17	11.88	3.99	2.60	0.56
	III	exp	-	-	-	-	-	-
		DFT	-0.04	-0.11	-0.63	-0.26	2.40	0.88
	IV	exp	-	-	-	-	-	-
		DFT	-0.04	-0.19	12.83	4.20	2.45	0.91

5.5 Summary and outlook

The electronic structure of the Chl $a^{\bullet-}$ anion radical in liquid and frozen solution and in the A_0 protein binding site of cyanobacterial PS I has been presented in this chapter. The PS I from *Thermosynechococcus elongatus*, *Synechocystis* sp. PCC 6803 and *men B26* mutant of *Synechocystis* with substituted deuterated vitamin K_3 organisms were used for photoaccumulation of the $A_0^{\bullet-}$ radical.

The initial step of the $A_0^{\bullet-}$ radical study was an investigation of the model system: the electrochemically generated Chl $a^{\bullet-}$ in liquid and frozen solution. Chl $a^{\bullet-}$ in solution was prepared by electrochemical methods in the home-built cell. The hyperfine and quadrupole parameters of the Chl $a^{\bullet-}$ were resolved by different pulsed EPR techniques at X- and Q-band frequencies. ENDOR and TRIPLE measurements in liquid and frozen solutions allowed the hyperfine proton couplings and their signs to be determined. The assignment of all ENDOR lines of the Chl $a^{\bullet-}$ in frozen solution was achieved. The HYSCORE method was used to resolve the small coupling of the nitrogen of the Chl *a*. Advanced EPR spectroscopic results were compared with density functional theory (DFT) calculations. DFT calculations of the spectroscopic parameters were in good agreement with experimental hyperfine and quadrupole couplings obtained from the ENDOR, TRIPLE and HYSCORE spectra. The obtained anisotropic hfcs are in good agreement with previous calculation [Sinnecker, 2002]. The combination of pulsed EPR and DFT calculations allowed the whole set of the magnetic parameters to be determined and a description the spin density distribution of the Chl $a^{\bullet-}$ to be realized.

High field (244 GHz) EPR measurements allowed **g**-tensor components of the Chl $a^{\bullet-}$ in frozen solvent and $A_0^{\bullet-}$ radical in PS I to be determined.

The photoaccumulation procedure used to generate the $A_0^{\bullet-}$ radical always yielded a mixture of the $A_0^{\bullet-}$ and $A_1^{\bullet-}$ radicals. In order to separate their contributions, Q-band (34 GHz) EPR techniques were used. Additionally, to generate the maximum concentration of $A_0^{\bullet-}$ radical, the photoaccumulation procedure was performed in PS I extracted from the different photosynthetic cyanobacterial organisms: *Thermosynechococcus elongatus*, *Synechocystis* sp. PCC 6803 and *men B26* mutant of *Synechocystis* with substituted deuterated vitamin K_3. The modified photoaccumulation procedure produced the highest ratio of $A_0^{\bullet-}/A_1^{\bullet-}$ radicals.

It was shown that hfcs of the electrochemical generated Chl $a^{\bullet-}$ anion radical and photoaccumulated $A_0^{\bullet-}$ radical are close (see Tables). The additional ENDOR line (*) in the photoaccumulated $A_0^{\bullet-}$ radical appears due to the large anisotropy of the hfcs of proton in position 10 and methyl group in position 12[1]. The redistribution of the spin density of Chl *a* arises as a result of influence of the H-bonding bonding between oxygen in keto group of Chl *a* molecule and hydrogen atom of the tyrosine ligand.

The electronic structures of Chl $a^{\bullet-}$ and model system of the $A_0^{\bullet-}$ radical were further analyzed by DFT calculation. The theoretical model of $A_0^{\bullet-}$ included the main ligands, a tyrosine and methionine.

Additional measurements of the $A_0^{\bullet-}$ radical photoaccumulation procedure to the PS I from other organisms (e.g. *Chlamydomonas reinhardtii*) should extend our knowledge about differences of the protein binding sites in the PS I from cyanobacterial organisms and higher plants.

Bibliography to Chapter 5

Bonnerjea J. and Evans M. C. W. (1982) FEBS Letters, 148, 313-316.

Clack D.W. and Hush N.S. (1965) Successive One-Electron Reduction Potentials of Porphins and Metal Porphins in Dimethylformamide. J. Amer. Chem. Society, 87, 4238-4242

Feher G. (1956) Observation of Nuclear Magnetic Resonances via the Electron Spin Resonance Line. Physics Reviews, 103, 834-835.

Felton R. H. and Linschitz H. (1966) Polarographic Reduction of Porphyrins and Electron Spin Resonance of Porphyrin Anions. J. Amer. Chem. Society., 88, 11-13.

Felton R., Sherman G. M. and Linshitz H. (1964) Formation of Phase Test Intermediate of Chlorophyll by Electrolytic Reduction. Nature, 203, 637.

Forman A, Davis M.S., Fujita I., Hanson L.K., Smith K.M. and Fajer J. (1981) Mechanisms of Energy Transduction in Plant Photosynthesis. Israel J. Chemistry, 21, 265-269.

Fujita I., Davis M.S. and Fajer J. (1978) Anion Radicals of Pheophytin and Chlorophyll *a* – Their Role in the Primary Charge Separations of Plant Photosynthesis. J. Amer. Chem. Society, 100, 6280-6282.

Golbeck J.H, private communication.

Golbeck J.H. and Cornelius J.M. (1986) Biochimica et Biophysica Acta, 849, 16-24.

Heathcote P., Hanley J.A. and Evans M.C.W. (1993) Double-Reduction of A_1 Abolishes the EPR Signal Attributed to A_1^- - Evidence for C2 Symmetry in the Photosystem I Reaction Center. Biochimica et Biophysica Acta, 1144, 54-61.

Hofbauer T. (2001) Electron Paramagnetic Resonance at 94 GHz: Methodological Developments and Studies of Photosynthetic Reaction Centers. PhD Thesis, Berlin.

Hoff A.J., Lendzian F., Möbius K. and Lubitz W. (1982) Proton and Nitrogen Electron Nuclear Double and Triple Resonance of the Chlorophyll *a* Anion in Liquid Solution. Chem. Phys. Letters, 85, 3-8.

Hyde J.S., Rist G.H. and Eriksson L.E. (1968) ENDOR of Methyl, Matrix and Alpha Protons in Amorphous and Polycrystalline Matrices. J. Phys. Chemistry, 72, 4269–4276,

Johnson T.W., Shen G., Zybailov B., Kolling D., Reategui R., Beauparlant S., Vassiliev I.R., Bryant D.A., Jones A.D., Golbeck J.H. and Chitnis P.R. (2000) Recruitment of a Foreign Quinone into the A_1 Site of Photosystem I: I. Genetic and Physiological Characterization of Phylloquinone Biosynthetic Pathway Mutants in *Synechocystis sp PCC* 6803. J. Biol. Chemistry, 275, 8523–8530.

Jordan P., Fromme P., Witt H.T., Klukas O., Saenger W. and Krauss N. (2001) Three-dimensional Structure of Cyanobacterial Photosystem I at 2.5 Å Resolution. Nature, 411, 909-917.

Kiselev B. A., Kozlov Y. N. and Yerstigneyev Y. B. (1973) Electrochemical Study of Chlorophyll. 2. Reduction of Chlorophyll and Further Transformation of Anion Radical. Biofizika, 18, 59-63.

Mathis P., Ikegami I. and Setif P. (1988) Nanosecond Flash Studies of the Absorption-Spectrum of the Photosystem I Primary Acceptor A_0. Photosynth. Research, 16, 203–210.

McLean M.B. and Sauer K. (1982) The Dependence of Reaction Center and Antenna Triplets on the Redox State of Photosystem I. Biochimica et Biophysica Acta, 679, 384-392.

Niklas J., Epel B., Antonkine M.L., Sinnecker S., Pandelia M.E. and Lubitz W. (2009) Electronic Structure of the Quinone Radical Anion $A_1^{\bullet -}$ of Photosystem I Investigated by Advanced Pulse EPR and ENDOR Techniques. J. Phys. Chemistry, 113, 10367-10379.

Nuijs A.M., Shuvalov V.A., Van Gorkom H.J., Plijter J.J. and Duysens L.N.M. (1986) Picosecond Absorbency Difference Spectroscopy on the Primary Reactions and the Antenna-excited States in Photosystem I Particles. Biochimica et Biophysica Acta, 850, 310–318.

Pearson R.G. (1963). Hard and Soft Acids and Bases. J. Amer. Chem. Society, 85, 22.

Pushkar Y. N., Stehlik D., van Gastel M. and Lubitz W. (2004) Asymmetric Hydrogen-bonding of the Quinone Cofactor in Photosystem I Probed by C-13-labeled Naphthoquinones. J. Mol. Structure, 700, 233–241.

Redding K. and van der Est A. (2006) The Directionality of Electron Transport in Photosystem I. In: Golbeck J.H. (eds) Photosystem I: The Light-Driven Plastocyanin: Ferredoxin Oxidoreductase. Advances in Photosynthesis and Respiration, vol. 24, 413-437, Publishers: Springer, Dordrecht.

Rigby S.E.J., Evans M.C.W. and Heathcote P. (2003) ENDOR and Special Triple Resonance Spectroscopy of A_1^- of Photosystem I. Biochemistry, 35, 6651-6656.

Saji T. and Bard A.J. (1977) Electrogenerated Chemiluminescence. 29. The Electrochemistry and Chemiluminescence of Chlorophyll *a* in N,N-dimethylformamide Solutions. J. Amer. Chem. Society, 99, 2235-2240.

Schweiger A. and Jeschke G. (2001) Principles of Pulse Electron Paramagnetic Resonance. Publishers: Oxford University Press, UK.

Silakov A., Reijerse E.J., Albracht P.J., Hatchikian E.C. and Lubitz W. (2007) The Electronic Structure of the H-Cluster in the [FeFe]-Hydrogenase from *Desulfovibrio desulfuricans*: a Q-band ^{57}Fe-ENDOR and HYSCORE Study. J. Amer. Chem. Society, 129, 11447-11458.

Sinnecker S., Koch W. and Lubitz W. (2002) Chlorophyll *a* Radical Ions: A density functional study. J. Phys. Chemistry B, 106, 5281-5288.

Stesmans A. and van Gorp G. (1989) Novel Method for Accurate *g* Measurements in Electron-spin Resonance, Review of Scientific Instruments., 60, 2949–2952.

van der Est A., Prisner T., Bittl R., Lubitz W., Stehlik D., and Möbius K. (1997) Time-resolved X-, K-, and W-band EPR of the Radical Pair state $P_{700}^{+}A_1^{-}$ of Photosystem I in Comparison with $P_{865}^{+}Q_A^{-}$ in Bacterial Reaction Centers. J. Phys. Chemistry B, 101, 1437–1443.

Zech S.G., Hofbauer W., Kamlowski A., Fromme P., Stehlik D., Lubitz W., and Bittl R. (2000) A Structural Model for the Charge Separated State $P_{700}^{+}A_1^{-}$ in Photosystem I from the Orientation of the Magnetic Interaction Tensors. J. Phys. Chemistry B, 104, 9728–9739.

Chapter 6. Characterization of the heliobacterial reaction centers by multi-frequency electron paramagnetic resonance spectroscopy.

6.1 Introduction

Heliobacterium was accidentally discovered in 1981 due to a failure in the preparation of a culture of anoxygenetic photosynthetic bacteria [Gest, 1983]. During a standard exercise in a microbiology class, the enrichment of *Rhodospirillaceae* using the N_2-fixation procedure, the replacement of NH_4Cl with $(NH_4)_2SO_4$ was done. A green patch appeared in bottles after several weeks under light. Microscopical examination of the sample showed the presence of unusual bacteria, which was called after the sun and chloride (NH_4Cl) - *Heliobacterium chlorum* [Gest, 1983]. Later, *heliobacteriae* organisms were found mostly in soils, especially rice paddies [Romero, 1988].

Heliobacteria are strictly anaerobic gram-positive photosynthetic organisms [Woese, 1985]. Unlike green and purple bacteria, heliobacteria have no chlorosomes or intracytoplasmic membranes; all pigments are contained in the cytoplasmic membrane [Gest, 1983]. The heliobacterial reaction center (HbRC), where charge separation and electron transfer processes occur, is also located in the membrane.

The first characterization of the newly discovered bacteria was done by microscopic methods and absorption spectroscopy [Gest, 1983].

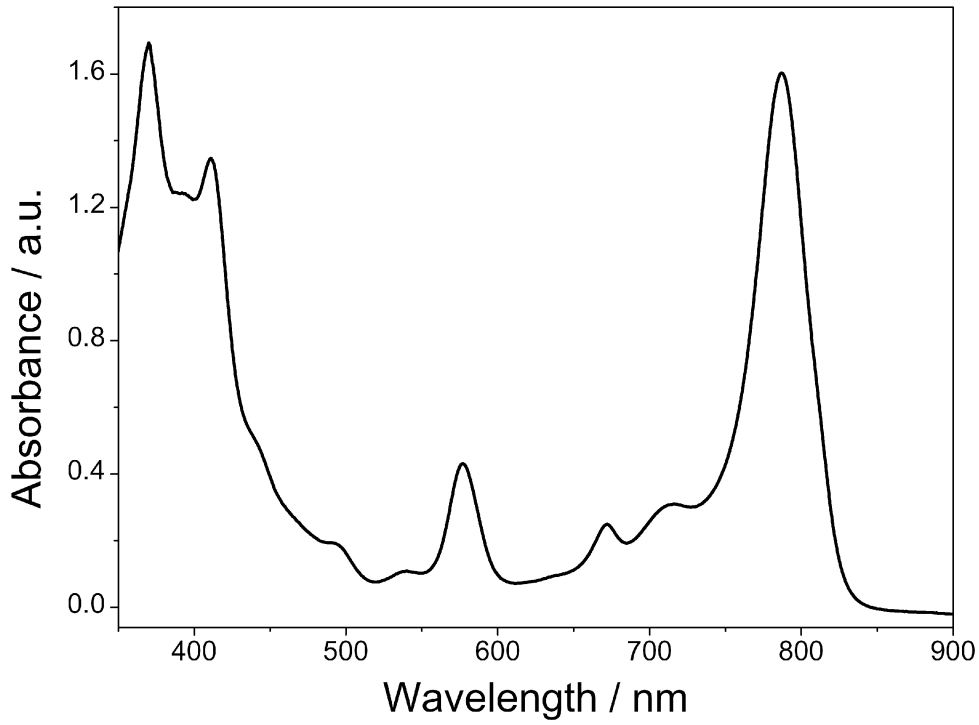

Figure 6.1 Absorption spectrum of untreated reaction centers of *Heliobacterium modesticaldum* in buffer solution (50 mM MOPS) at room temperature.

The absorption spectrum of HbRC shows an unusual maximum near 786 nm, indicating the presence of a new type of bacteriochlorophyll (Fig.6.1). This bacteriochlorophyll molecule was extracted and identified; it is called BChl *g* [Brockmann, 1983]. The molecular structure of the BChl *g* is shown in Fig.6.2*b*. The structure of BChl *g* is similar to BChl *b*, since both pigments contain an ethylidene group at ring II. Note that isomerization of BChl *g* at ring II under air in the darkness yields Chl a_F with farnesol tail [Kobayshi, 1998] (Fig 6.2*a*). It was proposed that BChl *g* may represent a stage in the evolution of Chl *a*.

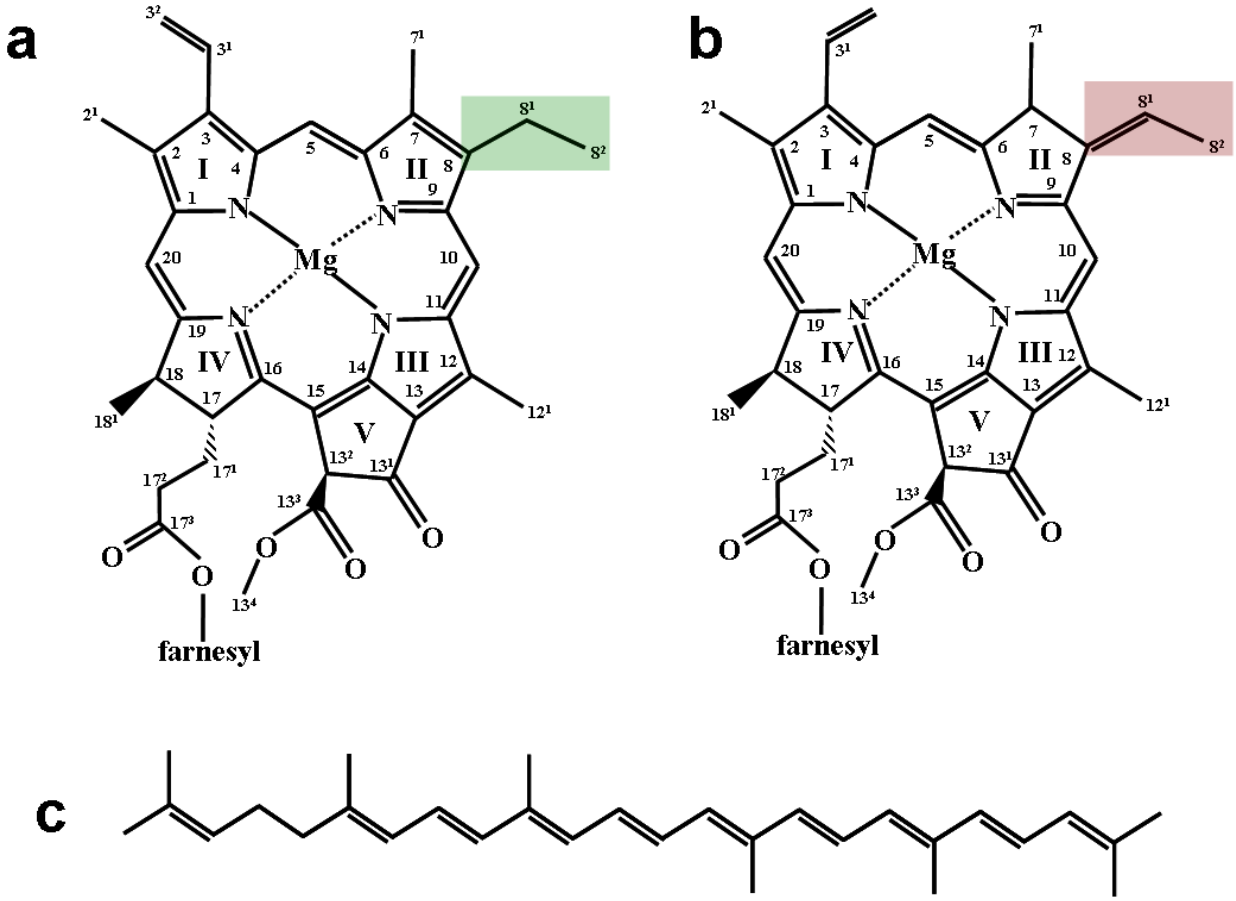

Figure 6.2 Structures of pigments which were found in HbRC. (*a*) Chl a_F, (*b*) BChl *g* and (c) carotenoid 4,4-diaponeurosporene.

The next step in the characterization of the heliobacteria using redox titrations and time-resolved optical spectroscopy was done in 1985 [Prince, 1985] It was found that HbRC contains 22 - 35 BChls *g* per RC [Prince, 1985], [Heinnickel, 2007]. The light-harvesting antenna complexes were found to be missing. Most of the BChl *g* molecules and two molecules of the carotenoid 4,4'-diaponeurosporene are directly bound to the reaction center, which is located in the cytoplasmic membrane [Trost, 1989] [van den Meent, 1990]. The carotenoid 4,4-diaponeurosporene is a C30 acyclic compound with nine conjugated double bonds and one

non-conjugated double bond [Takaichi, 1997]. It has been suggested that the small content of carotenoids in heliobacteria is the reason that why they are sensitive to oxygen [Gest, 1983].

HbRC is organized as a single homodimeric pigment–protein complex [Liebl, 1993] and classified as Type I reaction center because it contains as terminal acceptor a [4Fe-4S] cluster [Heinnickel, 2006]. A similar Type I homodimeric RC has been found in green sulfur bacteria *Chlorobiaceae*, for review see [Hauska, 2001]. Photosystem I (PS I) of cyanobacterial and higher plants is a well studied Type I RC and it can serve as a "model" system for the investigations of HbRC. It is assumed that the structure of the homodimeric HbRC is similar to the structure of the heterodimeric PS I of cyanobacteria. An X-ray crystal structure (2.5 Å) was determined for cyanobacterial PS I [Fromme, 2001]. In contrast to PS I, no crystallographic or other structural information is available for HbRC due to the high oxygen sensitivity of BChl *g*. However, several electron transfer (ET) cofactors of HbRC have been identified by biochemical and spectroscopic methods.

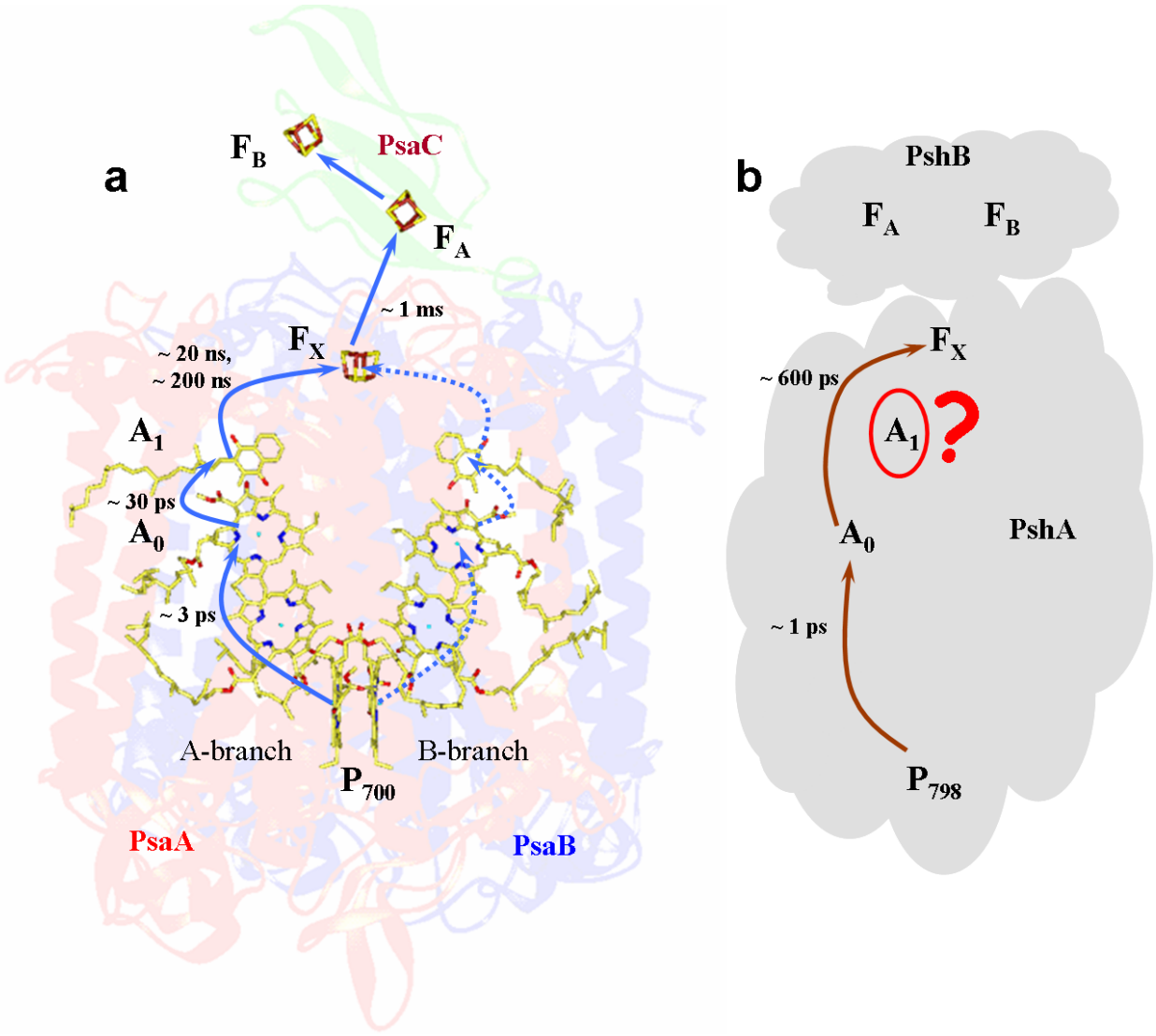

Figure 6.3 (*a*) ET cofactors in PS I as obtained from the X-ray structure of PsaA/PsaB and PsaC subunits (PDB entry 1JB0) [Fromme, 2001]. The ET pathways and corresponding rates measured at room temperature are shown [Brettel, 1997] [Joliot, 1999]. (*b*) The ET cofactors found in PshA and PshB subunits of HbRC and known ET rates are shown [Heinnickel, 2007].

HbRC contains the protein subunits PshA and PshB, for review see [Oh-oka, 2007] [Heinnickel, 2007]. The main ET cofactors are bound by the homodimeric PshA subunit, similar to the PsaA/PsaB subunits in PS I (Fig.6.3) [Liebl, 1993]. The HbRC primary electron donor P_{798} is a heterodimer of BChl *g* and *g'* [Prince, 1985] [Kobayshi, 1991] [Fisher, 1990]. Its redox

potential was estimated to be +225 mV [Prince, 1985]. Two chlorophyll *a*-like pigments 8^1-hydroxy-Chl a_F with farnesol tail act as electron acceptor A_0 [van den Meent, 1991]. HbRC contains a [4Fe-4S] cluster, which functions as the electron acceptor F_X as was shown in [Heinnickel, 2006] [Miyamoto, 2006]. Reduced F_X of the HbRC has a $S = 3/2$ ground state at low temperature, in contrast to PS I, where reduced F_X is a [4Fe-4S] cluster with a $S = 1/2$ ground spin state [Heinnickel, 2006]. The PshB subunit contains two terminal [4Fe-4S] clusters F_A and F_B. The PshB is assumed to be functionally similar to the PsaC subunit of PS I [Heinnickel, 2005]. It was previously found, by HPLC, that heliobacteria contain one molecule of 1,4-menaquinone-7 per RC [Trost, 1989] [Hiraishi, 1989] [Kjaer, 1998]. It was proposed that this quinone could serve as the intermediate acceptor A_1 by analogy to phylloquinone in PS I (Fig.6.3*a*). However, there is no clear spectroscopic evidence of participation of the quinone in the ET chain up to now. The crucial role of A_1 in ET processes in PS I was clarified by transient optical and EPR methods [Mathis, 1988] [Brettel, 1988] [Heathcote, 1996] [Zech, 1997]. Transient (or time-resolved) EPR technique will be used in this study to detect light-induced intermediate states in HbRC.

The time-resolved EPR (TREPR) method detects transient radical pairs (RP), which are created during ET in photosynthetic RC. The time resolution of the TREPR method is typically tens of nanoseconds. Thus, the light-induced EPR signals from RP can be detected when the lifetime of the RP is large enough [Pedersen, 1979] [Norris, 1990] [Kandrashkin, 1996]. Several light-induced spin-correlated RPs are detectable by TREPR in the case of PS I. During spin evolution in the ET process a spin-correlation in the RPs is generated. This leads in TREPR to a polarized spin-correlated RP. Spin polarization allows information to be obtained about the

transient states in the ET. In PS I these states are $P_{700}^{\bullet+}A_0^{\bullet-}$, $P_{700}^{\bullet+}A_1^{\bullet-}$ and $P_{700}^{\bullet+}F_X^{\bullet-}$. The TREPR spectrum of $P_{700}^{\bullet+}A_1^{\bullet-}$ in PS I can be detected directly [van der Est, 1997].

In the case of HbRC, spin-correlated radical pairs could not be detected by TREPR techniques [van der Est, 1998]. The EPR signal of $P_{798}^{\bullet+}$ in the terminal RP $P_{798}^{\bullet+}F_X^{\bullet-}$ has been observed [van der Est, 1998]. The contribution of F_X^- is not observable due to fast relaxation. Photovoltage and optical techniques have shown previously that the lifetime of $P^{\bullet+}A_0^{\bullet-}$ RP in HbRC is about 600 ps at room temperature [van Kan, 1989]. Thus, this RP cannot be detected by TREPR. The lifetime of the possible RP $P_{798}^{\bullet+}A_1^{\bullet-}$ is also shorter that the EPR time resolution, this state will, therefore, also not be detectable. The time limitation of the TREPR method could be overcome by increasing the lifetime of the $P_{798}^{\bullet+}A_1^{\bullet-}$ RP. Marcus theory of ET shows that the lifetime of RP can be prolonged by changing the redox potentials of ET cofactors [Marcus, 1985]. It was shown for PS I that substitution of the native phylloquinone in the A_1 binding site by an artificial quinone can shift the redox potential of the A_1 acceptor [Pushkar, 2005]. Thus, the quinone substitution in HbRC looks like a promising method to clarify the role of the quinone in the ET in HbRC.

The present work deals with the characterization of HbRC extracted from *Heliobacterium modesticaldum*. A variety of biochemical and multifrequency EPR spectroscopic techniques was used. The influences of the external conditions as well as chemical treatments of the HbRC were performed in order to clarify the role of the quinone in HbRC

6.2 Field dependence of spin-polarized signals in HbRC (X, Q and W-bands EPR measurements)

The detection sensitivity of thermally equilibrated radical transients is higher at W-band compared to X- and Q-band EPR due to the increase of the Boltzman population difference with increased magnetic field. Therefore, prior to the multifrequency TREPR investigation of the HbRC core sample (frozen solution, 100 K) was characterized by pulsed W-band EPR under continuous illumination at 690 nm. A dark-adapted sample of HbRC shows no detectable W-band EPR resonances prior to the illumination. Under illumination with a diode laser at 690 nm, an EPR signal appears that consists of one slightly asymmetrical line positioned around g ~ 2.0025, which is assigned to the $P_{798}^{\bullet+}$ radical cation. Simulations of the echo-detected and CW EPR lineshape yield the principal g-values [2.00307; 2.00249; 2.00224] for the $P_{798}^{\bullet+}$ radical (error ± $2 \cdot 10^{-5}$). These values are very close to those [2.00307; 2.00260; 2.00226] for the $P_{700}^{\bullet+}$ radical in PS I determined at 200 K by 325 GHz EPR [Bratt, 1997] and [2.00308; 2.00264; 2.00226] obtained from W-band spectra of photooxidized $P_{700}^{\bullet+}$ in deuterated PS I [Zech, 2000]. This supports a similar dimeric nature of donor cofactors in HbRC and PS I. In PS I, an additional signal is typically detected in the low-field region which is attributed to the intermediate electron acceptor $A_1^{\bullet-}$ [Savitsky, 2008]. There is no spectroscopic evidence for the presence of such quinone-like signal in the HbRC. A small signal of $P_{798}^{\bullet+}$ remains after switching off the laser. It is estimated that the overall amplitude of this remaining fraction is less than 10% of the overall amplitude. Thus, the 'cyclic' component of the photoinduced ET process is greater than 90%, which is much higher than the 25% reported in a previous EPR study [van der Est, 1998].

Transient X-band, Q-band, W-band EPR spectra of HbRC recorded 1 μs after the laser flash at 532 nm are shown in Fig. 6.4. The spectra display only features in the $P_{798}^{\bullet+}$ spectral region. The EPR signals exhibit an *E/A** polarization pattern (low field - emission, high field - enhanced absorption overlayed with the net polarization). The observed polarization pattern was found to stem from the singlet-triplet mixing process in the precursor radical pair when the contribution of only one of the partners in the subsequent radical pair is observed. Similar EPR spectra were previously recorded in HbRC, green sulphur bacteria [van der Est, 1998] and purple bacteria [Hulsebosch, 1999], [Morris, 1995], [Proskuryakov, 1993], [Tang, 1999] [Zech, 1998].

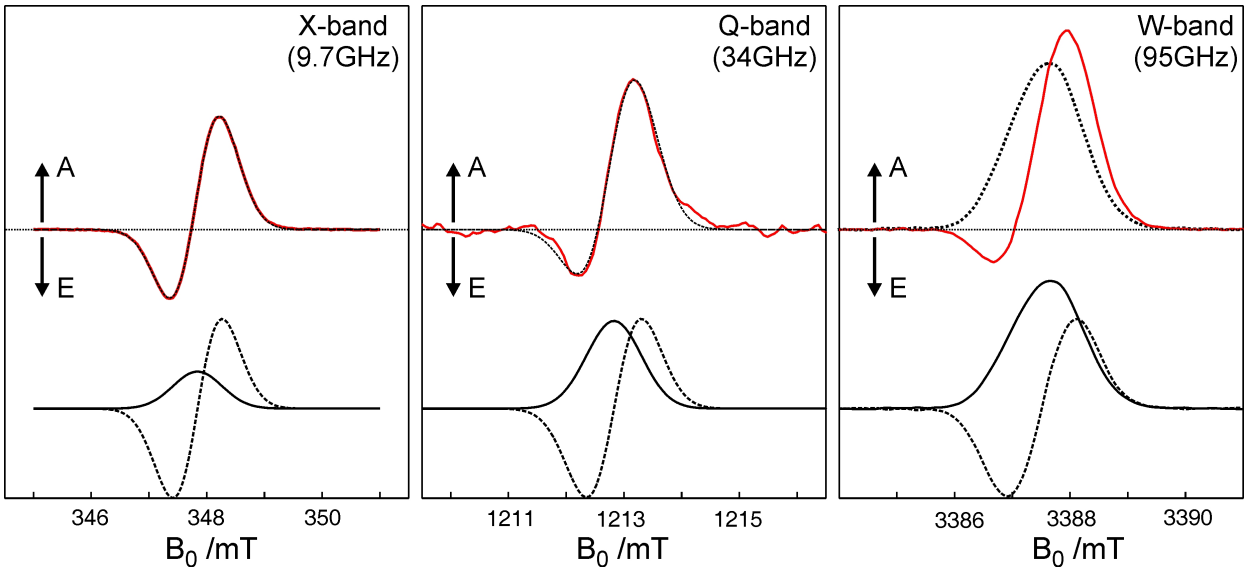

Figure 6.4 (Top) Experimental TREPR spectra (red curve) recorded 1 μs after the laser flash (532 nm) of HbRC sample at X-band (9.8 GHz, 80K), Q-band (34 GHz, 80K), W-band (95 GHz, 100K). Calculated spectra are indicated with black dotted curves. (Bottom) The net and multiplet polarization contributions obtained from experimental spectra are given by solid and dashed lines, respectively.

The exact treatment of polarization generated in sequential radical pairs is a rather complex task. This is because the spin system evolution in precursor radical pairs has to be calculated using a complete set of the magnetic and geometric parameters. However, it was shown that under the conditions that occur in photosynthetic reaction centers the polarization pattern of the given radical pair can be treated as a linear combination of the two contributions arising from the spin dynamics in the precursors [Kandrashkin, 1998].

The first contribution is a net polarization, *i.e.* purely absorptive or emissive, to each of the radicals in the subsequent RP. The net polarization of the two radicals is equal and opposite. The strength of the polarization can be approximated by:

$$P_N = \frac{q \cdot b}{q^2 + b^2 + k^2} \qquad \text{(Eq.6.1).}$$

The difference of the Larmor frequencies of the donor (D) and acceptor (A) spins in the pair $q = \omega_D - \omega_A = \frac{[g_D - g_A] \cdot \mu_B \cdot B_0}{\hbar}$ can be written as $q = \frac{\Delta g}{g_e} \cdot \omega_0$, where ω_0 is the EPR spectrometer frequency in angular frequency units. The flip-flop term in angular frequency units of the spin is given by $b = 2J+d$ with dipolar coupling d. The isotropic exchange interaction, $2J$, is defined as the energy difference between the singlet and triplet states E(S)-E(T_0). The decay rate for the precursor RP is noted by k.

In addition to the net polarization, singlet-triplet mixing also causes multiplet polarization (an antiphase doublet pattern with overall integrated intensity equal to zero) of the donor because of inhomogeneous broadening from unresolved hyperfine couplings. The multiplet polarization is proportional to

$$P_M \propto \frac{b \cdot \Delta}{q^2 + b^2 + k^2} \qquad \text{(Eq.6.2)}$$

where Δ is the half-width of the Gaussian line shape describing inhomogeneous broadening of the donor EPR line.

An analysis of the $P_{798}^{\bullet+}$ polarization offers the opportunity to clarify the nature of the precursor radical pair. In previously reported EPR investigation of HbRC at X-band and K-band (24 GHz), the analysis of $P_{798}^{\bullet+}$ polarization was performed using a direct fit of the observed EPR signals to theoretically predicted lineshapes without a knowledge of the absolute polarization values [van der Est, 1998], [Kandrashkin, 1998], [Kandrashkin, 2002]. The W-band EPR experiments, however, allowed the absolute polarization to be measured [Möbius, 2009]. To obtain the value of the net contribution in terms of the population difference of the electron Zeeman levels, the W-band EPR spectrum of $P_{798}^{\bullet+}$, after spin-lattice relaxation of the initial polarization by T_1 (about 140 μs at 100 K), was recorded 500 μs after the laser flash (Fig. 6.4). After scaling the net contribution to the thermally equilibrated spectrum, and after taking into account the equilibrium population difference at 100 K and 3.4 T (95 GHz) of $2.3 \cdot 10^{-2}$, a net contribution of $P_N = (1.8 \pm 0.1) \cdot 10^{-2}$ was obtained.

In the first step of the analysis it was assumed that polarization is generated in the short lived $P_{798}^{\bullet+}A_0^{\bullet-}$ radical pair as a precursor to $P_{798}^{\bullet+}F_X^{\bullet-}$. The mean decay rate of the precursor radical pair was taken to be about $10^9\ s^{-1}$ consistent with previously reported data [Lin, 1995], [Brettel, 2001], [Kleinherenbrink, 1994]. The spin-spin coupling term *b* was assumed to be dominated by the exchange interaction which is taken to be positive in order to explain *A* net and *E/A* multiplet patterns [Kandrashkin, 1998]. The averaged $P_{798}^{\bullet+}$ g-value of 2.0026 was calculated from the

values given above. The $A_0^{\bullet-}$ g-value of 2.0028 was estimated from previously reported EPR investigations [Bratt, 2000], [Un, 2001] on Chl $a^{\bullet-}$ yielding $\Delta g = \left[g(P_{798}^{\bullet+}) - g(A_0^{\bullet-})\right] \sim 2 \cdot 10^{-4}$. This suggests $q << k$ at W-band. The q-term reaches the highest value at W-band frequencies due to the linear frequency dependence.

The Eq.6.1 can be rewritten in form of the quadratic equation for b, which roots are given by:

$$b = \frac{q}{2P_N} \pm \sqrt{\left(\frac{q}{2P_N}\right)^2 - k^2} \qquad \text{(Eq.6.3).}$$

In order to obtain the real solution for b, the condition $k < q/2P$ has to be fulfilled. Substituting the values from the estimates above, one obtains $k < 1.8 \cdot 10^9$ s^{-1}. Thus, the analysis of net polarization leads to the estimate $\tau > 550$ ps for the lifetime of the $P_{798}^{\bullet+}A_0^{\bullet-}$ radical pair, which agrees with results from optical measurements. For $\tau = 550$ ps, a b-value of +10.0 mT is calculated from Eq.6.3. This value is, however, unrealistically large. However, it can be easily reduced assuming slightly larger τ values in Eq.6.3. Thus, for $\tau = 800$ ps and 1 ns spin-spin coupling values $b = 2 \cdot J + d$ of +3.0 mT and +1.8 mT are obtained. These values are already comparable with that reported for the primary radical pair $P_{865}^{\bullet+}BPhe^{\bullet-}$ (BPhe - bacteriopheophytin acceptor) in the bacterial reaction centers [Proskuryakov, 1996], [Till, 1997], [Hulsebosch, 1999], [Hulsebosch, 2001].

Due to uncertainty of the magnetic and geometric parameters of the $P_{798}^{\bullet+}A_0^{\bullet-}$ pair, it is difficult to analyse in detail the multiplet polarization contribution. However, taking into account that $q << k$, it can be shown that the multiplet polarization contribution does not depend on the

microwave frequency, see Eq.6.2. Thus, the multiplet signal can be used to obtain the net polarizations at X- and Q-band. Fig. 6.4 (bottom) shows the experimentally recorded spectra decomposed into net and multiplet polarization contributions. The decomposition was performed for the fitting experimental EPR spectrum to the calculated $P_{798}^{\bullet+}$ EPR absorption using the magnetic parameters extracted from the W-band EPR spectrum of thermally equilibrated $P_{798}^{\bullet+}$ to obtain the zero overall integrated intensity of the residual. The net polarization increases from X- to W-band as expected. The increase of the net polarization with increasing magnetic field was already observed in the bacterial reaction center in which the life time of the primary radical pair $P_{865}^{\bullet+}BPhe^{\bullet-}$ was prolonged from the native 200 ps to up to several nanoseconds either by the substitution of the native quinone acceptor $Q_A^{\bullet-}$ with the different quinone type or by chemical manipulations [Hulsebosch, 1999], [Tang, 1999], [Morris, 1995]. Fig. 6.5 shows the frequency dependence of the net polarization calculated assuming a constant multiplet contribution. The solid line shows the dependence calculated by Eq.6.1 using the parameters obtained from the analysis of the W-band net polarization. The X- and Q-band values deviate from the linear prediction. This deviation, however, is possibly explained by the g-tensor anisotropy which influences the W-band EPR spectrum but is not included in the theoretical model [Kandrashkin, 1998], *i.e.* Eq.6.1.

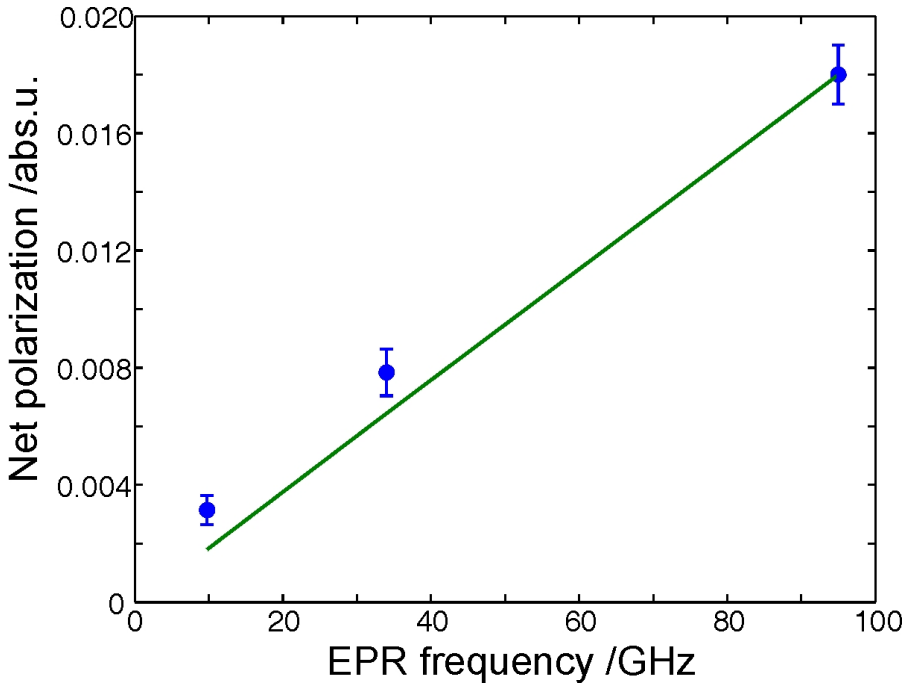

Figure 6.5 The experimental net polarization contribution (in populations difference) as function of the EPR frequency and theoretically predicted dependence (solid line) calculated using Eq.6.1 with $\Delta g = 2 \cdot 10^{-4}$, τ = 800ps and $2J+d = 3mT$.

Thus, the frequency dependence of the $P_{798}^{\bullet+}$ polarization can be satisfactory explained to be generated in the $P_{798}^{\bullet+}A_0^{\bullet-}$ radical pair. This, however, does not necessary mean that the quinone participates in the ET chain.

6.3 Samples from different purification stages

There are several biochemical factors, which have to be excluded, before a conclusion about the A_1 role can be reached. It was proposed that the quinone bound to the RC could be lost during the purification of HbRC or that the reaction center could be damaged afterwards. It was

shown above that the polarization pattern of $P_{798}^{\bullet+}$ is strongly influenced by the lifetime of the intermediate RP. Therefore, four different types of HbRC samples were compared by means of X-band TREPR. These samples were prepared at different purification stages of heliobacteria: i) cells of *Heliobacterium modesticaldum*, ii) membranes, iii) cells lysate and iv) purified HbRC. X-band TREPR spectra detected 1 µs after laser flash at 532 nm are shown at Fig.6.6. All spectra are similar and show the EPR contribution due to $P_{798}^{\bullet+}$ in the radical pair of $P_{798}^{\bullet+}F_X^{\bullet-}$ [van der Est, 1998]. A damage of the RC during purification can thus be excluded to a large extend due to identical EPR activity of all samples.

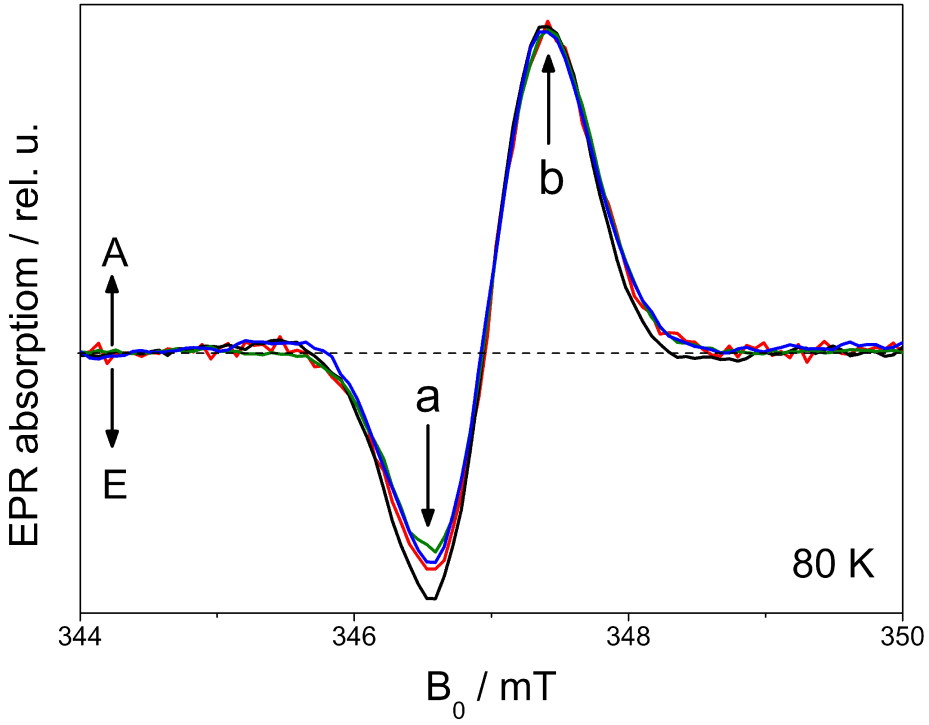

Figure 6.6 X-band TREPR spectra of HbRC recorded 1µs after the laser flash (532 nm) at 80 K of the four different purification stages: whole cells (red line), membranes (black line), cells lysate (green line) and purified HbRC (blue line).

The decay profiles of the EPR signals were also found to be similar for all purification stages (Fig.6.7). The analysis of the decays shows that they fit to one exponential with a decay time of about 9 ± 0.1 μs. Thus, the spin relaxation of the primary donor P_{798} as well as possible contributions from electron recombination processes does not change upon purification of the HbRC.

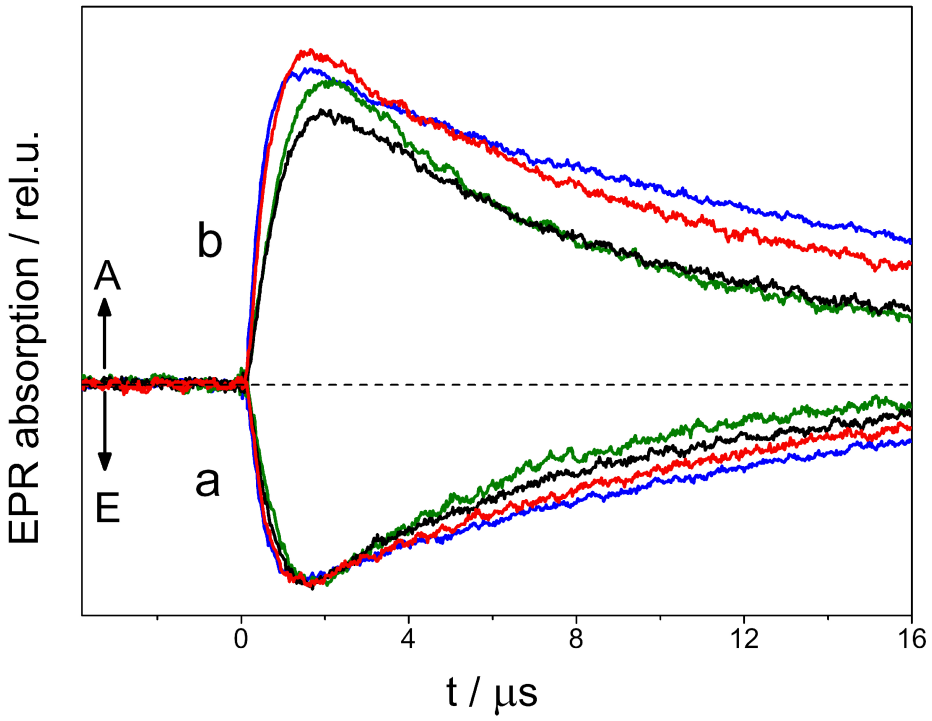

Figure 6.7 Decay profiles of the EPR signals of HbRC recorded at 80 K of the four different purification stages: whole cells (red line), membranes (black line), cells lysate (green line) and purified HbRC (blue line). Decays were recorded at spectral positions (a and b) which are indicated with arrows at Fig.6.6.

Thus if the quinone participates in the ET in HbRC, it is not lost during the purification. However, if the quinone does not participate in the ET, it remains unclear if it is retained at all preparation steps, because in this instance it would not be detected by EPR.

As the samples from different preparation steps gave the same results only purified reaction centers of *Heliobacterium modesticaldum* were used for further experiments. In these reaction centers the PshB subunit, which contains iron-sulfur clusters F_A and F_B is removed, but the crucial ET cofactors P_{798}, A_0, (A_1 ?), F_X should be retained.

6.4 Proof of the quinone participation in the ET: chemical treatments

The direct TREPR detection of $P_{798}^{\bullet+}A_1^{\bullet-}$ RP is impossible because ET rate is too fast in the native HbRC. However, the same set of chemical treatments as used for PS I for slowing down the ET rate between the A_1 and the F_X acceptors should allow trapping of these transient state. In the following part of this work these procedures are used for the HbRC.

6.4.1 Quinone replacement

The amino acid sequence of the PshA subunit of HbRC shows a high degree (ca 50%) of similarity with the PS I PsaA/PsaB subunits in the region around the P_{700} and at the putative A_1 binding sites [Heinnickel, 2007]. The participation of a quinone type acceptor in the ET chain of HbRC is therefore expected. Furthermore, the presence of 1-2 menaquinone-7 molecules per HbRC was detected by HPLC [Hiraishi, 1989] [Kjaer, 1998]. Thus, the ET chain structure of HbRC, *i.e.* cofactor and distances between them is supposed to be similar to the ET chain of PS I. However, TREPR measurements on HbRC are not able to detect the spin-polarized signal from a

transient RP $P_{798}^{\bullet+}A_1^{\bullet-}$. One possibility, which explains the TREPR results, is that the lifetime of $P_{798}^{\bullet+}A_1^{\bullet-}$ is too short to be detected. An attempt to replace the quinone in the putative binding site of A_1 in HbRC was done in analogy to the quinone replacement procedure in PS I [Pushkar, 2005]. Shifting of the redox potential of the quinone can change the ET rate between A_1 and F_X intermediates. The successful quinone substitution can bring the ET rate in HbRC into the TREPR accessible time range. The following quinones were used here: 2-methyl-1,4-naphthoquinone (vitamin K_3, VK_3; 2 rings), tetramethyl-1,4-benzoquinone (duroquinone; DQ, 1 ring) and 9,10-dioxoanthracene (anthraquinone; AQ, 3 rings) (Fig.6.8). The vitamin K_3 was selected for the replacement, because it is structurally similar to the menaquinone, the native HbRC quinone.

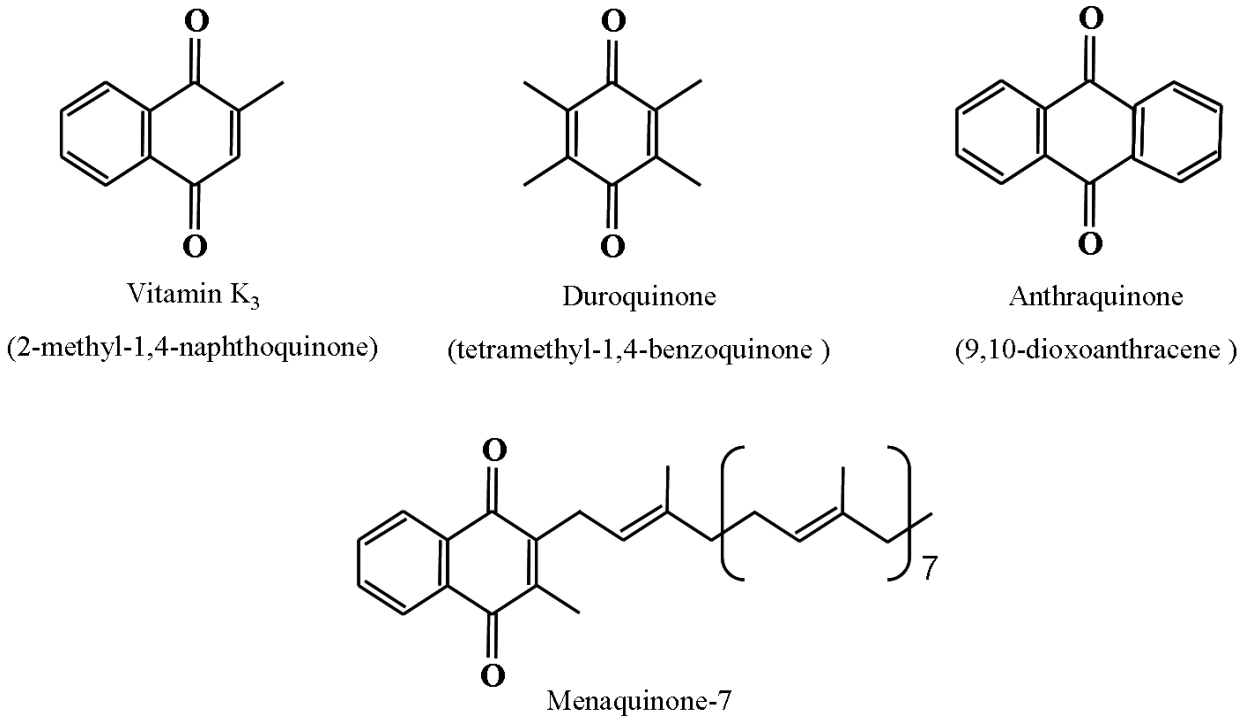

Figure 6.8 Structures of the quinones (vitamin K_3, duroquinone, anthraquinone) used for the replacement and possible native quinone (menaquinone-7) of HbRC.

The redox potentials (E_M) of these quinones in solution are known. The E_M ($Q/Q^{\bullet-}$) *vs*. saturated calomel electrode are -0.66 V, -0.76 V and -0.90 V in dimethylformamide at 25 °C for vitamin K_3, duroquinone and anthraquinone, respectively [Chambers, 1974]. It was previously shown that duroquinone substitution in PS I increases the redox potential of the A_1 acceptor, *i.e.* slowing the ET rate from A_1 to F_X. In contrast, the anthraquinone substitution decreases the redox potential of A_1, *i.e.* accelerating the ET rate [Pushkar, 2005] [Itoh, 2001]. Vitamin K_3 does not change the ET rate as compared to native PS I phylloquinone (vitamin K_1). Note, however, that the transient RP $P_{700}^{\bullet+}A_1^{\bullet-}$ in PS I can be directly detected by TREPR. The detailed description of the quinone replacement procedure in HbRC is given in Chapter 4.

The TREPR spectra of HbRC after the quinone replacement treatment are shown in Fig.6.9. The polarization pattern was found to be independent of the quinone used. All spectra are very similar to spectrum of the untreated HbRC (black line) and show only the EPR contribution of $P_{798}^{\bullet+}$ in the radical pair $P_{798}^{\bullet+}F_X^{\bullet-}$ [van der Est, 1998].

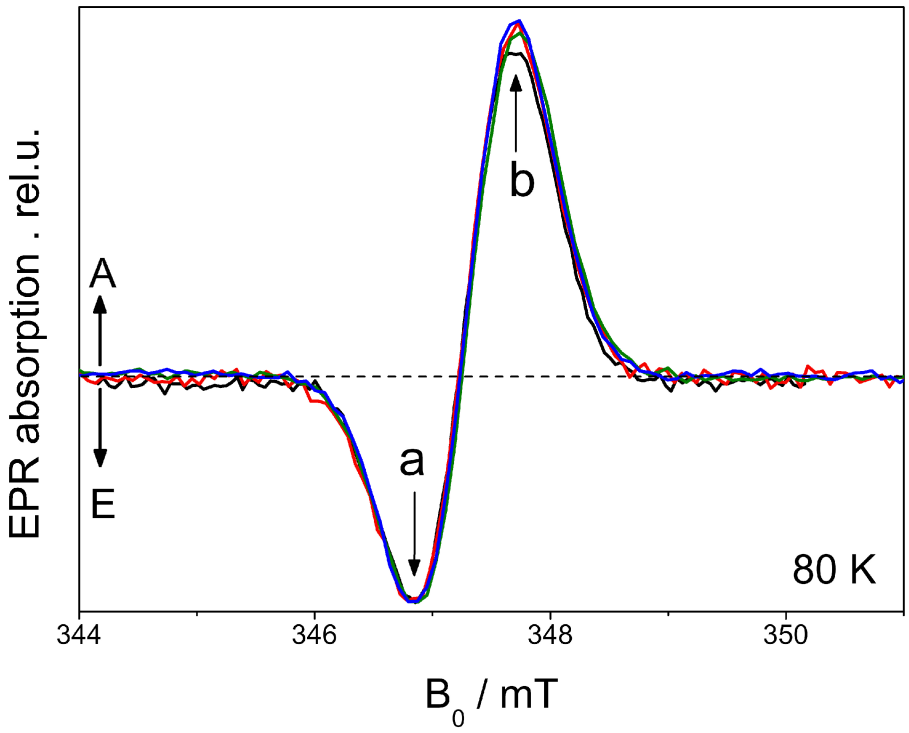

Figure 6.9 X-band TREPR spectra recorded 1µs after the laser flash (532 nm) at 80 K after the quinone replacement treatment of HbRC by vitamin K_3 (VK_3, red line), duroquinone (DQ, green line) and anthraquinone (AQ, blue line) and untreated HbRC (black line). Transients positions are indicated with arrows *a* and *b* (see Fig.6.10)

The EPR kinetics of $P_{798}^{\bullet+}$ polarization after quinone replacement in HbRC generally show slightly faster decay rates (Fig.6.10). This can, however, be explained by the presence of the ethanol stemming from the quinone replacement procedure.

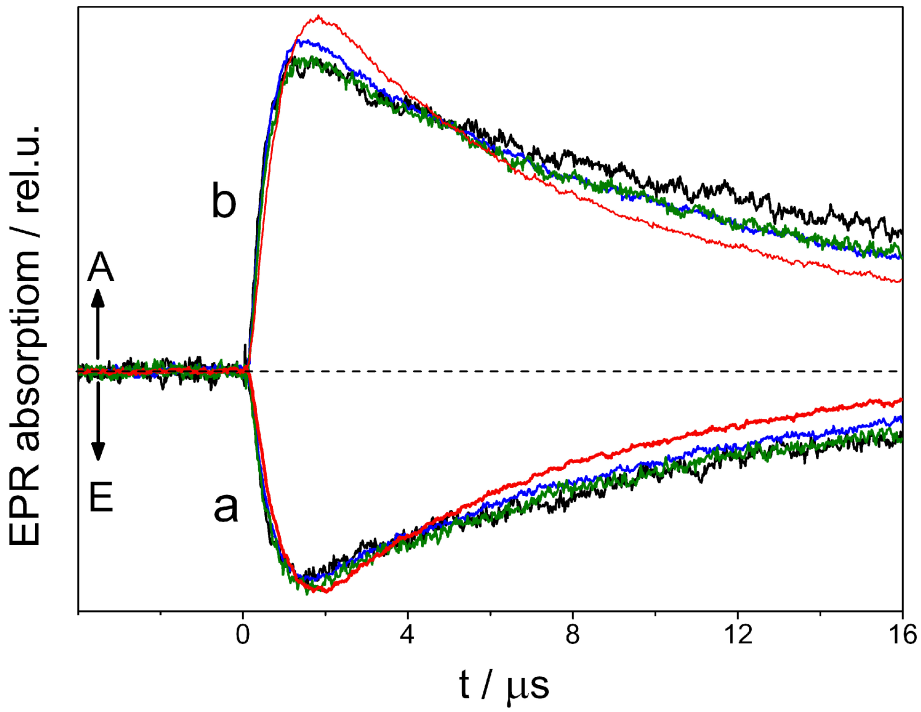

Figure 6.10 TREPR decay profiles of the $P_{798}^{\bullet+}$ signal after the quinone replacement treatment of HbRC by vitamin K_3 (VK_3, red line), duroquinone (DQ, green line) and anthraquinone (AQ, blue line) and untreated HbRC (black line). The kinetics were recorded at two field positions (a, b), which are indicated by arrows in Fig.6.9, for corresponding lines see Fig.6.9.

Thus, the following conclusion was drawn: if the quinone participates in ET in HbRC, then the quinone can not be replaced by the procedure used. However, if the quinone does not participate in ET, then the EPR signals are expected to be independent of the type of quinone incorporated into the HbRC.

6.4.2 F_X removal

It was previously shown that it is possible to remove the terminal acceptor F_X from PS I [Golbeck, 1982]. Such an F_X lacking PS I complex is still ET active, using the terminal acceptor A_1. Thus, F_X removal at the HbRC may allow detection of the accumulated $A_1^{\bullet-}$ radical either directly or indirectly as changes in EPR spectrum.

Unfortunately, it was found that during the F_X removal procedure in HbRC, which uses the oxidant potassium ferricyanide, the conversion (oxidation) of BChl *g* to Chl *a* takes place. Consequently, a significant part of reaction centers lost their ability for charge separation (see section *6.6*). The TREPR spectrum of the HbRC sample subjected to the procedure for the F_X removal shows a negligible signal from the spin-polarized $P_{798}^{\bullet+}$ (data not shown). An intensive EPR signal resulting from a triplet state was observed. Its polarization pattern and zero-field splitting parameters correspond to a Chl *a* triplet species generated by the intersystem crossing mechanism, which is characteristic for energy transfer in the "antenna" system of HbRC. This result correlates with the observation of a triplet Chl *a* spectrum in HbRC samples converted by air (see section *6.5*). In summary, the procedure for removal of the terminal acceptor F_X was found to be destructive for the HbRC, due to conversion of BChl *g* to Chl *a* and subsequent loss of the activity.

6.4.3 Investigation of the photoaccumulated radicals in HbRC

Previous investigations in PS I have demonstrated that it is possible to generate significant concentration of the $A_1^{\bullet-}$ radical by photoaccumulation procedure [Heathcote, 1996]. Therefore, two sets of photoaccumulated HbRC samples were prepared: i) with sodium ascorbate ($C_6H_7NaO_6$) and ii) with sodium dithionite ($Na_2S_2O_4$). Sodium ascorbate was added to continuously reduce the $P_{798}^{\bullet+}$ state of the donor during illumination. It should result in accumulation of stationary concentration of all acceptor radicals along the ET chain. Sodium dithionite is used for reduction of the iron-sulfur clusters. The continuous illumination of the dithionite-treated RC can lead to the saturation of the ET chain by electrons and, therefore, result in accumulation of the stationary cofactor radicals.

The TREPR spectrum of the ascorbate-reduced photoaccumulated sample is identical to untreated HbRC (data not shown). The CW EPR spectra of dark-frozen ascorbate photoaccumulated HbRC samples at X- and W-band do not provide any indication of additional radicals. A surprising result was obtained with the dithionite-reduced sample. The TREPR spectrum of the dithionite-reduced photoaccumulated HbRC sample is shown at Fig.6.11 at early and at late times after the laser flash. The spectrum recorded 1 μs after the flash appears with polarization pattern *A/E*, in contrast to the *E/A* pattern observed for untreated HbRC. This signal probably originates from species different from $P_{798}^{\bullet+}$. However, the detected signal is superimposed by a large triplet signal that it is generated only in a minority of the HbRCs. The TREPR spectra of the photoaccumulated HbRC do not allow to make any conclusions regarding the nature of this newly polarized signal.

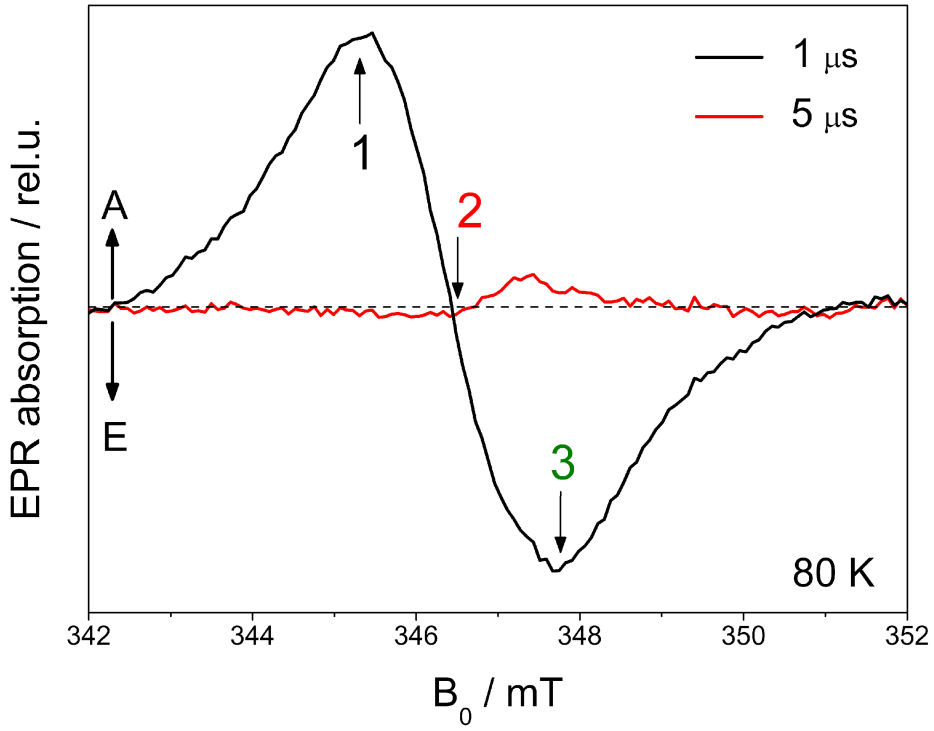

Figure 6.11 X-band TREPR spectra of dithionite reduced HbRC recorded 1μs (black line) and 5μs (red line) after the laser flash (532 nm) at 80 K.

At late time (5μs after laser flash) the spectrum appears with *E/A* polarization. This late signal probably comes from HbRCs, which do not interact with the sodium dithionite. The polarization pattern and EPR signal decays (Fig.6.12) are similar to the ones of the untreated HbRC.

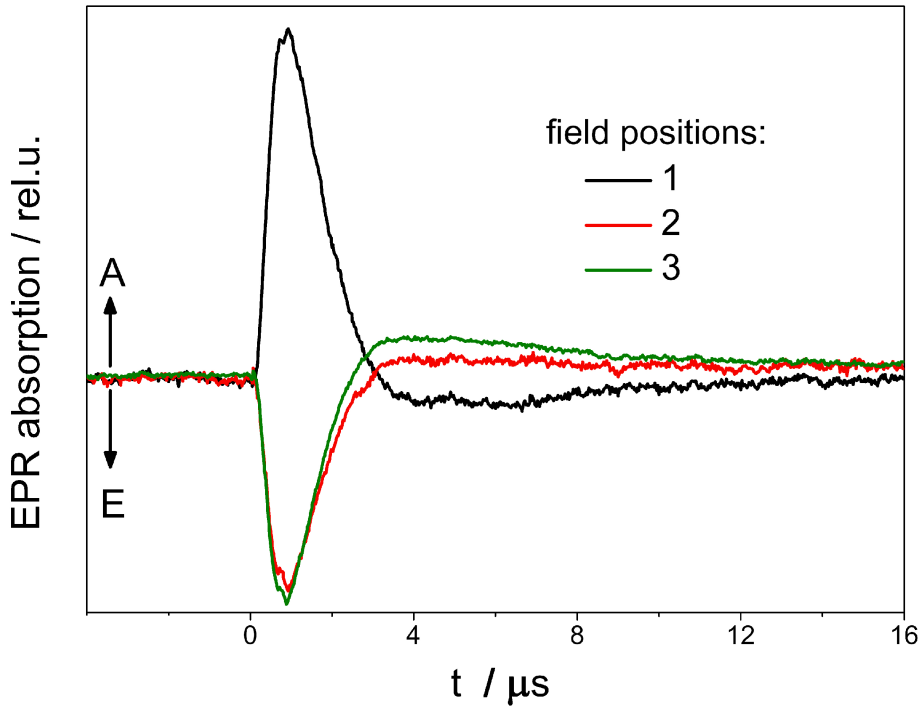

Figure 6.12 TREPR decay profiles of $P_{798}^{\bullet+}$ signal in dithionite reduced HbRC are shown. Kinetics at three field positions (1, 2, 3) were recorded, which are indicated by arrows in Fig.6.11.

The triplet spectrum in the dithionite-reduced HbRC is the same as in the untreated HbRC (Fig.6.15*a*, red line). This indicates that the sodium dithionite does not alter the structure of the BChl *g* and/or other ET cofactors, respectively (see next section *6.5*).

Thus, the procedure of photoaccumulation with sodium dithionite does not allow to accumulate a stationary radical $A_1^{\bullet-}$. Only a minor part of HbRC under the sodium dithionite and illumination show the cyclic ET and significant amounts of HbRC create triplet states.

6.5 Triplets in HbRC

Many photochemical reactions proceed through the formation of the excited triplet states. Excited triplet molecules in solution generally have short lifetimes so that their stationary concentration is low. However, the EPR sensitivity may be enhanced due to the initial spin polarization of these triples molecules. Triplets appear as result of intermolecular transitions from the excited singlet state. The singlet-triplet transition is spin forbidden; however, this transition occurs due to spin-orbit coupling, which mixes the S and T states. S-T_0 transitions are spin-selective and the triplet states appear with polarized spins [Pedersen, 1975]. There are several mechanisms for the formation of polarized triples states known.

After light excitation of HbRC triplets can be detected by TREPR. The difference in the polarization pattern as well as zero-field splitting (ZFS) parameters |D| and |E| allow to be characterized and the process by which they were formed, to be identified.

Fig.6.13 shows triplet spectra of HbRC at different times after laser excitation. Shortly after the laser flash (1 μs) the triplet spectrum shows the polarization pattern *eeeaaa* (*e* – emission, *a* - absorption) (Fig.6.13, black line). This polarization pattern is characteristic for a triplet state formed by the intersystem crossing (ISC) mechanism [Levanon, 1978].

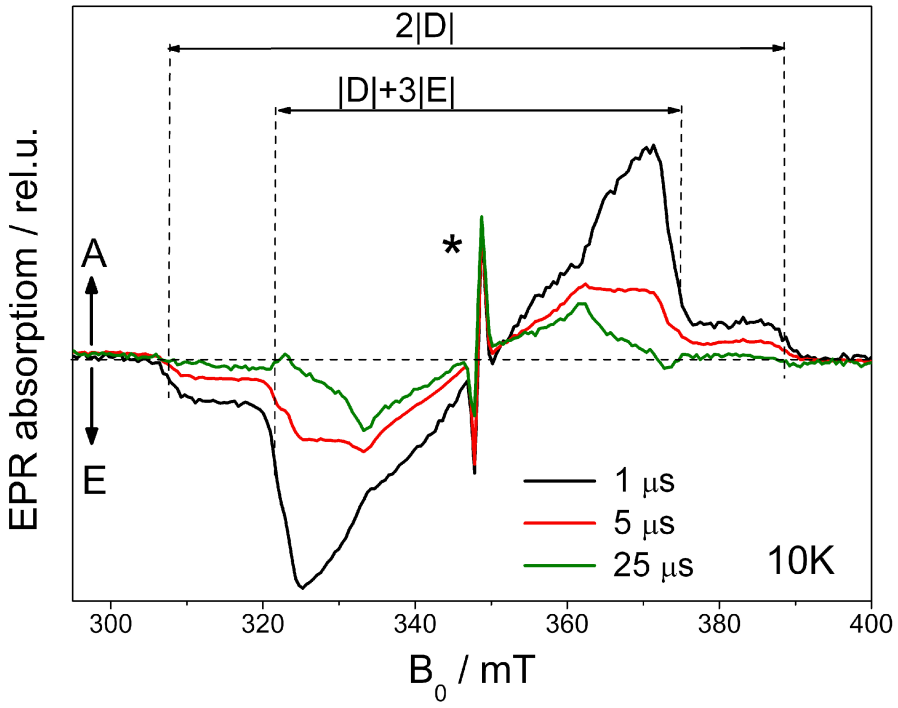

Figure 6.13 X-band TREPR triplet spectra recorded 1μs (black line), 5 μs (red line) and 25 μs (green line) after the laser flash (532 nm) at 10 K. The signal marked (*) at center field is assigned to the spin-polarized signal of $P_{798}^{\bullet+}$ (see Fig.6.5).

After intensive illumination of HbRC, excess light can excite the surrounding "antenna" BChl *g* molecules. During *intersystem crossing* (ISC) processes, the excited singlet state of "antenna" BChl *g* non-radiatively proceeds to the excited triplet state that is spin-polarized (Fig.1.2, *b*). The probability of flipping of the excited electron increases when the vibrational levels of the two excited states overlap. ISC usually is characteristic for molecules with "heavy" atom, because the spin-orbit interaction in such molecules is large [Budil, 1991].

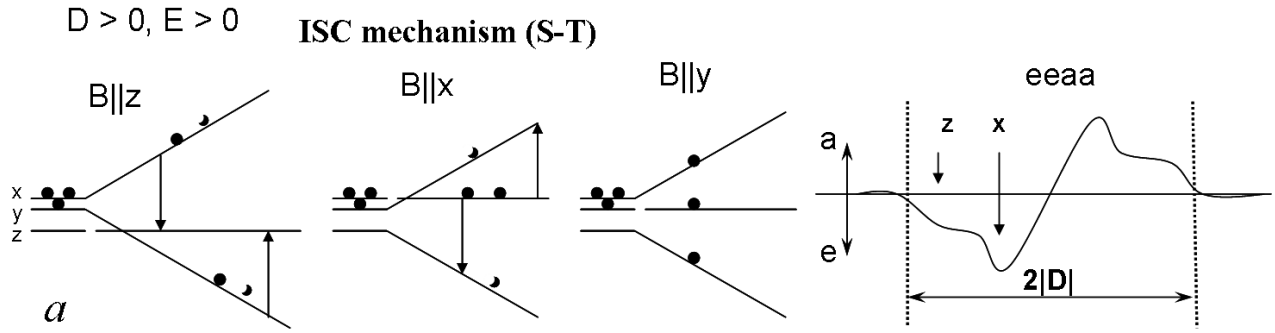

Figure 6.14 Formation of polarized triples state by the intersystem crossing (ISC) mechanism in a system with positive ZFS parameters (D > 0, E > 0). The expected polarization pattern of EPR spectrum is presented.

In general, ISC is highly selective with respect to the three spin sublevel predominantly populating only a single level or a pair of levels in significant excess to the remaining levels or level [Levanon, 1978]. Due to this selective population of triplet sublevels of BChl *g* with polarization pattern *eeaa* is appear (Fig. 6.14).

The population of the BChl *g* triplet sublevels transfers by the triplet-triplet mechanism [Levanon, 1978] [Cogdell, 1987] to the triplet sublevels of the carotenoid 4,4'-diaponeurosporene, which is located close to the surrounding "antenna" BChl *g* molecules. The observed polarization pattern of the carotenoid triplet corresponds to the polarization pattern of "antenna" BChl *g*. Such triplet-triplet quenching processes, by the carotenoid, serves as a protection mechanism for the RC from excess energy, like in many other photosynthetic organisms [Bittl, 2001] [Vrieze, 1998] [Cohen, 2004] [Frank, 1996]. The triplet levels of Car molecules are lower than the triplet levels of antenna Chl *a*. The energy transfer occurs by the following scheme:

$$^{1}\text{Car} + {}^{3}\text{Chl } a^{*} \rightarrow {}^{3}\text{Car}^{*} + {}^{1}\text{Chl } a$$

and prevents the formation of destructive singlet-state oxygen radicals [Cogdell, 1987]:

$$^3O_2 + {}^3\text{Chl } a^* \rightarrow {}^1O_2^* + {}^1\text{Chl } a.$$

The ZFS parameters determined from the simulation of the TREPR spectrum recorded 1 µs after the laser flash (Fig.6.15) (|D| = 40.5 ± 1 mT, |E| = 3.8 ± 0.6 mT; populations of the triplet sublevels p_X = 0.4, p_Y = 1.1, p_Z = 0.67) agree with previously reported values for the carotenoid neurosporene in the light-harvesting complexes of purple bacteria *Rb. sphaeroides* (|D| = 39.3 mT, |E| = 3.8 mT) [Bittl, 2001]. This result confirms the presence and function of the carotenoid neurosporene in the HbRC [Amesz, 1995] [Kobayashi, 1998]. At the later time, after the laser flash (Fig.6.15, 25 µs), the triplet spectrum is different. The ZFS parameters |D| = 40.5 ± 1 mT, |E| = 3.8 ± 0.6 mT corresponds to a triplet carotenoid. Here the polarization pattern is *eaeaea* and the population of the triplet sublevels are p_X = 0.2, p_Y = 0.15, p_Z = 0.8. The change in the polarization pattern of the carotenoid triplet occurs due to spin evolution in the x and y sublevels.

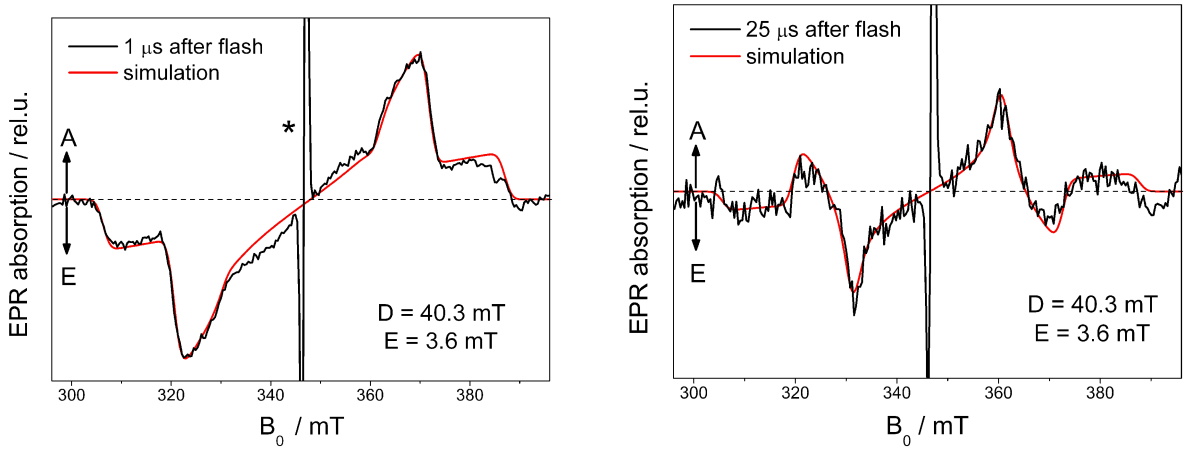

Figure 6.15 X-band TREPR triplet spectra of untreated HbRC 1 and 25 µs after laser flash (black lines) at 80 K and simulated triplet spectra (red lines) at 80 K. The signal marked (*) in the center field assigned to the EPR signal of $P_{798}^{\bullet+}$.

The results of the TREPR study of different preparations of HbRC show the influence of the biochemical treatment on the triplet spectra. A triplet spectrum with ZFS parameters |D| = 29.5 mT and |E| = 2.3 mT of Ch *a*, (Fig.6.16*b*, green line) was observed after air conversion of BChl *g* to Chl *a* in HbRC. The ZFS parameters are comparable with ZFS values of the Chl *a* triplet in organic solvent obtained previously: |D| = 29.3 and |E| = 4.3 mT [Thurnauer, 1977]. The triplet spectrum of the oxygen converted HbRC does not change during the detection time. The *eeeaaa* polarization pattern of the spectrum is typical for a triplet which is formed by the ISC mechanism. Charge separation does not take place in air converted HbRC.

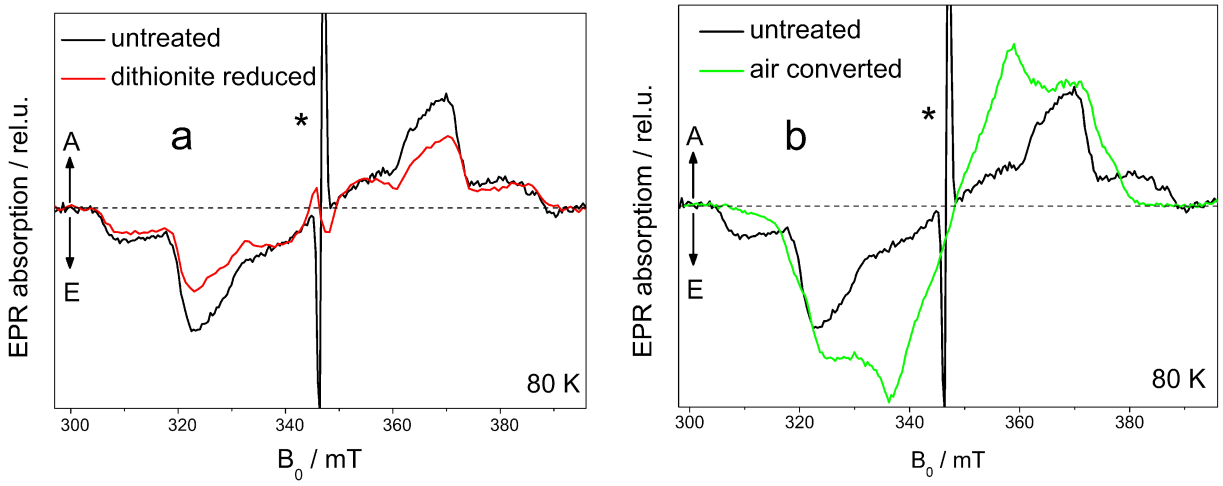

Figure 6.16 (*a*) X-band TREPR triplet spectra of untreated HbRC (black line), dithionite reduced HbRC (red line). (*b*) X-band TREPR triplet spectra of untreated HbRC (black line) and HbRC after oxidation by air (green line). Spectra recorded 1μs after the laser flash (532 nm) at 80 K. The signal marked (*) in the center field assigned to the EPR signal of $P_{798}^{\bullet+}$.

Thus, all triplets are formed by the ISC mechanism. The absence of the carotenoid triplet spectrum could be explained by differences in energy levels of triplets of Chl *a* and BChl *g*. If energy levels of the triplet corresponding to Chl *a* are close to the triplet levels of carotenoid or

located above it, triplet-triplet quenching via carotenoid will be either slower than the relaxation processes or potentially blocked.

6.6 Oxygen sensitivity of HbRC (BChl g *conversion to Chl* a*)*

It was previously shown that upon interaction with oxygen the extracted BChl *g* molecule is converted into Chl *a* in 80 % v/v acetone solution [Kobayashi, 1998]. The same conversion was observed in purified HbRC under oxygenic conditions (oxygen or other oxidant) [Romero, 1988]. The characteristic absorption peaks of BChl *g* (786 nm) and Chl *a* (670 nm) were used to trace the conversion process. The UV/Vis absorption spectra of HbRC in buffer solution under anaerobic (black line) and aerobic conditions (red line) are shown in Fig.6.17. The HbRC absorption spectrum under anaerobic conditions reveals the absorption bands at 369 nm, 407 nm, 576 nm, 670 nm and 710-800 nm, which correspond to the pigments of HbRC. The same absorption bands were previously observed in the membrane fractions of heliobacteria and in water/acetone solution of BChl *g* [Amesz, 1995] [Kobayashi, 1991]. The long-wavelength absorption band of BChl *g* is unique as compared to all other known (bacterio)chlorophylls [Romero, 1988]. The absorption spectrum of the HbRC has a dominant BChl *g* band with a maximum at 786 nm and a width of ~ 40 nm. The band is inhomogeneously broadened, and low-temperature absorption spectroscopy has led to the assignment of three different pools of pigments [van Dorssen, 1985], called BChl *g* 778, 793, and 808 after their respective absorption maxima.

The absorption band at 404 - 410 nm in HbRC was previously assigned to the carotenoid 4,4'-diaponeurosporene, [Takaichi, 1997]. The absorption peak at 670 nm is indicative of Chl *a*, which acts as primary electron acceptor A_0.

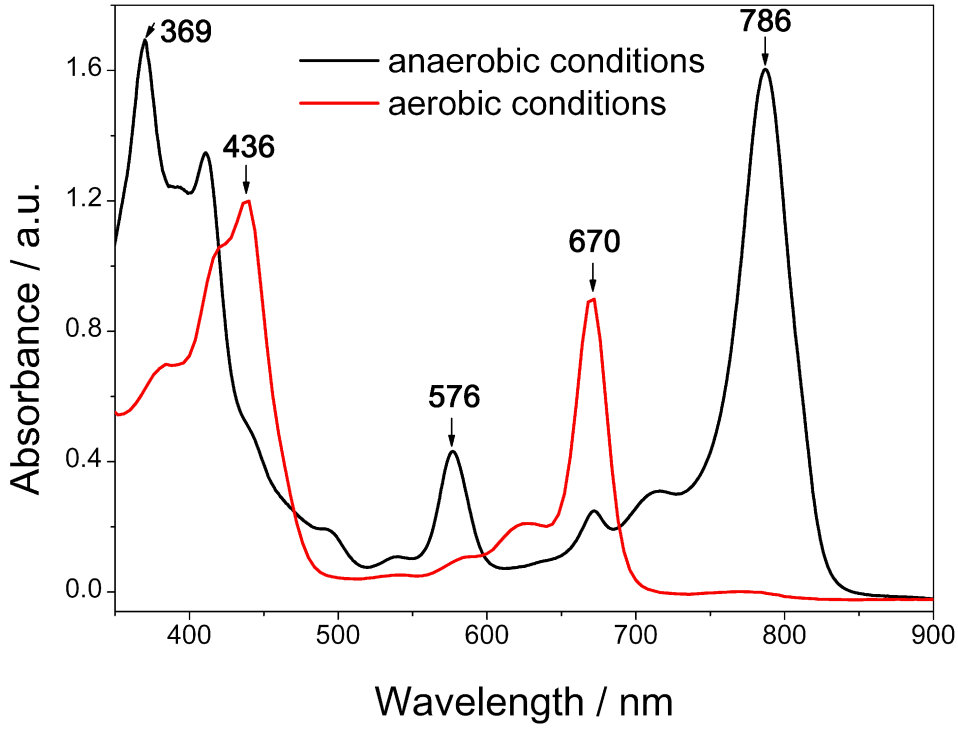

Figure 6.17 UV/Vis absorption spectra of untreated (black line) and air converted HbRC (red line) in buffer solution (50 mM MOPS) at room temperature. The decrease of the absorption at 786 and increase of the absorption at 670 nm indicates the conversion of BChl *g* to Chl *a*.

The absorption spectrum of the air converted HbRC sample shows an increase of the absorption at 670 nm, which is characteristic for Chl *a* (Fig. 6.17, red line) and a decrease of absorption at 786 nm, 576 nm and 369 nm, which corresponds to BChl *g*. The complete conversion of BChl *g* to Chl *a* in air occurs over 120 hours. The presence of additional oxidant potassium ferricyanide accelerates the conversion (4-5 hours).

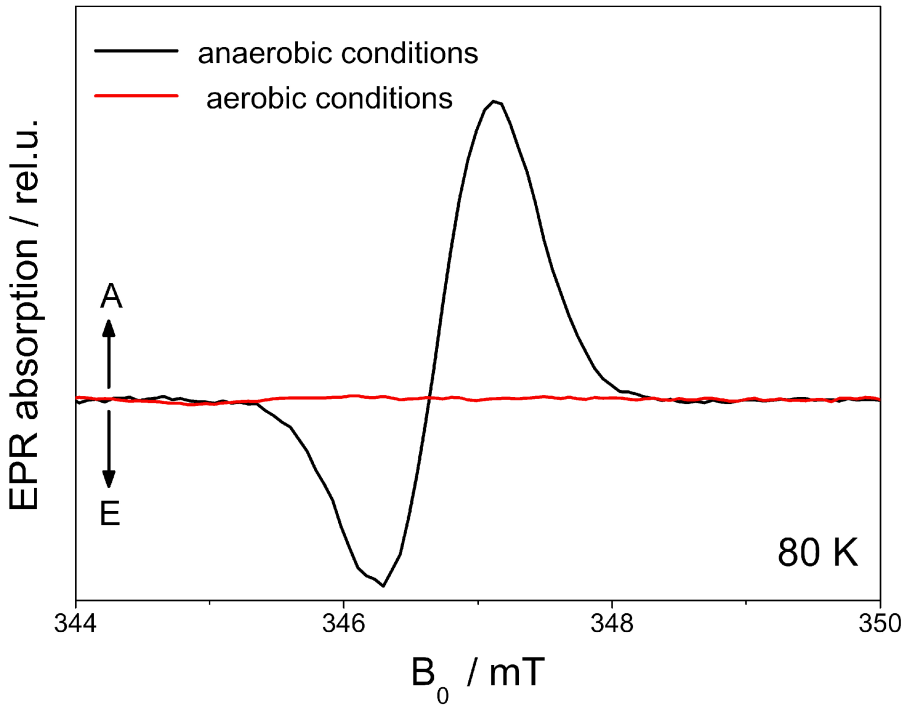

Figure 6.18 X-band TREPR spectra of untreated (black line) and air converted (red line) HbRC recorded 1 μs after the laser flash (532 nm) at 80 K.

The light-induced spin-polarized signal of $P_{798}^{\bullet+}$ was not observed in TREPR spectrum of completely converted HbRC (Fig. 6.18, red line). However, a strong triplet with polarization pattern and ZFS parameters corresponding to the triplet of Chl *a* formed by the ISC mechanism was observed (Fig.6.16*b*, green line). This implies that HbRC loses the ability for the light-induced charge separation between the primary donor and the primary electron acceptor after the conversion of BChl *g* to Chl *a*.

6.7 Action spectrum of HbRC

The dependence of the light-induced charge separation efficiency on the excitation wavelengths can provide information about the initial steps of the ET process.

The main pigment of HbRC is BChl *g*. Therefore, the maximum photoactivity is expected at excitation wavelength corresponding to the maximum absorption of this pigment around 786 nm. The first EPR experiments, however, indicated maximum EPR intensity after excitation of HbRC at 690 nm. Here, the ET efficiency of HbRC at excitation wavelengths from 440 to 910 nm was measured using the intensity of the $P_{798}^{\bullet+}$ TREPR signal in order to obtain the action spectrum. Experiments were done under unsaturated light condition, which were controlled by the light dependence of the EPR signal intensity. The peak-to-peak intensity of the $P_{798}^{\bullet+}$ signal was normalized to the number of the photons at individual excitation wavelength. The EPR signal intensity plotted against the excitation wavelengths yields the action spectrum (Fig.6.19). The action spectrum reveals two pronounced maxima at 670 nm and 786 nm. The first one (670 nm) coincides with the absorption band of Chl *a*, which is the primary electron acceptor A_0. The peak at 786 nm corresponds to absorption of BChl *g*, particularly to the electron donor P_{798}.

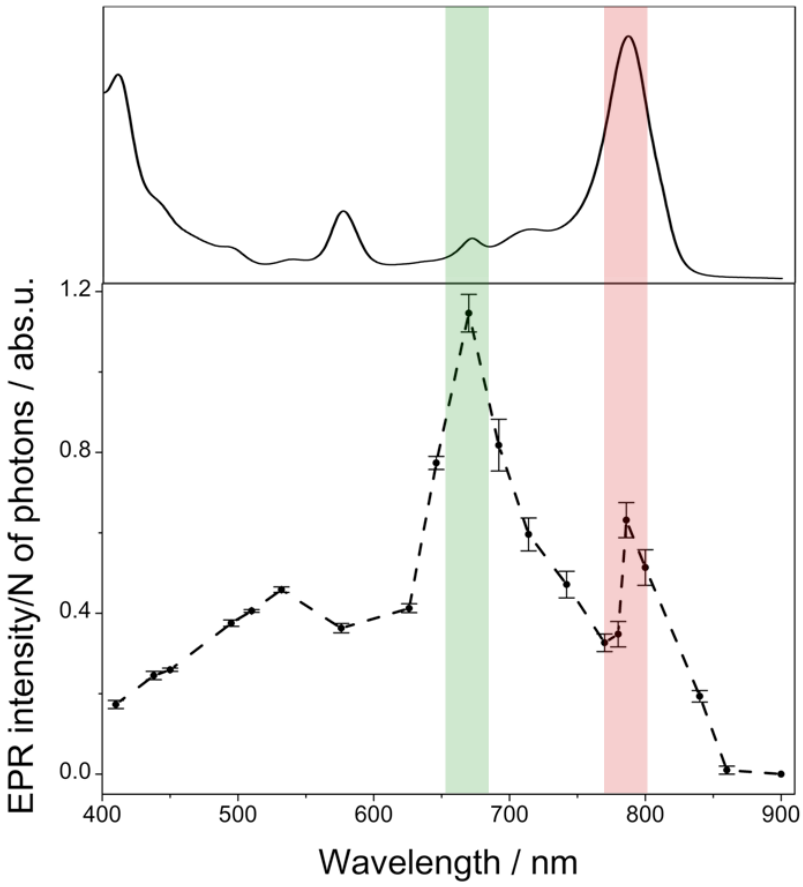

Figure 6.19 The action spectrum of the light-induced ET in HbRC (bottom panel) and corresponding absorption spectrum of HbRC (top panel). Note: The most effective excitation wavelengths in HbRC are 670 nm (Chl *a*) and 786 nm (BChl *g*).

The typical primary process of ET in a photosynthetic Type I reaction centers is charge separation between the excited electron donor P and the primary electron acceptor A_0. Therefore, the direct excitation at absorption wavelength of the donor should yield the most charge separation. However, an unusual increase of the EPR signal was detected in HbRC after excitation at the wavelength of the A_0 (Chl *a*) absorption. Thus, to explain this unexpected observation two possible charge separation pathways in HbRC have to be realized. The first one is the typical pathway: $P_{798}A_0 \rightarrow P^*_{798}A_0 \rightarrow P_{798}^{\bullet+}A_0^{\bullet-}$. The alternative pathway goes through the

excited state of A_0: $P_{798}A_0 \rightarrow P_{798}A_0^* \rightarrow P_{798}^{\bullet+}A_0^{\bullet-}$. The last mechanism of charge separation in HbRC could be more efficient because the Chl *a* (A_0) is excited directly, bypassing the "antenna". In contrast, the typical charge separation pathway proceeds via the excited donor P_{798} (BChl *g* dimer) and partially involves the excitation of "antenna" BChl *g* pigments.

This result is in good agreement with previous optical studies of Neerken et al. in membranes of *Heliobacillus mobilis* [Neerken, 2001]. Low-temperature transient absorption measurements showed a direct pathway for charge separation from the excited A_0, which does not involve the excited P_{798} state. A mechanism of the charge separation, which does not involve the excited donor, was previously proposed by ultrafast transient absorption measurements in PS I [Müller, 2003]. Here it was shown that charge separation could also proceed via the excited states of accessory chlorophylls.

6.8 Temperature dependence of charge recombination kinetics

The detection of forward ET processes did not provide clear evidence of quinone participation in the HbRC ET chain. However, information about ET cofactors can be obtain from the analysis of the recombination process in the reaction center. The charge recombination may occur from each ET acceptor, however, in the case of purified HbRC without the PshB subunit the ET ends at the acceptor F_X. After recombination of any intermediate RP the oxidized donor $P_{798}^{\bullet+}$ returns to the ground state P_{798}. Therefore, the recombination rates can be obtained from the analysis of $P_{798}^{\bullet+}$ EPR signal decays. The lifetimes of $P_{798}^{\bullet+}$ in the range of 2 to 16 ms were previously reported [Chiou, 1996]. Slow decays (12-15 ms) were obtained over a temperature range larger than 240 K and assigned to the recombination rate of $P_{798}^{\bullet+}$ $F_X^{\bullet-}$, by analogy to PS I

[Schlodder, 1998]. Biphasic decay traces (12 – 15ms and 2 – 4 ms components) were detected between 170 K and 230 K around the glass transition temperature. The fast decays (2-4 ms), detected at temperatures below 170 K and were assigned to recombination from $P_{798}^{\bullet+}A_1^{\bullet-}$ [Chiou, 1996].

The reported lifetimes of $P_{798}^{\bullet+}$ are in the order of 2 to 20 ms and can be obtained by measuring the time dependence of the $P_{798}^{\bullet+}$ thermally equilibrated EPR absorption signal, *i.e.* after T_1 relaxation of the initial polarization, in a transient EPR experiment that utilizes lock-in detection and field modulation. The time decays show no dependence on magnetic field over the EPR spectrum of $P_{798}^{\bullet+}$. Thus, the time decay is due to electron recombination and can be analyzed for temperature dependence. Fig.6.20 shows selected X- and W-band EPR decay traces recorded for the same sample at 100 K, 150 K and 230 K. The decay was found to be non-exponential. The kinetics can be deconvoluted into a biphasic decay with times of 10 to 16 ms and 2 to 4 ms, in good agreement with previous optical studies [Chiou, 1996] [Miyamoto, 2006]. The 10 to 16 ms decay is dominant at high temperatures. This decay component is not observed at low temperature; only the fast component is seen. It was suggested that the switch over from slow to fast component upon cooling may indicate *i*) a shift of $P_{798}^{\bullet+}F_X^{\bullet-}$ recombination state to a state prior to $P_{798}^{\bullet+}F_X^{\bullet-}$ in analogy to PS I [Brettel, 1997] [Schlodder, 1998]; or *ii*) faster recombination of $P_{798}^{\bullet+}F_X^{\bullet-}$ as a result of slowing protein conformational changes at low temperatures.

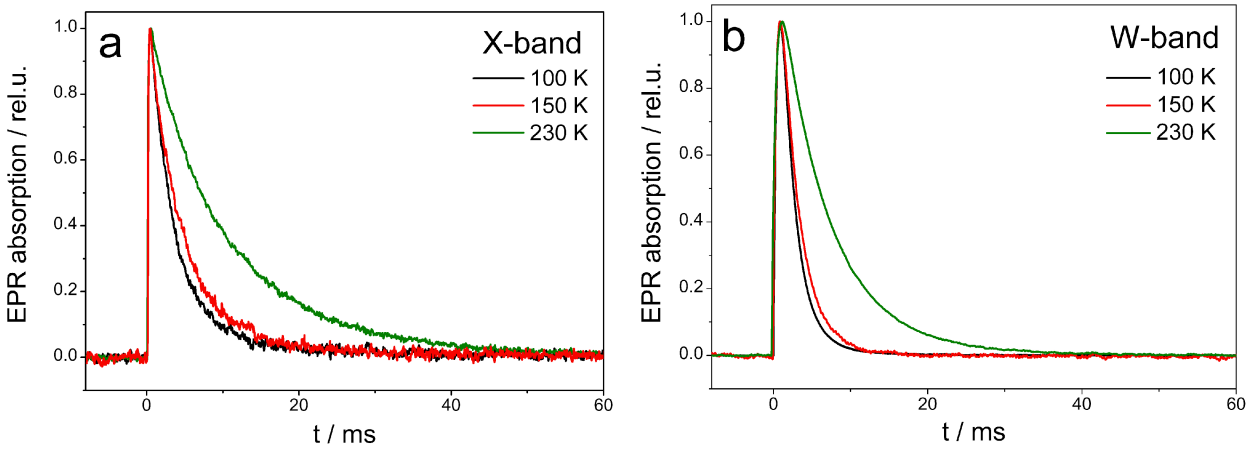

Figure 6.20 Decay profiles of the (*a*) X-band and (*b*) W-band EPR signal of $P_{798}^{\bullet+}$ after a laser flash (532 nm) obtained with transient lock-in detection and field modulation (modulation amplitude 0.3 mT). The kinetics are measured at 100 K, 150 K, and 230 K.

The first hypothesis (*i*) is, however, not supported neither by the previous investigations [Neerken, 2001] [Heinnickel, 2007] nor by the suggestion about the absence of the A_1 acceptor in the ET chain in HbRC, which were done above. Moreover, recent TREPR measurements have shown that charge recombination between $P_{798}^{\bullet+}$ and $F_X^{\bullet-}$ occurs with a time constant of ~ 3 - 5 ms at 5 K [Miyamoto, 2006], which agrees with the fast decay component. On the other hand, it was shown for the bacterial reaction center (bRC) from *Rhodobacter sphaeroides* that the protein dynamic is important for charge recombination from the primary quinone acceptor $Q_A^{\bullet-}$ to the $P_{865}^{\bullet+}$ donor [McMahon, 1998] [Kriegl, 2003]. The non-exponentiality of $P_{865}^{\bullet+}Q_A^{\bullet-}$ electron recombination kinetics was attributed to the distribution of the recombination rates due to structural heterogeneity of the RC at low temperatures [McMahon, 1998] [Kriegl, 2003]. For the unimodal distribution the time domain decay data can be described by the power law [Palazzo, 2002]:

$$A(t) = A_0 + A_1/(1+\lambda \cdot t)^n \qquad \text{(Eq.6.4)}$$

with the parameters λ and n that are related to the average decay rate constant $k = n\cdot\lambda$ ($\tau = k^{-1}$) and the width of rate distribution function $\sigma^2 = n\cdot\lambda^2$. This power law, which was previously used to describe $P_{865}^{\bullet+}Q_A^{\bullet-}$ recombination [Kleinfeld, 1984] [Palazzo, 2002], describes the EPR decays in HbRC in a suitable way. The detailed analysis of EPR decays by the power law (Eq.6.4) and biexponential ($A(t) = A_1\cdot\exp(-t/\tau_1) + A_2\cdot\exp(-t/\tau_2)$) functions at different temperatures was performed in order to prove that either: *i)* the temperature dependence of recombination due to changes in protein conformations or *ii)* a shift of the recombined charge-separated state occurs. Each individual decay is well described by power law and biexponential functions. However, the parameters obtained from biexponential analysis show a significant spread, especially over the temperature range 140-200 K, see Fig.6.21.

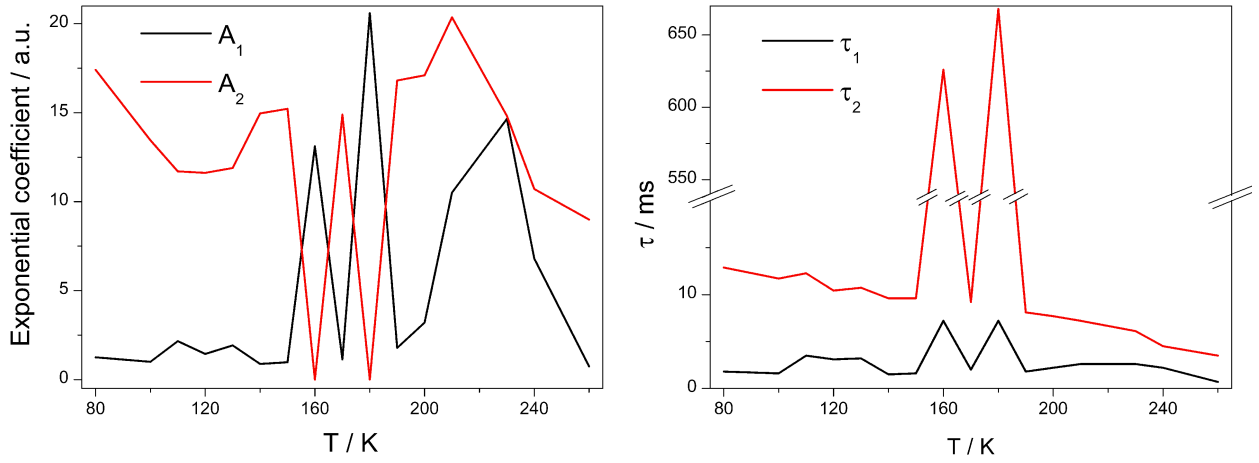

Figure 6.21 (*a*) Exponential coefficients (A_1, A_2) and (*b*) decay times (τ_1, τ_2) obtained from fitting of $P_{798}^{\bullet+}$ EPR decays with biexponential function. Significant deviations are observed in the temperature range 150-200 K.

The quality of the analysis demonstrates better agreement of the experimental data with the power law than with the biexponential function. The decay rate coefficients and width of the

distribution for the power law analysis are summarized in Table 6.1. Fig.6.22 shows average rate coefficients as a function of temperature. The comparison of the results obtained for HbRC and bacterial RC shows a similar temperature behaviour of the rate coefficients [McMahon, 1998] [Kriegl, 2003]. The recombination rate continuously increases upon cooling. A pronounced step occurs in the temperature range between 150 and 200 K.

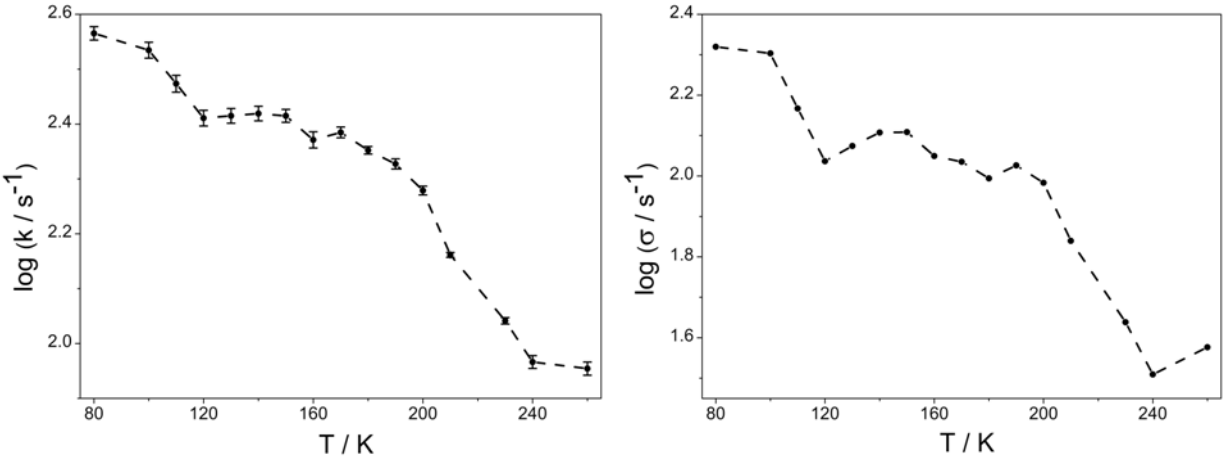

Figure 6.22 (*a*) The average rate coefficients *k* of charge recombination and (*b*) widths of the rate distribution σ on a logarithmic scale obtained from the analysis of $P_{798}^{\bullet+}$ EPR decays by the power law function (for details see text).

The width of the distribution increases linearly with increase of the average rate, *i.e.* the σ/k ratio is constant throughout the measured temperature range up to 210 K. Therefore, the standard deviation of the rate distributions f(log *k*) is temperature independent in this range. The distribution shows a tendency of narrowing above 230K, comparable to the results of previous investigations [MacMahon, 1998]. Therefore, at room temperature due to a protein conformation change, one would expect a mono-exponential decay with very narrow distribution. Unfortunately, such EPR measurements are complicated due to the high sensitivity of HbRC to

oxidation. However, good agreement between the EPR recombination kinetics in the temperature range 80 – 260 K of HbRC and bacterial RC was found. This allows us conclude that the recombination in HbRC occurs between terminal cofactors $P_{798}^{\bullet+}$ and $F_X^{\bullet-}$.

The break in Arrhenius behaviour in the temperature region between 150 K and 200 K is explained by a change of the HbRC conformational relaxation process due to the presence of a glass transition which decreases the free energy difference between redox states of the neutral and the charge separated state at high temperatures similar to the bacterial RC [Kriegl, 2003] [McMahon, 1998]. Special attention should be paid to the rate distribution, which is suggested to have a maximum around 200 K. The dynamic model predicts a broadening of the rate distribution over the temperature interval in which charge recombination occurs on the time scale of protein structural relaxation in the charge-separated state [Kriegl, 2003]. However, the quality of EPR measurements does not allow this analysis to be performed in detail. Optical methods would help to clarify this discrepancy.

Table 6.1 Kinetic parameters of charge recombination in purified HbRCs obtained from the analysis of X-band EPR decay profiles of $P_{798}^{\bullet+}$ by the power law function (see text).

T /K	k /s^{-1}	τ /ms	σ /s^{-1}	σ/k
80	367 ± 5	2.7	208 ± 11	0.56 ± 0.03
100	342 ± 5	2.9	201 ± 13	0.59 ± 0.04
110	297 ± 5	3.3	147 ± 8	0.50 ± 0.03
120	257 ± 4	3.9	109 ± 5	0.42 ± 0.02
130	260 ± 4	3.89	119 ± 5	0.46 ± 0.02
140	262 ± 3	3.8	128 ± 6	0.49 ± 0.03
150	260 ± 3	3.8	128 ± 6	0.50 ± 0.02
160	235 ± 4	4.3	112 ± 6	0.48 ± 0.03
170	242 ± 2	4.1	108 ± 4	0.45 ± 0.02
180	225 ± 2	4.4	99 ± 3	0.44 ± 0.01
190	212 ± 2	4.7	106 ± 5	0.50 ± 0.02
200	190 ± 1	5.3	96 ± 4	0.51 ± 0.02
210	145 ± 1	7	69 ± 2	0.48 ± 0.01
230	110 ± 1	9	43 ± 1	0.40 ± 0.01
240	92 ± 1	10.8	32 ± 1	0.35 ± 0.02
260	90 ± 1	11.1	38 ± 2	0.42 ± 0.02

6.9 Summary

Heliobacterial reaction centers (HbRCs) extracted from *Heliobacterium modesticaldum* were studied by multifrequency transient EPR (TREPR) methods. The main aim was to clarify the participation of quinone in the electron transfer processes in HbRC.

The direct detection of the spin-correlated radical pairs ($P_{798}^{\bullet+}A_0^{\bullet-}$ and/or $P_{798}^{\bullet+}A_1^{\bullet-}$) in HbRC is difficult due to the very short lifetimes. The contribution of the $P_{798}^{\bullet+}$ in the radical pair (RP) $P_{798}^{\bullet+}F_X^{\bullet-}$ is detectable in TREPR experiments (Fig.6.4). This is in agreement with results of a previous study [van der Est, 1998]. The simulation of W-band photoaccumulated EPR signal yields the principal g-values [2.00307; 2.00249; 2.00224] (error ± $2 \cdot 10^{-5}$). This signal is assigned to the radical $P_{798}^{\bullet+}$. The obtained g-values are very close to results for the radical cation of the electron donor $P_{700}^{\bullet+}$ in PS I [Bratt, 1997] [Zech, 2000]. This reveals the similarities of the chemical nature of both donors: P_{700} in PS I (dimer of chlorophyll *a*) and P_{798} in HbRC (dimer of bacteriochlorophyll *g*).

The analysis of the $P_{798}^{\bullet+}$ spin polarization and $P_{798}^{\bullet+}$ recombination kinetics yields information on ET steps. The spin polarization was investigated by X, Q and W-band EPR methods. The high-field W-band EPR studies allowed determination of the absolute values of the net polarization. The net polarization of $P_{798}^{\bullet+}$ increases with increasing magnetic field. This frequency dependence can be well explained without taking into account the transient RP $P_{798}^{\bullet+}A_1^{\bullet-}$. The observed polarization is most probably generated in the short-lived $P_{798}^{\bullet+}A_0^{\bullet-}$ RP as precursor to $P_{798}^{\bullet+}F_X^{\bullet-}$. The analysis of EPR recombination kinetics in the temperature range 80-260 K also shows that the recombination presumably occurs between two

cofactors $F_X^{\bullet-}$ and $P_{798}^{\bullet+}$. However, the analysis of neither the spin polarization nor the recombination kinetics of the $P_{798}^{\bullet+}$ allow to explicitly exclude the quinone participation in the ET chain, assuming that the lifetime of RP $P_{798}^{\bullet+}A_1^{\bullet-}$ is very short.

Biochemical treatment methods may influence the lifetime of intermediates in the RP in photosynthetic RCs. Therefore, a set of biochemical treated HbRC samples was studied by TREPR. The procedure of quinone replacement, which was successfully applied to PS I, was used for HbRC in order to achieve an increase of the $P_{798}^{\bullet+}A_1^{\bullet-}$ lifetime. However, it was found that procedure of quinone replacement in HbRC influences neither the spin polarization pattern nor the EPR signal decays of $P_{798}^{\bullet+}$. This leads to the following conclusion: *i)* if the quinone participates in HbRC ET, then the quinone cannot be replaced by the substitution procedure; *ii)* or the quinone does not participate in ET, then EPR signals are independent of the replacement as expected. An attempt was made to remove the terminal acceptor F_X, as was previously applied to PS I, using the oxidant potassium ferricyanide. This failed due to the high sensitivity of the BChl *g* pigments to oxidation. HbRC were found to lose the ability of the charge separation after conversion of BChl *g* to Chl *a* under oxidation conditions. Light excitation of the oxidized HbRC results in the formation of polarized Chl *a* triplets via the intersystem crossing mechanism. In contrast, illumination of untreated HbRC results in the formation of triplet states of the carotenoid 4,4'-diaponeurosporene, which were detected in the EPR spectrum.

The efficiency dependence of charge separation on the excitation wavelength was measured in order to obtain the action spectrum of HbRC. The action spectrum showed a maximum efficiency of ET at an excitation wavelength of 670 nm, which corresponds to the absorption of Chl *a*. Untreated HbRCs contain only two Chl *a* molecules, which act as primary acceptor A_0.

Therefore, in HbRC an "alternative" path of charge separation is proposed. The typical pathway of charge separation in the RC starts from excitation of the primary electron donor P_{798}: $P_{798}A_0 \rightarrow P^*_{798}A_0 \rightarrow P_{798}^{\bullet+}A_0^{\bullet-}$. The alternative pathway goes through the excited state of the acceptor A_0: $P_{798}A_0 \rightarrow P_{798}A^*_0 \rightarrow P_{798}^{\bullet+}A_0^{\bullet-}$. This result is supported by previous optical studies [Neerken, 2001].

The experimental results as well as the parameters obtained from data analysis do not explicitly require the formation of the intermediate RP $P_{798}^{\bullet+}A_1^{\bullet-}$, *i.e.* quinone participation in ET. However, it does not allow to resolve clearly the apparent contradiction between photoaccumulation EPR results [Brok, 1986] [Miyamoto, 2006] and chemical analysis of the HbRC [Trost, 1989], which suggest the presence of a quinone acceptor, or the transient absorption [Lin, 1994] and photovoltage [Brettel, 1998] data, which indicate that there is no quinone involved in the ET.

|Bibliography to Chapter 6

Amesz J., (1995) The Heliobacteria, a New Group of Photosynthetic Bacteria. J. Photochemistry and Photobiology B, 30, 89-96.

Bittl R., Schlodder E., Geisenheimer I., Lubitz W., and Cogdell R.J. (2001) Transient EPR and Absorption Studies of Carotenoid Triplet Formation in Purple Bacterial Antenna Complexes. J. Phys. Chemistry B, 105, 5525-5535.

Bratt P.J., Poluektov O.G., Thurnauer M.C., Krzystek J., Brunel L.C., Schrier J., Hsiao Y.W., Zerner M. and Angerhofer A. (2000) The g-factor Anisotropy of Plant Chlorophyll *a*. J.Phys. Chemistry B, 104, 6973-6977.

Brettel K. (1988) Electron Transfer from A_1^- to an Iron–sulfur Center with $t_{1/2}$ = 200 ns at Room Temperature in Photosystem I. Characterization by Flash Absorption Spectroscopy. FEBS Letters, 239, 93–98.

Brettel K. (1997) Electron Transfer and Arrangement of the Redox Cofactors in Photosystem I. Biochimica et Biophysica Acta, 1318, 322-373.

Brettel K. and Leibl W. (2001) Electron Transfer in Photosystem I. Biochimica et Biophysica Acta, 1507, 100-114.

Brettel K., Leibl W. and Liebl U. (1998) Electron Transfer in the Heliobacterial Reaction Center: Evidence against a Quinone-type Electron Acceptor Functioning Analogous to A_1 in Photosystem I. Biochimica et Biophysica Acta, 363, 175–181.

Brockmann H. and Lipinski A. (1983) Bacteriochlorophyll *g* - a New Bacteriochlorophyll from *Heliobacterium Chlorum*. Arch. Microbiology, 136, 17-19.

Brok M., Vasmel H., Horikx J.T.G. and Hoff A.J. (1986) Electron Transport Components of *Heliobacterium chlorum* Investigated by EPR Spectroscopy at 9 and 35 GHz. FEBS Letters, 194, 322–326.

Budil D.E. and Thurnauer M.C. (1991) The Chlorophyll Triplet State as a Probe of Structure and Function in Photosynthesis. Biochimica et Biophysica Acta, 1057, 1-41.

Chambers J.Q. (1974) The Chemistry of the Quinonoid Compounds, ed. Patai S., Publishers: Wiley&Sons, London.

Chiou H.C. and Blankenship R.E., (1996) Temperature Dependence of Charge Recombination in *Heliobacillus mobilis*. Photochemistry and Photobiology, 64, 32-37.

Cogdell R.J. and Frank H.A. (1987) How Carotenoids Function in Photosynthetic Bacteria. Biochimica et Biophysica Acta, 895, 63-79.

Cohen R.O, Shen G, Golbeck J.H, Xu W., Chitnis P.R., Valieva A.I, van der Est A., Pushkar Y. and Stehlik D. (2004) Evidence for Asymmetric Electron Transfer in Cyanobacterial Photosystem I: Analysis of a Methionine-to-Leucine Mutation of the Ligand to the Primary Electron Acceptor A_0. Biochemistry, 43, 4741-4754.

Fischer M. R. (1990) Photosynthetic Electron Transfer in *Heliobacterium chlorum* Studied by EPR Spectroscopy. Biochimica et Biophysica Acta, 1015, 471-481.

Frank H. A., Friesner R., Nairn J. A., Dismukes G. C., Sauer K. (1979) Orientation of the Primary Donor in Bacterial Photosynthesis. Biochimica et Biophysica Acta, 547, 484-501.

Frank H.A. and Cogdell R.J. (1996) Carotenoids in Photosynthesis. Photochemistry and Photobiology, 63, 257-264.

Fromme P., Jordan P. and Krauss N. (2001) Structure of Photosystem I. Biochimica et Biophysica Acta, 1507, 5-31.

Gest H. and Favinger J.L. (1983) *Heliobacterium Chlorum*, an Anoxygenic Brownish-green Photosynthetic Bacterium Containing a New Form of Bacteriochlorophyll. Arch. Microbiology, 136, 11-16.

Golbeck J.H. and Warden J.T. (1982) Electron Spin Resonance Studies of the Bound Iron-sulfur Centers in Photosystem I - Photoreduction of Center A Occurs in the Absence of Center B. Biochimica et Biophysica Acta, 681, 77-84.

Hauska G., Schoedl T., Remigy H. and Tsiotis G. (2001) The Reaction Center of Green Sulfur Bacteria. Biochimica et Biophysica Acta, 1507, 260-277.

Heathcote P., Moenne-Loccoz P., Rigby S. E. J. and Evans M. C. W. (1996) Photoaccumulation in Photosystem I Does Produce a Phylloquinone $A_1^{\bullet-}$ radical. Biochemistry, 35, 6644-6650.

Heinnickel M. and Golbeck J.H. (2007) Heliobacterial Photosynthesis. Photosynthesis Research, 92, 35-53.

Heinnickel M., Agalarov R., Svensen N., Krebs C. and Golbeck J.H. (2006) Identification of F_X in the Heliobacterial Reaction Center as Cluster with an S = 3/2 Ground Spin State. Biochemistry, 45, 6756-6764.

Heinnickel M., Shen G. Z., Agalarov R. and Golbeck J. H.(2005) Resolution and Reconstitution of a Bound Fe-S Protein from the Photosynthetic Reaction Center of *Heliobacterium modesticaldum*. Biochemistry, 44, 9950-9960.

Hiraishi A. (1989) Occurence of Menaquinone as the Sole Isoprennoid in the Photosynthetic Bacterium *Heliobacterium Chlorum*. Arch. Microbiology, 151, 378-379.

Hulsebosch R. J., Borovykh I. V., Paschenko S. V., Gast P. and Hoff A. J. (1999) Radical Pair Dynamics and Interactions in Quinone-reconstituted Photosynthetic Reaction Centers of *Rb. sphaeroides R26:* A Multifrequency Magnetic Resonance Study. J. Phys. Chemistry B, 103, 6815-6823.

Hulsebosch R. J., Borovykh I. V., Paschenko S. V., Gast P. and Hoff A. J. (2001) Radical Pair Dynamics and Interactions in Quinone-reconstituted Photosynthetic Reaction Centers of *Rb. sphaeroides R26:* A Multifrequency Magnetic Resonance Study. J. Phys. Chemistry B, 105, 10146-10146.

Itoh S., Iwaki M., and Ikegami I. (2001) Modification of Photosystem I Reaction Center by the Extraction and Exchange of Chlorophylls and Quinones. Biochimica et Biophysica Acta, 1507, 115-138.

Joliot P. and Joliot A. (1999) In vivo Analysis of the Electron Transfer within Photosystem I: are the Two Phylloquinones Involved? Biochemistry, 38, 11130–11136.

Kamlowski A., Frankemoller L., van der Est A., Stehlik D. and Holzwarth A. R. (1996) Evidence for Delocalization of the Triplet State $^3P_{680}$ in the D(1)D(2)cytb(559)-complex of Photosystem II. In 95th Annual Meeting of the Deutsche-Bunsen-Gesellschaft-fur-Physikalische-Chemie on Primary Processes of Photosynthesis, Jena, Germany.

Kandrashkin Y. E., Vollmann W., Stehlik D., Salikhov K. and van der Est A. (2002) The Magnetic Field Dependence of the Electron Spin Polarization in Consecutive Spin Correlated Radical Pairs in Type I Photosynthetic Reaction Centres. Molecular Physics, 100, 1431-1443.

Kandrashkin Y.E., Salikhov K.M. and Stehlik D. (1996) Spin Dynamics and EPR Spectra of Consecutive Spin-correlated Radical Pairs. Model Calculations. In 28th Congress of the AMPERE on Magnetic Resonance and Related Phenomena, Canterbury, England.

Kjaer B., Frigaard N. U., Yang F., Zybailov B., Miller M., Golbeck J. H. and Scheller, H. V. (1998) Menaquinone-7 in the Reaction Center Complex of the Green-sulfur Bacterium *Chlorobium vibrioforme* Functions as the Electron Acceptor A_1. Biochemistry, 37, 3237-3242.

Kleinfeld D., Okamura M.Y. and Feher G. (1984) Electron-Transfer Kinetics in Photosynthetic Reaction Centers Cooled to Cryogenic Temperatures in the Charge-Separated State - Evidence for Light-Induced Structural-Changes. Biochemistry, 23, 5780-5786.

Kleinherenbrink F. A., Hastings M., Wittmershaus G. and Blankenship R. E. (1994) Delayed Fluorescence from Fe-S Type Photosynthetic Reaction Centers at Low Redox Potential. Biochemistry, 33, 3096-3105.

Kobayashi M., Hamano T., Akiyama M., Watanabe T., Inoue K., Oh-oka H., Amesz J., Yamamura M. and Kise H. (1998) Light-independent Isomerization of Bacteriochlorophyll *g* to Chlorophyll *a* Catalyzed by Weak Acid in vitro. Analytica Chimica Acta, 365, 199-203.

Kobayashi M., van den Meent E. J., Erkelens C., Amesz J., Ikegami I. and Watanabe T. (1991) Bacteriochlorophyll *g* Epimer as a Possible Reaction Center Component of Heliobacteria. Biochimica et Biophysica Acta, 1057, 89-96.

Kriegl J.M., Forster F.K. and Nienhaus G.U. (2003) Charge Recombination and Protein Dynamics in Bacterial Photosynthetic Reaction Centers Entrapped in a Sol-gel Matrix. Biophysical Journal, 85, 1851-1870.

Levanon H. and Norris J.R. (1978) The Photoexcited Triplet State and Photosynthesis. Chem. Reviews, 78, 185-198.

Liebl U., Mockensturm-Wilson M., Trost J. T., Brune D. C., Blankenship R. E. and Vermaas W. (1993) Single Core Polypeptide in the Reaction Center of the Photosynthetic Bacterium *Heliobacillus mobilis*. Proc. Natl. Acad. Sci. USA, 90, 7124-7128.

Lin S., Chiou H. C. and Blankenship R. E. (1994) Secondary-Electron Transfer Processes in Membranes of *Heliobacillus mobilis*. Biochemistry, 34, 12761-12767.

Marcus R.A. and Sutin N. (1985) Electron Transfer in Chemistry and Biology. Biochimica et Biophysica Acta, 881, 265-322.

Mathis P., Setif P. (1988) Kinetic Studies on the Function of A_1 in the Photosystem I Reaction Center, FEBS Letters, 237, 65–68.

McMahon B. H., Müller J. D., Wraight C. A. and Nienhaus G. U. (1998) Electron Transfer and Protein Dynamics in the Photosynthetic Reaction Center. Biophysical Journal, 74, 2567-2587.

Miyamoto R., Iwaki M., Mino H., Harada J., Itoh S. and Oh-oka H. (2006) ESR Signal of the Iron-sulfur Center F_X and its Function in the Homodimeric Reaction Center of *Heliobacterium modesticaldum*. Biochemistry, 45, 6306-6316.

Möbius K. and Savitsky A. (2009) High-Field EPR Spectroscopy on Proteins and their Model Systems: Characterization of Transient Paramagnetic States. Publishers: RSC Publishing, London.

Morris A. L., Snyder S. W., Zhang Y. N., Tang J., Thurnauer M. C., Dutton P. L., Robertson D. E. and Gunner M. R. (1995) Electron-Spin Polarization Model Applied to Sequential Electron-Transfer in Iron-Containing Photosynthetic Bacterial Reaction Centers with Different Quinones as Q_A. J. Phys. Chemistry, 99, 3854-3866.

Müller M. G., Niklas J., Lubitz W. and Holzwarth A. R. (2003) Ultrafast Transient Absorption Studies on Photosystem I Reaction Centers from *Chlamydomonas reinhardtii*. 1. A New Interpretation of the Energy Trapping and Early Electron Transfer Steps in Photosystem I. Biophysical Journal, 85, 3899-3922.

Neerken S. and J. Amesz (2001) The Antenna Reaction Center Complex of Heliobacteria: Composition, Energy Conversion and Electron Transfer. Biochimica et Biophysica Acta, 1507, 278-290.

Norris J. R., Morris A. L., Thurnauer M. C. and Tang J. (1990) A General Model of Electron-spin Polarization Arising from the Interactions in the Radical Pairs. J. Chem. Physics, 92, 4239-4249.

Oh-oka H. (2007) Type 1 Reaction Center of Photosynthetic Heliobacteria. Photochemistry and Photobiology, 83, 177-186.

Palazzo G., Mallardi A., Hochköppler A., Cordone L. and Venturoli G. (2002) Electron Transfer Kinetics in Photosynthetic Reaction Centers Embedded in Trehalose Glasses:

Trapping of Conformational Substates at Room Temperature. Biophysical Journal, 82, 558-568.

Pedersen J.B. (1979) Determination of the Primary Reaction of Photosynthesis from Transient ESR Signals. FEBS Letters, 97, 305-310.

Prince R.C., Gest H. and Blankenship R.E. (1985) Thermodynamic Properties of the Photochemical Reaction Center of *Heliobacterium chlorum*. Biochimica et Biophysica Acta, 810, 377-384.

Proskuryakov I.I., Klenina I. B., Hore P. J., Bosch M. K., Gast P. and Hoff A. J. (1996) Electron Paramagnetic Resonance of the Primary Radical Pair in Reaction Centers of Photosynthetic Bacteria. Chem. Phys. Letters, 257, 333-339.

Proskuryakov I.I., Klenina I. B., Shkuropatov A. Y., Shkuropatova V. A. and Shuvalov V. A. (1993) Free-Radical and Correlated Radical-Pair Spin-Polarized Signals in *Rhodobacter sphaeroides R-26* Reaction Centers. Biochimica et Biophysica Acta, 1142, 207-210.

Pushkar Y. N., Karyagina I., Stehlik D., Brown S. and van der Est A. (2005) Recruitment of a Foreign Quinone into the A_1 Site of Photosystem I. J. Biol. Chemistry, 280, 12382-12390.

Romero P.B., Favinger J.L. and Gest H. (1988) Distinctive Properties of Bacilloform Photosynthetic Heliobacteria. FEMS Microbiol.Letters, 49, 451-454.

Savitsky A., Heinnickel M., Khuzeeva L., Antonkine M.L., Möbius K. and Golbeck J.H. (2008) Characterization of Homodimeric Type I Reaction Center Cores from *Heliobacterium modesticaldum* by High-field Electron Paramagnetic Resonance Spectroscopy, in Photosynthesis. Energy from the Sun. J.F. Editors: Allen, et al., Springer: Heidelberg., 65-68.

Schlodder E., Falkenberg K., Gergeleit M. and Brettel K. (1998) Temperature Dependence of Forward and Reverse Electron Transfer from $A_1^{\bullet-}$, the Reduced Secondary Electron Acceptor in Photosystem I. Biochemistry, 37, 9466-9476.

Sieckmann I., Brettel K., Bock C., van der Est A. and Stehlik D. (1993) Transient Electron Paramagnetic Resonance of the Triplet State of P_{700} in Photosystem I: Evidence for Delocalization at Room Temperature. Biochemistry, 32, 4842-4847.

Takaichi S., Inoue K., Akaike M., Kobayashi M., Oh-oka H. and Madigan M. T. (1997) The Major Carotenoid in All Known Species of Heliobacteria is the C-30 Carotenoid 4,4'-diaponeurosporene, not Neurosporene. Arch. Microbiology, 168, 277-281.

Tang J., Utschig L. M., Poluektov O., Thurnauer M. C. (1999) Transient W-band EPR Study of Sequential Electron Transfer in Photosynthetic Bacterial Reaction Centers. J. Phys. Chemistry B, 103, 5145-5150.

Thurnauer M.C. and Norris J.R. (1977) The Ordering of the Zero-field triplet Spin Sublevels in the Chlorophyll. A Magnetophotoselection Study. Chem. Phys. Letters, 47, 100-105.

Till U. Klenina I. B., Proskuryakov I.I., Hoff A. J. and Hore P. J. (1997) Recombination Dynamics and EPR Spectra of the Primary Radical Pair in Bacterial Photosynthetic Reaction Centers with Blocked Electron Transfer to the Primary Acceptor. J. Phys. Chemistry B, 101, 10939-10948.

Trost J.T. and Blankenship R.E. (1989) Isolation of a Photoactive Photosynthetic Reaction Center-core Antenna Complex from *Heliobacillus mobilis*. Biochemistry, 28, 9898-9904.

Un S., Dorlet P. and Rutherford A.W. (2001) A High-field EPR Tour of Radicals in Photosystems I and II. Appl. Magn. Resonance, 21, 341-361.

van den Meent E. J., Kobayashi M., Erkelens C., van Veelen P. A., Amesz J. and Watanabe T. (1991) Identification of 8^1-hydroxychlorophyll a as a Functional Reaction Center Pigment in Heliobacteria. Biochimica et Biophysica Acta, 1058, 356-362.

van den Meent E.J., Kleinherenbrink F.A.M. and Amesz J. (1990) Purification and Properties of an Antenna Reaction Center Complex from Heliobacteria. Biochimica et Biophysica Acta, 1015, 223-230.

van der Est A., Hager-Braun C., Leibl W., Hauska G. and Stehlik D. (1998) Transient Electron Paramagnetic Resonance Spectroscopy on Green-sulfur bacteria and Heliobacteria at Two Microwave Frequencies. Biochimica et Biophysica Acta, 1409, 87-98.

van der Est A., Prisner T., Bittl R., Fromme P.,. Lubitz W, Möbius K. and Stehlik D. (1997) Time-resolved X-, K-, and W-band EPR of the Radical Pair State $P_{700}^{\bullet+}A_1^{\bullet-}$ of Photosystem I in Comparison with $P_{865}^{\bullet+}Q_A^{\bullet-}$ in Bacterial Reaction Centers. J. Phys. Chemistry B, 101, 1437–1443.

van Dorssen R. J., Vasmel H. and Amesz J. (1985) Antenna Organization and Energy Transfer in Membranes of *Heliobacterium Chlorum*. Biochimica et Biophysica Acta, 809, 199-203.

van Kan P.J.M., Aartsma T.J. and Amesz J. (1989) Primary Photosynthetic Processes in *Heliobacterium chlorum* at 15K. Photosynth. Research, 22, 61-68.

Vrieze J., E. van den Meent and Hoff A. (1998) Triplet Properties and Interactions of the Primary Electron Donor and Antenna Chromophores in Membranes of *Heliobacterium chlorum*, Studied with ADMR Spectroscopy. Biochemistry, 37, 14900-14909.

Woese C.R., Debrunner-Vossbrinck B.A., Oyaizu H., Stackebrandt E. and Ludwig W. (1985) Gram-positive Bacteria: Possible Photosynthetic Ancestry, Science, 229 762-765.

Zech S. G., Gardiner A.T., Lubitz W. and Bittl R. (2000) A Structural Model for the Charge Separated State $P_{700}^{\bullet+}A_1^{\bullet-}$ in Photosystem I from the Orientation of the Magnetic Interaction Tensors. J. Phys. Chemistry B, 104, 9728-9739.

Zech S.G., Gerdiner A.T., Lubitz W and Bittl R. (1998) Time and Temperature Dependence of transient EPR Spectra of the Radical Pair $P_{865}^{\bullet+}[Fe^{2+}Q_A^{\bullet-}]$ in Iron-Containing Bacterial Reaction Centers of *Rhodobacter sphaerodies* R-26. Proceedings of the Joint 29th Ampere – 13th ISMAR International Conference, 949-950.

Zech S.G., van der Est A.J. and Bittl R. (1997) Measurement of Cofactor Distances Between $P_{700}^{\bullet+}A_1^{\bullet-}$ in Native and Quinone-substituted Photosystem I using Pulsed Electron Paramagnetic Resonance Spectroscopy. Biochemistry, 36, 9774–9779.

Appendix

Coordinates (xyz) of Chl *a* for DFT calculation

Mg	**-0.0392**	**0.0928**	**1.4062**
C	**-0.1606**	**-1.4162**	**-1.7457**
C	**0.3406**	**3.1539**	**-0.1312**
C	**-0.0327**	**1.5503**	**4.5113**
C	**-0.3353**	**-3.0791**	**2.8989**
N	**0.0539**	**0.7484**	**-0.6419**
C	**-0.0536**	**-0.0337**	**-1.7847**
C	**-0.0744**	**0.8397**	**-3.0474**
C	**0.4940**	**2.1938**	**-2.5140**
C	**0.2687**	**2.0689**	**-0.9946**
C	**1.9965**	**2.3854**	**-2.8435**
C	**-1.5162**	**0.9405**	**-3.6328**
C	**-1.6038**	**1.3462**	**-5.1317**
C	**-1.2782**	**2.8137**	**-5.4250**
O	**-1.9501**	**3.7370**	**-4.9953**
O	**-0.1993**	**3.1383**	**-6.2328**
N	**0.1111**	**2.0384**	**2.0830**
C	**0.2507**	**3.1795**	**1.3035**
C	**0.3071**	**4.3493**	**2.1382**
C	**0.2001**	**3.8979**	**3.4807**
C	**0.0835**	**2.4429**	**3.4114**
C	**0.4591**	**5.7688**	**1.6592**
C	**0.1972**	**4.6515**	**4.7235**
C	**0.2241**	**5.9993**	**4.9402**
N	**-0.1550**	**-0.6376**	**3.3535**
C	**-0.1356**	**0.1458**	**4.4983**
C	**-0.2362**	**-0.7117**	**5.6826**
C	**-0.3134**	**-2.0212**	**5.2278**
C	**-0.2651**	**-1.9656**	**3.7598**
C	**-0.2287**	**-0.2259**	**7.1095**
C	**-0.3943**	**-3.2819**	**6.0575**
C	**0.9818**	**-3.9222**	**6.3770**
N	**-0.1877**	**-1.8518**	**0.7626**
C	**-0.3067**	**-3.0685**	**1.4738**
C	**-0.3951**	**-4.1815**	**0.5581**
C	**-0.3292**	**-3.5972**	**-0.7438**
C	**-0.2038**	**-2.1882**	**-0.5444**
C	**-0.5308**	**-5.6402**	**0.8990**
C	**-0.3729**	**-3.8848**	**-2.1570**
O	**-0.4828**	**-4.9470**	**-2.7885**
C	**-0.2772**	**-2.4240**	**-2.8959**
C	**0.8796**	**-2.4406**	**-3.8773**
O	**2.0678**	**-2.2830**	**-3.6251**
O	**0.4275**	**-2.7188**	**-5.1575**
C	**1.4620**	**-2.9370**	**-6.1483**

C	**0.6671**	**2.1309**	**-6.8120**
H	**0.4964**	**4.1263**	**-0.6159**
H	**-0.0374**	**2.0146**	**5.5046**
H	**-0.4288**	**-4.0615**	**3.3785**
H	**0.5893**	**0.4031**	**-3.8216**
H	**-0.0681**	**3.0585**	**-2.9167**
H	**2.3854**	**3.3119**	**-2.3805**
H	**2.1596**	**2.4597**	**-3.9383**
H	**2.5961**	**1.5355**	**-2.4626**
H	**-2.1203**	**1.6396**	**-3.0219**
H	**-2.0026**	**-0.0498**	**-3.5498**
H	**-2.6575**	**1.2259**	**-5.4535**
H	**-1.0025**	**0.6424**	**-5.7342**
H	**1.3234**	**6.2742**	**2.1394**
H	**-0.4365**	**6.3856**	**1.8891**
H	**0.6138**	**5.8187**	**0.5661**
H	**0.1641**	**4.0284**	**5.6310**
H	**0.2169**	**6.3902**	**5.9669**
H	**0.2466**	**6.7424**	**4.1353**
H	**-0.8835**	**0.6579**	**7.2463**
H	**-0.5776**	**-1.0097**	**7.8086**
H	**0.7883**	**0.0770**	**7.4401**
H	**-0.9137**	**-3.0646**	**7.0143**
H	**-1.0236**	**-4.0334**	**5.5377**
H	**1.6208**	**-3.2248**	**6.9548**
H	**0.8613**	**-4.8504**	**6.9735**
H	**1.5270**	**-4.1796**	**5.4484**
H	**-0.5743**	**-5.8090**	**1.9911**
H	**-1.4473**	**-6.0789**	**0.4517**
H	**0.3203**	**-6.2313**	**0.4998**
H	**-1.2163**	**-2.3227**	**-3.4758**
H	**0.9252**	**-3.1519**	**-7.0875**
H	**2.1007**	**-2.0395**	**-6.2604**
H	**2.0990**	**-3.7950**	**-5.8626**
H	**0.1183**	**1.4907**	**-7.5305**
H	**1.1464**	**1.5054**	**-6.0363**
H	**1.4437**	**2.6987**	**-7.3520**

Coordinates (xyz) of Chl *a* with tyrosine and methionine ligands for DFT calculation

C	**2.9294**	**0.2650**	**1.1925**
S	**2.7500**	**2.0335**	**0.7269**
C	**2.9627**	**2.8327**	**2.3662**
C	**2.2794**	**-9.8445**	**3.3695**
C	**1.2720**	**-8.7746**	**2.9831**
C	**-0.0364**	**-8.7675**	**3.5191**
C	**1.5920**	**-7.7632**	**2.0500**
C	**-0.9837**	**-7.8031**	**3.1415**
C	**0.6584**	**-6.7886**	**1.6576**
C	**-0.6499**	**-6.7986**	**2.2013**
O	**-1.6059**	**-5.8847**	**1.8715**
Mg	**-0.0863**	**2.3386**	**0.3291**
C	**-0.3037**	**-0.7680**	**-1.2808**
C	**0.5268**	**3.8110**	**-2.7098**
C	**-0.4789**	**5.4163**	**1.8315**
C	**-1.0201**	**0.7787**	**3.3536**
N	**0.0216**	**1.6013**	**-1.7082**
C	**-0.0909**	**0.2923**	**-2.1587**
C	**0.0310**	**0.2485**	**-3.6958**
C	**0.7878**	**1.5850**	**-3.9762**
C	**0.4145**	**2.4251**	**-2.7449**
C	**2.3201**	**1.3938**	**-4.0998**
C	**-1.3560**	**0.2554**	**-4.4208**
C	**-2.0811**	**-1.0982**	**-4.5465**
C	**-1.4781**	**-2.0277**	**-5.6066**
O	**-0.6500**	**-1.6801**	**-6.4331**
O	**-1.9525**	**-3.3226**	**-5.6848**
N	**-0.0199**	**4.3050**	**-0.3350**
C	**0.2862**	**4.7187**	**-1.6213**
C	**0.3359**	**6.1582**	**-1.6839**
C	**0.0457**	**6.6318**	**-0.3789**
C	**-0.1708**	**5.4408**	**0.4442**
C	**0.6321**	**6.9784**	**-2.9113**
C	**-0.0444**	**7.9915**	**0.1257**
C	**0.1546**	**9.1837**	**-0.5079**
N	**-0.6295**	**2.9787**	**2.2589**
C	**-0.6969**	**4.3022**	**2.6675**
C	**-1.0373**	**4.3619**	**4.0925**
C	**-1.1793**	**3.0504**	**4.5271**
C	**-0.9321**	**2.1885**	**3.3607**
C	**-1.1998**	**5.6288**	**4.8936**
C	**-1.5027**	**2.5678**	**5.9225**
C	**-0.2581**	**2.2275**	**6.7825**
N	**-0.5759**	**0.4311**	**0.9478**
C	**-0.8650**	**-0.0853**	**2.2318**
C	**-0.9768**	**-1.5239**	**2.1910**
C	**-0.7403**	**-1.8726**	**0.8228**
C	**-0.5128**	**-0.6326**	**0.1282**

C	**-1.2709**	**-2.4274**	**3.3593**
C	**-0.6522**	**-2.9443**	**-0.1217**
O	**-0.7803**	**-4.1963**	**-0.0184**
C	**-0.3502**	**-2.2811**	**-1.5436**
C	**0.9430**	**-2.8519**	**-2.1231**
O	**2.0783**	**-2.6441**	**-1.7161**
O	**0.6701**	**-3.6762**	**-3.1929**
C	**1.8177**	**-4.3199**	**-3.8093**
C	**-2.8595**	**-3.8659**	**-4.6902**
H	**2.7659**	**-0.3291**	**0.2775**
H	**3.9485**	**0.0789**	**1.5777**
H	**2.8526**	**3.9186**	**2.2049**
H	**2.1800**	**2.4930**	**3.0664**
H	**3.9701**	**2.6181**	**2.7679**
H	**3.3196**	**-9.4741**	**3.2817**
H	**2.1310**	**-10.1870**	**4.4129**
H	**-0.3231**	**-9.5341**	**4.2556**
H	**2.6030**	**-7.7286**	**1.6160**
H	**-1.9951**	**-7.8075**	**3.5703**
H	**0.9329**	**-6.0117**	**0.9320**
H	**-1.2579**	**-5.2177**	**1.1902**
H	**0.8453**	**4.2744**	**-3.6528**
H	**-0.5677**	**6.3944**	**2.3195**
H	**-1.2609**	**0.2950**	**4.3088**
H	**0.6169**	**-0.6227**	**-4.0460**
H	**0.4200**	**2.0608**	**-4.9072**
H	**2.8289**	**2.3680**	**-4.2307**
H	**2.5653**	**0.7542**	**-4.9718**
H	**2.7352**	**0.9142**	**-3.1925**
H	**-1.2038**	**0.6510**	**-5.4432**
H	**-2.0257**	**0.9647**	**-3.8955**
H	**-3.1358**	**-0.9234**	**-4.8546**
H	**-2.1466**	**-1.6092**	**-3.5699**
H	**1.5420**	**7.6036**	**-2.7835**
H	**-0.1990**	**7.6746**	**-3.1532**
H	**0.7943**	**6.3423**	**-3.8003**
H	**-0.3182**	**8.0619**	**1.1906**
H	**0.0367**	**10.1249**	**0.0463**
H	**0.4344**	**9.2705**	**-1.5636**
H	**-1.9083**	**6.3324**	**4.4101**
H	**-1.5802**	**5.4225**	**5.9117**
H	**-0.2390**	**6.1747**	**5.0072**
H	**-2.0992**	**3.3381**	**6.4538**
H	**-2.1522**	**1.6701**	**5.8671**
H	**0.3914**	**3.1159**	**6.9126**
H	**-0.5555**	**1.8697**	**7.7900**
H	**0.3525**	**1.4359**	**6.3060**
H	**-2.1537**	**-2.0785**	**3.9352**
H	**-1.4721**	**-3.4622**	**3.0320**
H	**-0.4224**	**-2.4679**	**4.0772**

H	**-1.1774**	**-2.5911**	**-2.2074**
H	**1.4041**	**-4.9078**	**-4.6443**
H	**2.5318**	**-3.5634**	**-4.1835**
H	**2.3290**	**-4.9762**	**-3.0806**
H	**-3.7868**	**-3.2660**	**-4.6075**
H	**-2.3649**	**-3.9494**	**-3.7043**
H	**-3.1121**	**-4.8753**	**-5.0553**
H	**2.1991**	**-10.7431**	**2.7195**
H	**2.1701**	**-0.0155**	**1.9424**

Chapter 1

Chapter 2

Chapter 3

Chapter 4

Chapter 5

Chapter 5

Chapter 6

CURRICULUM VITAE

Leysan Khuzeeva

Address: Max-Planck Institute for Bioinorganic Chemistry,
Stiftstraβe 34-36, 45470 Mülheim an der Ruhr, Germany
Phone: +49 208 / 306 - 3891
Fax: +49 208 / 306 - 3951
Email: khuzeeva@mpi-muelheim.mpg.de
Web: www.mpibac.mpg.de

Date of birth: 22.12.1982
Place of birth: Kazan, Russia
Gender: Female
Nationality: Russian

Present position: Ph.D. student at Mathematisch-Naturwissenschaftlichen Fakultät of Heinrich-Heine University (Düsseldorf) and Research Fellow in Max-Planck Institute for Bioinorganic Chemistry (Mülheim an der Ruhr).

Education:

- 01.09.2000 - 31.07.2005 Diploma in Physics (M.S.), Faculty of Physics, Kazan State University, Kazan, Russia. Graduated: excellent.

Positions Held:

- 2003-2005 – Assistant in laboratory of molecular photochemistry of Kazan Physico-Technical Institute, Kazan, Russia.
- 2005-2007 – PhD student (Sfb 498, project A3 by Antonkin/Stehlik) in Fachbereich Physik, Institut für Experimental Physik (WE 1), Freie Universität Berlin, Berlin, Germany.

Visits: 2005 (March-May) - Visiting scientist, Free University of Berlin, Berlin, Germany. (Prof. Dietmar Stehlik).

Technical and Specialized Skills:

- Electron paramagnetic resonance techniques (CW EPR, TREPR, advanced ENDOR)
- Basic biochemical skills

Research Interests:

- Spin chemistry and its application in photochemistry
- Electron paramagnetic resonance spectroscopy (CW EPR, TR EPR, advanced EPR\ENDOR techniques)
- Interest in studying of electron transfer in photosynthetic systems

Languages: Russian (native language), English (good), German (basic level, A2 of Göthe Institute)

Awards:

- 2004 (Nov.) – The 2nd place of anniversary scientific conference in department of Physics, Kazan, Russia.
- 2005 – The 1st place of scientific student's conference in the Physics Department, of Kazan State University, Kazan, Russia.
- 2005 – The 1st place of All-Russian conference "Structure and dynamics of molecular systems", Yalchik, Russia.
- 2005 –Teplov M.A. scholarships from Academic Council of the Physics Department of Kazan State University.
- 2006 – The best poster of All-Russian conference "Structure and dynamics of molecular systems", Yalchik, Russia.

Publications:

- Khuzeeva L., Heinnickel M., Golbeck J.H., Antonkine M.L., Investigation of Photosynthetic Reaction Centers *Heliobacterium modestecaldum* by Time-resolved Electron Paramagnetic Resonance (2006) in book of abstracts of conference XIII All-Russia conference "Structure and dynamics of molecular systems" in Yalchik. p. 360 – 363.
- Savitsky A., Heinnickel M., Khuzeeva L., Antonkine M.L., Möbius K. and Golbeck J.H. Characterization of Homodimeric Type I Reaction Center Cores from *Heliobacterium modesticaldum* by High-field Electron Paramagnetic Resonance Spectroscopy. (2008) J.F. Allen et al. Photosynthesis. Energy of Sun: 14th International Congress on Photosynthesis Research 2007, p. 65–68.
- Khuzeeva L., Savitsky A., Niklas J., Heinnickel M., Möbius K., Golbeck J.H., Lubitz W., Antonkine M.L. Characterization of the Heliobacterial Reaction Center by the Electron Paramagnetic Resonance Spectroscopy at X-, Q-, W-bands. Photosynth. Research, in preparation.

- Niklas J., Khuzeeva L., Lubitz W., Antonkine M.L. Investigation of the Electron Acceptor $A_0^{\bullet-}$ in Photosystem I and Chl $a^{\bullet-}$ in Solution by Pulsed Q-band EPR Spectroscopy. Biochimica et Biophysica Acta, in preparation.

Date Signature